Cavity QED - Engineering the Phonon Interactions

Master Thesis

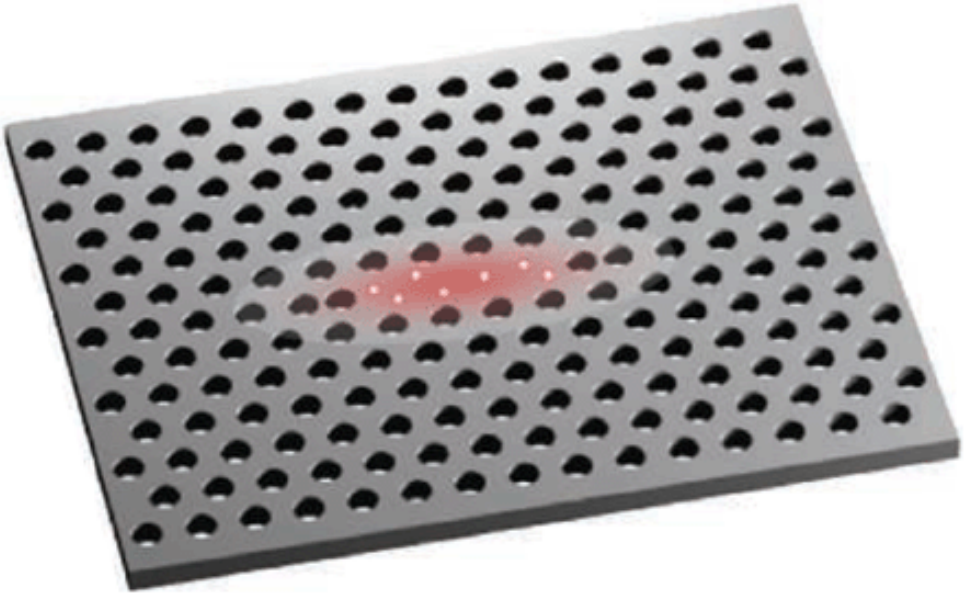

Anders Nysteen

Supervisors: Per Kær Nielsen and Jesper Mørk

May 29, 2013

DTU Fotonik
Department of Photonics Engineering

The picture on the front page is taken from `http://www.photonics.jst.go.jp/en/subject/index.html` and shows a sketch of a cavity-QED system, where quantum dots are grown inside a photonic crystal cavity.

Abstract

It is well-known that dephasing plays a major role in semiconductor cavity QED systems, and that this effect deteriorates the properties of, e.g., photonic crystal and micropillar realizations of single-photon sources. Even at low temperatures, scattering with phonons leads to decoherence.

We consider the possibility of altering the dephasing properties of the electron-phonon coupling by changing the electronic and phononic confinement. The starting point of our work is a recently published theory by P. Kaer *et. al.* (2010) [1], which considers longitudinal acoustic phonons described by a non-Markovian reservoir. These interact through the deformation potential coupling with a coupled quantum dot-cavity system. By applying a quantum master equation approach, we solve the equations of motion for the reduced density matrix, where the phonon degrees of freedom have been traced out.

Regarding the electronic confinement, we suggest an approach which relies on the asymmetry between electron and hole wavefunctions in the quantum dot. Commonly in the literature, this asymmetry is neglected in analyses of phonon-mediated dephasing effects in semiconductors. Our calculations show, that for a cavity QED system with the cavity and quantum dot tuned out of resonance, these assumptions neglect significant dynamics.

We demonstrate that for idealized spherical, but unequal, electron and hole wavefunctions there exists a non-zero cavity detuning where the phonon scattering is identically zero. The effect is due to a balancing between the carrier deformation potentials and the wavefunction asymmetry and only appears in materials where the deformation potential interaction shifts the energy bands in the *same* direction. For realistic truncated conical QD structures, analyzed by FEM calculations, a complete suppression of phonon scattering is not observed, but an optimal cavity detuning is still present where the phonon-induced pure dephasing is significantly reduced.

When confining the coupled QD-cavity system in an infinite slab, two resonant phonon modes appear, corresponding to the symmetric and anti-symmetric vibrational slab mode. We show that by tuning the optical cavity onto one of the resonance energies, the phonon-assisted cavity feeding increases significantly. At slightly lower phonon energies, a suppression of the phonon modes appears, which, with great possibility, could be used to decrease phonon-induced dephasing. A bulk description of the phonon modes is shown to be sufficient above 50 nm when considering a single reasonably-sized self-assembled QD placed in the center plane.

We believe these effects can be important for engineering the coherence properties of state-of-the-art QD-cavity structures.

Resume

Det er velkendt, at dephasing har stor indflydelse på kvanteelektrodynamikken (KED) i kaviteter for nanoskala-halvlederstrukturer, og at denne effekt forringer realiseringen af fotoniske krystaller og mikrosøjle-resonatorer som enkelt-fotonkilder. Selv ved lave temperatuers giver fononspredning til dekohærens.

Vi undersøger muligheden for at ændre dephasing-egenskaberne af elektron–fonon-koblingen ved at ændre det elektroniske og fononiske confinement. Udgangspunktet for vores arbejde er en nyligt publiceret teori af P. Kaer *et. al.* (2010) [1], som betragter longitudinale akustiske fononer beskrevet ved et ikke-Markoviansk reservoir. Disse vekselvirker gennem deformationspotentialeinteraktion med et koblet kvantedot–kavitetssystem. Ved at anvende kvante-master equation-formalisme løser vi bevægelsesligningerne for den reducerede tæthedsmatrix, hvor frihedsgraderne for fononerne er blevet tracet ud.

For det elektroniske confinement foreslår vi en fremgangsmåde som bygger på asymmetrien mellem elektron- og hul-bølgefuntionen i kvantedotten. Denne asymmetri bliver ofte ignoreret i litteraturen i analyser af fonon-medierede dephasing-effekter i halvledere. Vores udregninger viser, at for et kavitets-KED-system, hvor kavitet og kvantedot er ude af resonans, kan disse antagelser overse vigtig dynamik.

Vi viser, at for idealiserede sfæriske, men uens, elektron- og hul-bølgefunktioner, eksisterer detunings forskellig fra nul, hvor fonon-spredningen identisk er nul. Denne effekt skyldes en balance mellem ladningsbærernes deformationspotentiale og bølgefunktionens asymmetri, som kun opstår i materialer, hvor valens- og ledningsbånd bliver forskudt i *samme* retning, når krystallen sammenpresses. For realistiske strukturer af trunkerede koniske kvantedots, som vi analyserer med FEM-udregninger, opnås ikke en komplet elimination af fonon-spredningen, men der forekommer en optimal kavitets-detuning, hvor den fonon-inducerede pure dephasing-rate er reduceret markant.

Ved at placere kvantedot-kavitetssystemet i en uendelig plade opstår der to resonante vibrationstilstande, svarende til den symmetriske og anti-symmetriske vibrationelle mode i pladen. Vi påviser, at ved at tune den optiske kavitet til en af disse resonanser, så vil den fonon-assistered kavitets-feeding øges markant. Ved frekvenser lidt lavere end resonansfrekvenserne opnås en undertrykkelse af fonon-modes, og det vil med stor sandsynlighed kunne udnyttes til at mindske den inducerede dephasing. En bulk beskrivelse af fononerne ses tilstrækkelig for plader tykkere end 50 nm med for et enkelt selv-dannet kvantedot i center-planet af pladen.

De påviste effekter formodes at have en vigtig effekt for at kunne kontrollere kohærensegenskaberne i nutidens kvantedot–kavitets-strukturer.

Preface

This thesis is submitted as fulfilment of the requirements for obtaining the degree of Master of Science in Engineering at the Technical University of Denmark (DTU). The work has been accomplished at the Department of Photonics Engineering headed by Professor Jesper Mørk, and the duration of the work was 5 months in the period from April 2011 to October 2011 corresponding to a credit of 30 ECTS points.

First of all, I would like to thank my supervisors Per Kær Nielsen and Professor Jesper Mørk for their constant encouragement and many fruitful discussions on phonon interaction and especially Per for providing a solid theoretical framework in which I carried out my calculations.

Furthermore, I thank the (former) Quantum Photonics group at DTU, particularly Kristian Høeg Madsen and Asger Kreiner-Møller, for introducing me to their work and for providing the experimental point of view on the theoretical features of my work. I would also like to acknowledge the superb company of my fellow students Mikkel Settnes and Lasse Mejling Andersen throughout my entire period of studies at DTU, and Mikkel for enlightening discussions on fundamental quantum mechanics.

Finally, I would like to thank my family and friends for their wonderful support during the project.

Anders Nysteen
Department of Photonics Engineering
Technical University of Denmark
27 October 2011

Contents

Chapter 1

Introduction

Information may be considered the most fundamental thing that must propagate from a cause to an effect, and how that information is transmitted and processed in physical systems has been a great research topic the last couple of decades. Through the evolving field of quantum mechanics, the classical information theory was expanded and the so-called quantum information technology was introduced, opening for new ways of treating information in ways that was not possible according to classical theory. A new feature was the concept of quantum cryptography, where quantum states are used to transport classical information in a perfectly secure way, revealing possible eavesdroppers [2].

Another hot topic in the field of quantum information technology is quantum computation. In standard computation technology, information is stored in bits, which are logical states that attain a value of "0" or "1". In quantum computation, logical states are also described by two-state systems, which may be the two spin states of a spin 1/2-particle [3], the ground and excited state of an atom [4, 5], or vertically and horisontally polarised light [6]. The fundamental unit in a quantum computer is the qubit (*qu*antum *b*inary dig*it*), the quantum mechanical analogy to the classical bit. The difference is that the qubit may not only be in the state $|0\rangle$ or the state $|1\rangle$, but also in a linear superposition of these two states. This creates an infinite number of bit states not available according to classical theory, and this could be used to increase the effiency of computer algorithms such as factorizing of large numbers [7].

An important aspect of quantum information technology is the ability of a light source to emit a single quantum of light, the so-called *photon*. The first experimental realization of a single-photon source was done in 1977, where a strictly quantum mechanical light source was presented [8], (see [9, 10] for review articles on single-photon sources). A lot of research has been done on single-photon sources ever since, and the qubit, described by the two polarisation states of a photon, shows promising features. The photon has the advantage that it only interacts weakly with the surroundings, and due to its propagating nature, it carries information along. A drawback is, however, that photons do not mutually interact, making the construction of two-qubit quantum gates challenging, but several designs have been proposed [6].

A physical system may only be used for quantum information technology if certain criteria are fulfilled [11]. The ideal single-photon source must have *directional emission into a single mode of the radiation field*, and *the photon must be emitted when it is needed*, "on demand" [12]. Furthermore the emitted phonons must be *indistinguishable*, which is a measure of how well the photon overlap is from emission to emission.

The improvement of nanoscale fabrication enables the construction of even smaller quantum

systems. The properties of light emitters may no longer be described by the intrinsic properties of the light source only, but the effects of the environment has to be taken into account to describe the light-matter interaction correctly. These interactions introduce decoherence of the photonic degrees of freedom, which reduces the indistinguishability, and thus, for a realistic system, full indistinguishability will be unachievable.

In the literature the coherence time, T_{coh}, is usually phenomenologically expressed as [13], [14]

$$\frac{1}{T_{\text{coh}}} = \frac{1}{T_{\text{dephasing}}} + \frac{1}{2T_{\text{lifetime}}}, \tag{1.1}$$

where $T_{\text{dephasing}}$ is a characteristic time of all relevant dephasing processes and T_{lifetime} is the emission lifetime of the excited QD state. The ratio $T_{\text{coh}}/(2T_{\text{lifetime}})$ may be interpreted as the "degree of indistinguishability" and is less than unity when dephasing processes are present. The indistinguishabilty may be increased in two ways, either by increasing $T_{\text{dephasing}}$ through minimization of the dephasing effects, or by shortening the emission lifetime. Both approaches will be discussed in this thesis.

A promising structure for a single-photon emitter is a so-called quantum dot (QD) placed inside a photonic cavity [15, 16, 17]. These QD single-photon emitters have shown applications in both quantum cryptography [18] and quantum computation [19]. The QD-cavity system will be the main system of this thesis. Therefore we describe the properties of a QD and a photonic cavity in details.

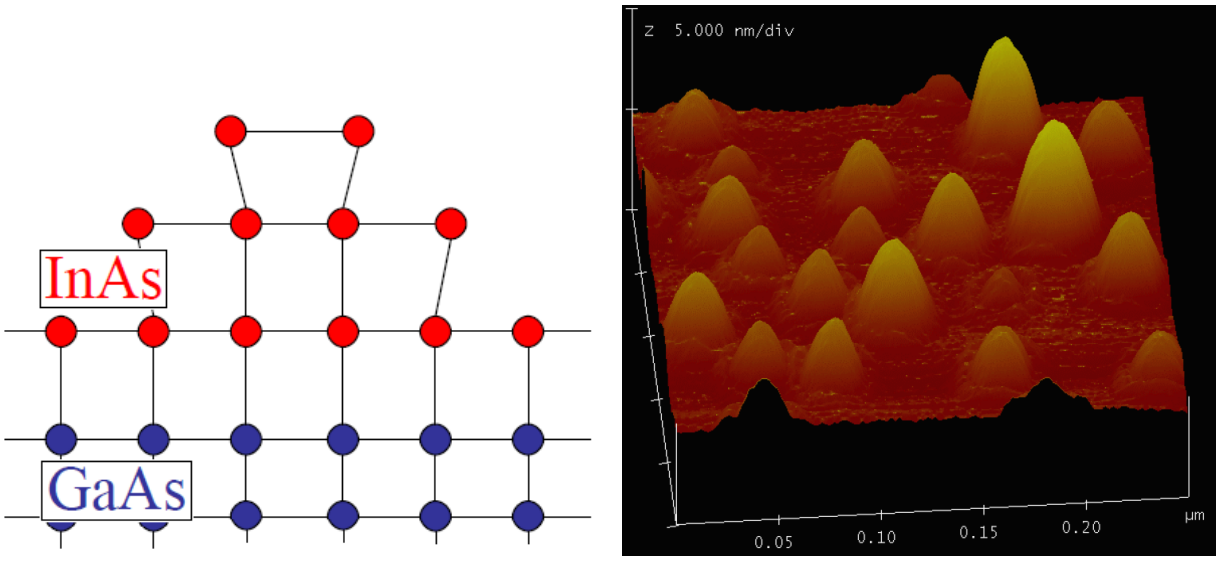

Figure 1.1: **(a)** Quantum dots on a wetting layer are formed by strain effects when evaporating InAs onto a GaAs substrate due a difference in lattice constants, picture taken from [20]. **(b)** Micrograph of self-assembled QDs, where the height scale indicates 5 nm/division. Courtesy of Steve Lyon [20].

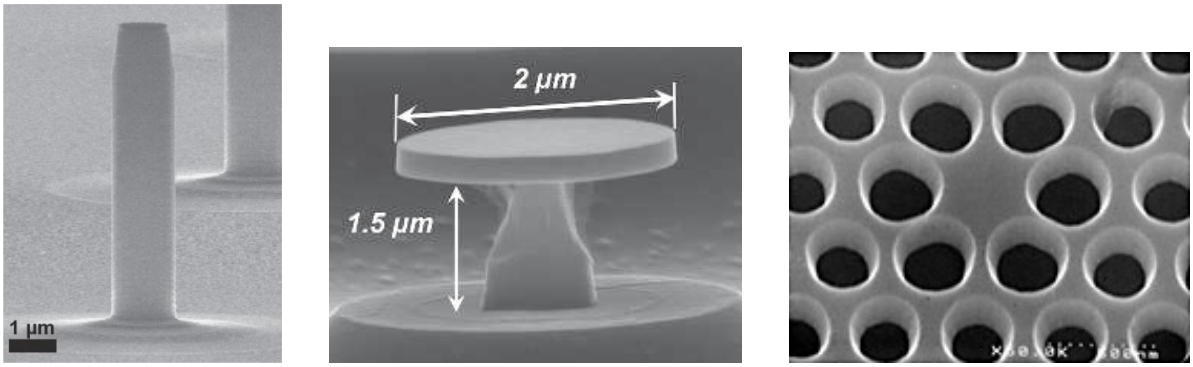

(a) (b) (c)

Figure 1.2: **(a)** Scanning electron micrograph of a 1.2 μm diameter pillar cavity, where the optical cavity is in the growing direction. Fabricated at University of Würzburg, courtesy of D. Press et. al. [33]. **(b)** Scanning electron microscopy picture of a 2 μm diameter microdisk seen from the side, where the optical modes propagate in the ring-structure, the so-called whispering gallery modes. Fabricated at LPN/CNRS, courtesy of E. Peter et. al., [34]. **(c)** Scanning electron micrograph image of a single laser cavity where light is trapped in the missing hole-defect in the periodic structure of changing refractive index on the same scale as the wavelength of the light. The volume of the cavity is 0.03 cubic microns. Courtesy of O. Painter, California Institute of Technology [35].

Semiconductor quantum dots and photonic cavities

The semiconductor industry is developing rapidly, and the possibility of creating nanoscale structures has become a reality. Semiconductors posses a high degree of freedom in designing structures with specific electronic properties, making semiconductors very viable for implementing efficient single-photon sources and to integrate these in larger solid-state systems.

Semiconductor quantum dots are point-like nanoscale heterostructures, in which electrons are confined in all three dimensions. A standard way to create QDs in a semiconductor is by epitaxial growth using the Stranski-Krastanow technique [21, 22, 23, 24]. By molecular beam epitaxy [25], a very thin semiconductor layer, e.g. InAs, is evaporated onto a substrate consisting of another semiconductor material, e.g. GaAs. The difference in lattice constants builds up strain in the material leading to the formation of small InAs-islands randomly positioned over a thin wetting layer (WL), see Fig. 1.1a. Finally a thick layer of the substrate is grown on the top. Due to this procedure of growing the dots by strain effects, the dots are called self-assembled quantum dots, and they typically vary between 4-100 nm in size [26, 27], depending on the exact growing parameters, see Fig. 1.1b.

Photonic cavities are structures in which light is confined in resonant modes which depend on the structure material and geometries. In semiconductors three different types of microcavities have shown to interact strongly with light and are often discussed as efficient cavity quantum electrodynamical systems [28], see Fig. 1.2a-c. These are micropillar resonators [29], microdiscs [30], and photonic crystal cavities (PCCs) [31], see [32] for a review on semiconductor photonic cavities. Considering a PCC as example, light is confined due to a defect in a periodic structure of materials with changing dielectric constant on a length scale that is comparable to the wavelength of light.

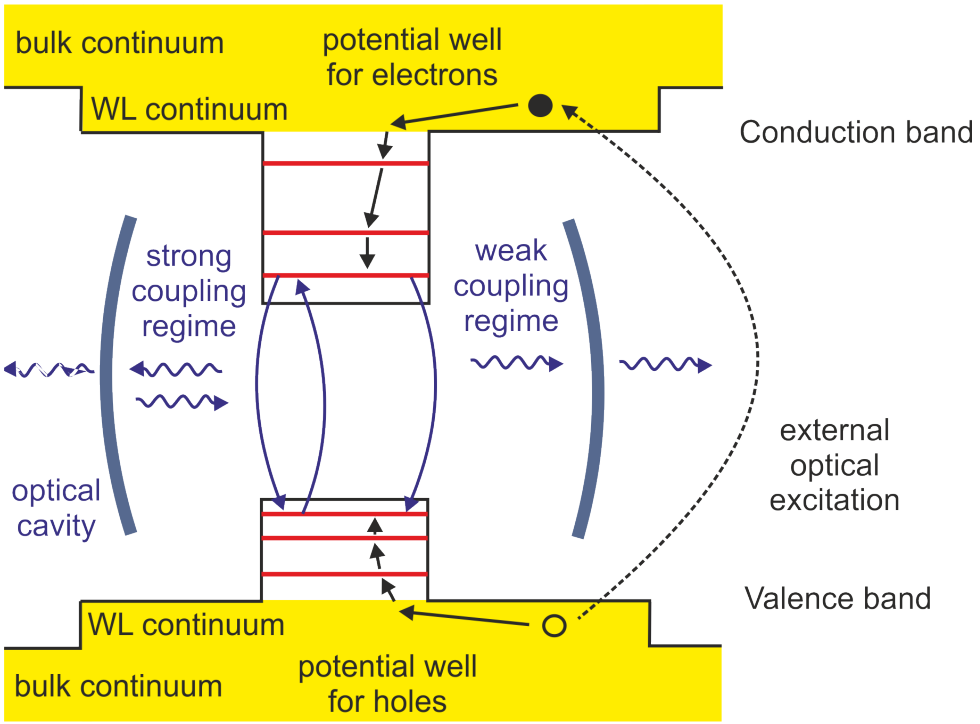

Figure 1.3: Energy diagram of a QD-wetting layer model, where the QD is excited through the wetting layer. The captions and drawings in blue indicates the interaction of the QD with an optical cavity. For further explanations, see the main text. Inspired by picture in [36].

1.1 Dynamics in a cavity-QD system

To understand the dynamics in a cavity-QD system, the physical properties of the quantum dot must first be understood. In a QD the electrons and holes are confined by having a semiconductor with lower band edges than the surrounding semiconductor material, see Fig. 1.3. The nano-scale confinement implies that carrier modes is described by a discrete set of energies in the dot. In the wetting layer the carriers are confined only in one direction in a so-called quantum well structure, where the two unconfined dimensions gives a continuum of WL modes. In the barrier material the electrons are unconfined and are described by a bulk continuum.

Due to various decay mechanisms, the lifetime of a carrier an excited QD state is finite, and eventually an electron and a hole will recombine and a photon will be emitted by spontaneous emission. A standard experiment carried out in solid-states quantum optics, used e.g. to characterize quantum dots, is photoluminescence spectroscopy, where spectral information about the emitted light is obtained[1] [38]. The excitation of a QD is indicated in Fig. 1.3 by the black arrows. Typically a WL mode is excited by an external optical excitation[2], which creates an

[1] If the QD is grown with the Stranski-Krastanow technique, a lot of dots appear in the sample, each having different optical transition frequencies due to their different sizes, and these are all excited when the WL initially is excited. By using a photodiode with a narrow spectrum, it is, however, possible to pick out a single quantum dot for the measurements [37].

[2] The excitation of a WL mode and not directly a QD mode is due to practical purposes such that the detection frequency is different from the excitation frequency. If the frequencies were equal, it would be difficult to distinguish the emitted light from the excitation pulse in the measured spectrum.

electron in the conduction band and a hole in the valence band. In the WL the probability of scattering on phonons (quantized lattice vibrations) and other carriers is large, and the carriers quickly scatters to the bottom of the WL band. The ground state of the carriers is in the bottom of their respective bands, such that holes actually "scatter upwards" as indicated in Fig. 1.3. The carriers are captured into the QD states and through scattering processes they relax to the ground state of the QD, from which the carriers may recombine at the creation of a photon.

As bare QD as a light source has the advantage of being described by all solid states, but the light emission is non-directional. By placing the QD in an optical cavity, directional emission is obtained, and two physically different regimes appear for the combined QD-cavity system, the strong and the weak coupling limit [39]. The dynamics in the two regimes are illustrated in Fig. 1.3 by the blue lines and captions. In the strong coupling limit, the strength of the light-matter coupling is large compared to the loss mechanisms, and energy oscillates between the QD and the cavity. The weak coupling limit is characterized by loss mechanisms dominating the coherent coupling, giving an irreversible decay of the excited QD, where the cavity acts like an additional loss mechanism. The weak coupling limit is especially interesting for single-photon sources due to the so-called Purcell effect, where a change in the local optical density of states due to the optical cavity enhances the spontaneous emission rate. When the spontaneous emission rate increases compared to the decoherence rate, the indistinguishability of the emitted photons is increased, making this a promising single-photon source.

Experiments on various configurations with QDs inside photonic cavities have been carried out, showing features of either the weak or the strong coupling regime [40, 41], and from the latter a value of the electron-photon coupling strength for the given system may be extracted. The dynamics of the system has been described by basic analytical models, where the phonon interaction is examined only by a pure dephasing rate [42]. This approximation have recently been shown to omit important effects of e.g. temperature, which may only be realized analytically by applying a many-body picture describing the interaction between electron, photons and phonons [1, 43].

In this thesis we explore the many-body model of [1] by applying a master-equation formalism and determining the reduced density matrix for a two-level quantum dot inside a single-mode cavity, where the interaction with a large phonon reservoir has been traced out. We assume that the phonon dispersion is not changed by the presence of the optical cavity, and we neglect multi-phonon processes. We present a thorough description of the physics that the model in [1] contains, and we exploit the model to qualitatively discuss the phonon-induced decrease in emitter lifetime and the indistinguishability of the emitted photons. In the literature, simple assumptions are always made concerning the electronic confinement in similar models, and to our knowledge this is something that has not examined in details. We show in this thesis that these simple assumptions miss relevant physical features, and we demonstrate how both the electronic and phononic confinement may be engineered to change the effect of electron-phonon scattering on the emitter lifetime and pure dephasing.

Other approaches to describe the dynamics of a coupled QD-cavity system is considered in [44, 45], where a Green's function formalism is used.

1.2 Outline of the thesis

This thesis is divided into eight chapters, and a short outline of the contents is given below

Chapter 2: Fundamental Theory We start from the Hamiltonian of a charged particle interacting with an electromagnetic field and derive a Hamiltonian in second quantization describing the basic form of the Hamiltonian describing the QD-cavity system. An elaborating discussion of the electron-phonon interaction is given for three different electron-phonon coupling mechanisms.

Chapter 3: Equations of Motion The basic theory of quantum dynamics is reviewed, and we derive the reduced density matrix for the QD-cavity system by tracing out the phonon degrees of freedom in a time-local scattering assumption.

Chapter 4: Model: Cavity QED System The equation of motion from Chapter 3 is applied to the model Hamiltonian derived in Chapter 2, and the resulting equations of motion (EOM) may be formulated as a linear matrix differential equation.

Chapter 5: Exploring the Model The EOM from Chapter 4 are solved, and by starting from a basic lossless system we thoroughly demonstrate the physical interpretation of the different terms in the EOM, when the lossless model is expanded. We introduce the effective phonon spectrum and describe how this is related to the relaxation time of the QD. Finally, we relate the physics in this model with recent publications.

Chapter 6: Pure Dephasing and Indistinguishability An analytic expression for the time-evolution operator of the QD-cavity system i derived. This is used to discuss the phonon-induced pure dephasing effects and relate these to indistinguishability.

Chapter 7: Engineering the Electronic Confinement The influence of the shape of the electron wavefunction on the electron-phonon interaction is examined in details, first with an approximate ellipsoidal wavefunction and then with wavefunctions obtained from FEM-calculation, showing promising QD configurations for achieving low dephasing.

Chapter 8: Engineering the Phononic Confinement - Phonons in an Infinite Slab The confinement of phonons in a simple slab structure is considered, showing both resonant and suppressed phonon modes, which are discussed in relation to the QD-cavity system.

The simulations in this thesis are carried out using the parameters in Appendix A when nothing else is mentioned.

Chapter 2

Fundamental Many-Body Theory

In the first half of this chapter, we will sketch the origin of the Hamiltonian used to describe the semiconductor QD-cavity system and clarify the various assumptions. The description is based on standard textbooks [46, 47, 48], following [36]. The second half discusses the three major electron-phonon scattering mechanisms, namely the deformation potential interaction, the piezoelectric interaction, and the Fröhlich coupling.

2.1 The Hamiltonian

In the many-body description of the QD-cavity system, several different interaction mechanisms contribute to the total Hamiltonian. To clarify the different contributions to the total Hamiltonian of the system, we divide the interaction into three fundamentally different parts,

$$H(t) = H_0 + H_{\text{int}} + U(t). \tag{2.1}$$

H_0 describes the non-interacting part of $H(t)$, and the interaction part, H_{int}, constitutes all possible interactions between the particles. As discussed later when describing the operators in second quantization, H_0 only contains quadratic terms in the fermionic or bosonic operators, whereas H_{int} consists of the product of more than two fermionic or bosonic operators. $U(t)$ represent all effects which have an explicit time dependence and these effects drive the system from equilibrium. All the derivations are made keeping in mind that we want to use the theory to describe a semiconductor heterostructure.

In this work we consider interaction of charged particles with a classical and quantized electromagnetic field. The corresponding Hamiltonian is described in [49, 50, 48, 51] and is in the Schrödinger picture given by

$$H = \sum_i T_i(t) + \frac{1}{2}\int \mathrm{d}\mathbf{r}\, \left[\epsilon|\mathbf{E}(\mathbf{r})|^2 + \frac{1}{\mu_0}|\mathbf{B}(\mathbf{r})|^2\right]. \tag{2.2}$$

The first term is the sum over all single-particle Hamiltonians describing the kinetic $T_i(t)$ energy of each individual particle, and the second term constitutes the energy of the total electromagnetic field. Due to the time invariance of the equations of motion, H is a constant of motion, see e.g. [48]. In Eq. (2.2) we have included non-resonant contributions to screeing by replacing the vacuum permittivity ϵ_0 by the background dielectric constant, $\epsilon = \epsilon_r\epsilon_0$, with ϵ_r being the relative permittivity [50].

Choosing to work in the Coulomb gauge where the vector potential $\mathbf{A}$ is transverse, i.e. $\boldsymbol{\nabla} \cdot \mathbf{A}(\mathbf{r}, t) = 0$, we have

$$\mathbf{E}_t(\mathbf{r}, t) = -\frac{\partial \mathbf{A}(\mathbf{r}, t)}{\partial t}, \qquad \mathbf{E}_l(\mathbf{r}, t) = -\boldsymbol{\nabla}\varphi(\mathbf{r}, t), \qquad \mathbf{B}(\mathbf{r}, t) = \boldsymbol{\nabla} \times \mathbf{A}(\mathbf{r}, t), \tag{2.3}$$

where the electric field is divided into a transverse part determined by the vector potential and a longitudinal part described by the scalar potential $\varphi(\mathbf{r}, t)$. Furthermore the quantized field must be given in the Heisenberg picture where the operators are time-dependent. We will be dealing with both classical and quantized electromagnetic fields, and thus the vector potential must be written as a sum of these $\mathbf{A}(\mathbf{r}, t) = \mathbf{A}_{\text{cl}}(\mathbf{r}, t) + \mathbf{A}_{\text{qm}}(\mathbf{r})$.

A standard way of introducing the electromagnetic interaction is in a gauge-invariant way by the method of minimal substitution $\mathbf{p} \to \mathbf{p} - q\mathbf{A}$, see e.g. [52]. Applying this in the Coulomb gauge, the kinetic energy of the individual particles may be written as

$$\sum_i T_i(t) = \sum_i \frac{1}{2m_i} \left[\mathbf{p}_i - q_i \mathbf{A}(\mathbf{r}_i, t)\right]^2 \tag{2.4}$$

$$\approx \sum_{i,\text{ions}} \frac{p_i^2}{2m_i} + \sum_{i,\text{elec}} \left[\frac{p_i^2}{2m_i} + \frac{e}{m_i}\mathbf{A}(\mathbf{r}_i, t) \cdot \mathbf{p}_i\right], \tag{2.5}$$

where q_i indicates the charge of the particle, $q_{\text{elec}} = -e$, and where summation over the spin index of the electron is contained in the sum to easen the notation. Three assumptions have been made to arrive at this expression, see e.g. [36]:

1. The response of the ions to the field will be much smaller than the response of the electrons due to the larger ion mass, and thus we neglect the ion-field interaction.
2. In the Coulomb gauge, $\mathbf{A}(\mathbf{r}_i)$ is transverse, and by using that $\mathbf{p}_i = -\mathrm{i}\hbar\boldsymbol{\nabla}_i$ one may show that $\mathbf{A}(\mathbf{r}_i) \cdot \mathbf{p}_i = \mathbf{p}_i \cdot \mathbf{A}(\mathbf{r}_i)$.
3. By considering low intensity fields, we may neglect terms of second order in $\mathbf{A}(\mathbf{r}_i)$.

To understand the contribution from the integral appearing in Eq. (2.2), it is advantageous to divide it into a transverse and a longitudinal part

$$H_{\text{trans}} = \frac{1}{2}\int \mathrm{d}\mathbf{r} \left[\epsilon |\mathbf{E}_t(\mathbf{r}, t)|^2 + \frac{1}{\mu_0}|\mathbf{B}(\mathbf{r}, t)|^2\right], \qquad H_{\text{long}} = \frac{1}{2}\int \mathrm{d}\mathbf{r}\, \epsilon |\mathbf{E}_l(\mathbf{r}, t)|^2, \tag{2.6}$$

using that the magnetic field is purely transverse, according to Maxwell's equations. As shown in [48], H_{long} is just the Coulomb electrostatic energy of the system of charges plus the Coulomb self-energy of the particle, which does not affect the dynamics, and we neglect it in this thesis. For a system of point charges,

$$H_{\text{long}} = V_{\text{Coulomb}} = \frac{1}{2}\sum_{i \neq j} \frac{q_i q_j}{4\pi\epsilon} \frac{1}{|\mathbf{r}_i - \mathbf{r}_j|}, \tag{2.7}$$

The Coulomb interaction may be written for the individual particle types,

$$V_{\text{Coulomb}} = V_{\text{ion-ion}} + V_{\text{elec-elec}} + V_{\text{elec-ion}} \tag{2.8}$$

$$= \frac{1}{2}\sum_{\substack{i \neq j \\ \text{ion-ion}}} \frac{q_i q_j}{4\pi\epsilon} \frac{1}{|\mathbf{R}_i - \mathbf{R}_j|} + \frac{1}{2}\sum_{\substack{i \neq j \\ \text{elec-elec}}} \frac{e^2}{4\pi\epsilon} \frac{1}{|\mathbf{r}_i - \mathbf{r}_j|} + \sum_{\substack{i \neq j \\ \text{elec-ion}}} \frac{(-e)q_j}{4\pi\epsilon} \frac{1}{|\mathbf{r}_i - \mathbf{R}_j|}. \tag{2.9}$$

Note that no factor of 1/2 is included in $V_{\text{elec-ion}}$ because double counting is not present in that sum. The last term $V_{\text{elec-ion}}$ may be simplified by considering displacements $\mathbf{u}_j$ of the ions relative to their equilibrium positions $\mathbf{R}_j^{(0)}$ in the static lattice,

$$\mathbf{R}_j = \mathbf{R}_j^{(0)} + \mathbf{u}_j. \tag{2.10}$$

The displacement will be smaller for the heavy ions than for the lighter electrons, and we may Taylor expand $V_{\text{elec-ion}}$ around $\mathbf{R}_j = \mathbf{R}_j^{(0)}$,

$$V_{\text{elec-ion}} = \sum_{i\neq j} \frac{(-e)q_j}{4\pi\epsilon} \frac{1}{|\mathbf{r}_i - \mathbf{R}_j|} \approx \sum_{i\neq j} \frac{(-e)q_j}{4\pi\epsilon} \left[\frac{1}{|\mathbf{r}_i - \mathbf{R}_j^{(0)}|} - \mathbf{u}_j \cdot \boldsymbol{\nabla}_{\mathbf{r}_i} \left(\frac{1}{|\mathbf{r}_i - \mathbf{R}_j^{(0)}|} \right) \right], \tag{2.11}$$

neglecting terms of second or higher order in the displacement. The first term may be recognized as the potential of electrons in a static lattice which we denote by $\mathcal{U}(\mathbf{r}_i)$. For an infinite and homogeneous lattice has well-known periodic Bloch state solutions for the electron wave functions, see e.g. [46, p. 36].

Summarizing from Eq. (2.5), (2.6), (2.9), and (2.11), we may divide the Hamiltonian in Eq. (2.2) into non-interacting parts,

$$H_{0,\text{elec}}\{\mathbf{r}_i\} = \sum_{i,\text{elec}} \left[\frac{p_i^2}{2m_i} + \mathcal{U}(\mathbf{r}_i) \right], \tag{2.12}$$

$$H_{0,\text{rad}} = \frac{1}{2} \int \mathrm{d}\mathbf{r} \left[\epsilon |\mathbf{E}_t(\mathbf{r},t)|^2 + \frac{1}{\mu_0} |\mathbf{B}(\mathbf{r},t)|^2 \right], \tag{2.13}$$

$$H_{0,\text{ion}}\{\mathbf{r}_i\} = \sum_{i,\text{ion}} \left[\frac{p_i^2}{2m_i} \right], \tag{2.14}$$

and interacting parts

$$H_{\text{elec-rad}}\{\mathbf{r}_i\} = \sum_{i,\text{elec}} \frac{e}{m_i} \mathbf{A}(\mathbf{r}_i,t) \cdot \mathbf{p}_i, \tag{2.15}$$

$$H_{\text{elec-ion}}\{\mathbf{r}_i\} = \sum_{i\neq j} \mathbf{u}_j \cdot \boldsymbol{\nabla}_{\mathbf{r}_i} \left(\frac{eq_j}{4\pi\epsilon} \frac{1}{|\mathbf{r}_i - \mathbf{R}_j^{(0)}|} \right), \tag{2.16}$$

$$H_{\text{elec-elec}}\{\mathbf{r}_i\} = \frac{1}{2} \sum_{i\neq j,\text{elec-elec}} \frac{e^2}{4\pi\epsilon} \frac{1}{|\mathbf{r}_i - \mathbf{r}_j|}, \tag{2.17}$$

$$H_{\text{ion-ion}}\{\mathbf{R}_i\} = \frac{1}{2} \sum_{i\neq j,\text{ion-ion}} \frac{q_i q_j}{4\pi\epsilon} \frac{1}{|\mathbf{R}_i - \mathbf{R}_j|}. \tag{2.18}$$

Note that the Hamiltonian Eq. (2.2) only is valid for non-relativistic particles. For relativistic particle modes, which obey $\hbar\omega \gtrsim mc^2$, interaction happens at high particle velocities with the possibility of creating new particles, which is not included in Eq. (2.2). A way to neglect the relativistic modes is to introduce an upper frequency limit for the modes to be included, see e.g. [48, p. 201].

2.1.1 Hamiltonian in first and second quantization

Assuming that the considered crystal lattice is approximately homogeneous, we are dealing with a system of different groups of identical particles. To deal with such many-body systems of identical particles it is convenient to formulate the problem in second quantization, see. e.g. [46] or [53]. Below we introduce the main point of the quantization procedure.

The state of a quantum mechanical particle is described by the wavefunction $\psi_\nu(\mathbf{r}) = \langle \mathbf{r}|\nu\rangle$ where $|\nu\rangle$ is the state ket described by a complete set of quantum numbers denoted ν. Here ν may label both a set of discrete or continuous quantum numbers.

In first quantization, a system of N identical particles is described by extending the single particle state function to an N-particle wavefunction $\psi(\mathbf{r}_1, \mathbf{r}_2, ..., \mathbf{r}_N)$. The basis for the N-particle system may be constructed from any orthonormal single-particle basis. Any given local one-particle operator $O_j = O(\mathbf{r}_j, \boldsymbol{\nabla}_{\mathbf{r}_j})$, such as the kinetic operator $-\frac{\hbar^2}{2m}\nabla^2_{\mathbf{r}_j}$, may be written in the $|\nu\rangle$-representation,

$$O_j = \sum_{\nu_a,\nu_b} O_{\nu_a\nu_b} |\psi_{\nu_a}(\mathbf{r}_j)\rangle\langle\psi_{\nu_b}(\mathbf{r}_j)|, \tag{2.19}$$

with

$$O_{\nu_a\nu_b} = \int \mathrm{d}\mathbf{r}_j \, \psi^*_{\nu_a}(\mathbf{r}_j) O(\mathbf{r}_j, \boldsymbol{\nabla}_{\mathbf{r}_j}) \psi_{\nu_b}(\mathbf{r}_j), \tag{2.20}$$

and the total contribution is found by summing over all positions, $O_{\mathrm{tot}} = \sum_j O_j$.

Two-particle operators such as the Coulomb interaction between particles at $\mathbf{r}_j$ and $\mathbf{r}_k$, $V(\mathbf{r}_j - \mathbf{r}_k) = \frac{e^2}{4\pi\epsilon_0}\frac{1}{|\mathbf{r}_j - \mathbf{r}_k|}$, is in the $|\nu\rangle$-representation given by

$$V_{jk} = \sum_{\nu_a,\nu_b,\nu_c,\nu_d} V_{\nu_c\nu_d\nu_a\nu_b} |\psi_{\nu_c}(\mathbf{r}_j)\rangle|\psi_{\nu_d}(\mathbf{r}_k)\rangle\langle\psi_{\nu_a}(\mathbf{r}_j)|\langle\psi_{\nu_b}(\mathbf{r}_k)|, \tag{2.21}$$

with

$$V_{\nu_c\nu_d\nu_a\nu_b} = \int \mathrm{d}\mathbf{r}_j \int \mathrm{d}\mathbf{r}_k \, \psi^*_{\nu_c}(\mathbf{r}_j)\psi^*_{\nu_d}(\mathbf{r}_k) V(\mathbf{r}_j - \mathbf{r}_k)\psi_{\nu_a}(\mathbf{r}_j)\psi_{\nu_b}(\mathbf{r}_k), \tag{2.22}$$

where the total contribution is $V_{\mathrm{tot}} = \frac{1}{2}\sum_{j,k\neq j} V_{jk}$.

When considering systems with a lot of particles, calculations with the full wavefunction $\psi(\mathbf{r}_1, \mathbf{r}_2, ..., \mathbf{r}_N)$ quickly becomes cumbersome, and calculations may more easily be carried out in second quantization representation or the so-called occupation number representation. Instead of describing the particles by wavefunctions, we count the number of particles in each orbital $|\nu\rangle$.

The main concept is to create an N-particle Hilbert space which is spanned by products of complete orthonormal sets of the single particle states $|\nu\rangle$. Each single-particle state consists of a spatial part $|\alpha\rangle$ and a spin part $|\sigma\rangle$, giving $|\nu\rangle = |\alpha\rangle \otimes |\sigma\rangle$.

This enables the description of operators by creation and annihilation operators in this new occupation number representation. As stated earlier, the non-interacting parts of the Hamiltonian are described in the general form of a one-particle operator O with two creation/annihilation operators, where interactions, such as the Coulomb interaction illustrated here, are described

by three or more [46, 47],

$$O = \sum_{\nu_i\nu_j} O_{\nu_i\nu_j} a^\dagger_{\nu_i} a_{\nu_j}, \tag{2.23}$$

$$V = \frac{1}{2} \sum_{\nu_i\nu_j\nu_k\nu_l} V_{\nu_i\nu_j,\nu_k\nu_l} a^\dagger_{\nu_i} a^\dagger_{\nu_j} a_{\nu_l} a_{\nu_k}. \tag{2.24}$$

Here $a^\dagger$ indicates a creation operator and a an annihilation operator.

To describe an operator in second quantization, the quantum field creation and annihilation operators $\Psi^\dagger(\mathbf{r})$ and $\Psi(\mathbf{r})$ are introduced,

$$\Psi^\dagger(\mathbf{r}) = \sum_\nu \psi^*_\nu(\mathbf{r}) a^\dagger_\nu = \sum_\nu \langle \mathbf{r}|\nu\rangle^* a^\dagger_\nu, \quad \Psi(\mathbf{r}) = \sum_\nu \psi_\nu(\mathbf{r}) a_\nu = \sum_\nu \langle \mathbf{r}|\nu\rangle a_\nu. \tag{2.25}$$

These operators may be interpreted as being the sum of all the possible ways that a particle can be added to/removed from the position $\mathbf{r}$ trough any of the basis states $\psi_\nu(\mathbf{r})$. Using these we obtain the real space representation of a single-particle operator in second quantization,

$$O = \sum_{\nu_a\nu_b} O_{\nu_a\nu_b} a^\dagger_{\nu_a} a_{\nu_b} \tag{2.26}$$

$$= \sum_{\nu_a\nu_b} \left(\int \mathrm{d}\mathbf{r}\, \psi^*_{\nu_a}(\mathbf{r}) O(\mathbf{r}) \psi_{\nu_b} \right) a^\dagger_{\nu_a} a_{\nu_b} \tag{2.27}$$

$$= \int \mathrm{d}\mathbf{r} \left(\sum_{\nu_a} \psi^*_{\nu_a}(\mathbf{r}) a^\dagger_{\nu_a} \right) O(\mathbf{r}) \left(\sum_{\nu_b} \psi_{\nu_b}(\mathbf{r}) a_{\nu_b} \right) \tag{2.28}$$

$$= \int \mathrm{d}\mathbf{r}\, \Psi^\dagger(\mathbf{r}) O(\mathbf{r}) \Psi(\mathbf{r}), \tag{2.29}$$

and a similar expression exists for two-particle operators.

In the following we will write the different term of the total Hamiltonian,Eq. (2.12)-(2.18), in second quantization, following [36]. We denote the bosonic creation and annihilation operators for photons by $a^\dagger$ and a, the bosonic operators for the phonons by $b^\dagger$ and b, and the fermionic operators describing the electron by $c^\dagger$ and c.

Non-interacting parts of the Hamiltonian

By non-interacting parts of the Hamiltonian we refer to the terms containing products of two bosonic or fermionic operators, and these terms has to be time-independent in the Schrödinger picture. The non-interacting part of H consists of an electronic, a photonic, and a phononic part, which are described below.

Electrons The non-interacting electron part of the Hamiltonian is Eq. (2.12) and may be written as

$$H_{0,e}(\{\mathbf{r}_i\}) = \sum_i H_{0,e}(\mathbf{r}_i). \tag{2.30}$$

In second quantization a preferred basis for electrons is the eigenstates of $H_{0,\text{elec}}$ obeying the Schrödinger equation $H_{0,e}(\mathbf{r})\psi_\nu(\mathbf{r}) = \hbar\omega_\nu\psi_\nu(\mathbf{r})$, in which the Hamiltonian Eq. (2.12) diagonalizes using Eq. (2.28),

$$H_{0,e} = \int \mathrm{d}\mathbf{r}\, \Psi^\dagger(\mathbf{r}) H_{0,e}(\mathbf{r})\Psi(\mathbf{r}) = \sum_{\nu_a\nu_b} c^\dagger_{\nu_a} c_{\nu_b} \hbar\omega_{\nu_b}\delta_{\nu_a\nu_b} = \sum_\nu \hbar\omega_\nu c^\dagger_\nu c_\nu. \tag{2.31}$$

The number operator $c^\dagger_\nu c_\nu$,,counts" if there is 0 or 1 electron (due to its fermionic nature) in state ν. If one electron is present in the state ν, $\hbar\omega_\nu$ is added to the total energy.

Photons The non-interacting photonic Hamiltonian stems from the energy of the transverse electromagnetic field Eq. (2.13). The quantization of the radiation field is described in details in many textbooks [39, 53]. The E-field may be expressed as a weighted sum of orthonormal mode functions $\{\mathbf{w}_n(\mathbf{r})\}$ which are determined by the boundary conditions of the specific problem. The quantum number n is combined of both the spatial and polarization quantum numbers. The total transverse electric field is obtained by summing over all modes

$$\mathbf{E}_t(\mathbf{r}, t) = \sum_n \mathcal{E}_n [a^\dagger_n(t) + a_n(t)]\mathbf{w}_n(\mathbf{r}), \tag{2.32}$$

where the time-dependence of the photonic annihilation and creation operators $a^\dagger_n(t)$ and $a_n(t)$ is described in the Heisenberg picture. The weight factor $\mathcal{E}_n = \mathrm{i}\sqrt{\hbar\omega_n/(2\epsilon_0 V_P)}$ may be understood as the electric field ,,per photon" of energy $\hbar\omega_m$, where ϵ_0 is the vacuum permittivity and V_P is the quantization of the photon modes.

With Eq. (2.3) we may relate the magnetic field to the electric field,

$$\boldsymbol{\nabla} \times \mathbf{E}_t(\mathbf{r}, t) = -\frac{\partial(\boldsymbol{\nabla} \times \mathbf{A}(\mathbf{r}, t))}{\partial t} = -\frac{\partial \mathbf{B}(\mathbf{r}, t)}{\partial t}, \tag{2.33}$$

and by using this when inserting the expression for the quantized electric field, Eq. (2.32), into $H_{0,\text{rad}}$, we arrive at

$$H_{0,\text{rad}} = \sum_n \hbar\omega_n \left(a^\dagger_n a_n + \frac{1}{2}\right), \tag{2.34}$$

where the $1/2$ describes the energy of the vacuum field.

Phonons The non-interacting part describing the phonons stems from the kinetic energy of the ions in Eq. (2.14) and the Coulomb-interaction between the ions in Eq. (2.18). Due to the heavy masses of the ions compared to the electron, the ions react slower to external perturbations. Furthermore the ions are placed in a static lattice, and under the *harmonic approximation*, as we will introduce below, the ion-ion interaction may be approximately described by a quadratic term in the bosonic operators, which is why it considered in this section, see e.g. [47, sec. 1.1] or [46, chap. 3].

We consider the displacement of an ion, $\mathbf{Q}_i$, from its equilibrium position in the static lattice, $\mathbf{R}^{(0)}_i$, such that $\mathbf{R}_i = \mathbf{R}^{(0)}_i + \mathbf{Q}_i$. In the same way as done for the electron-ion interaction in Eq. (2.11) a Taylor-expansion of $H_{\text{ion-ion}}$ is done around $\mathbf{Q}_i = \mathbf{0}$. The zeroth order term becomes a constant which does not affect the dynamics, and this is neglected. Furthermore the

equilibrium position may be defined such that the first order term is zero [46]. The first actual contribution comes from the second order term. The harmonic approximation states that due to the heavy ion masses and the static lattice, it is reasonable only to include the second order term in the Hamiltonian, in which case the quantized Hamiltonian describing the non-interacting part of the phonon Hamiltonian becomes [47, 54]

$$H_{0,\mathrm{ph}} = \sum_{\mu} \hbar\omega_{\mu} \left(b_{\mu}^{\dagger} b_{\mu} + \frac{1}{2} \right). \tag{2.35}$$

The quantum number μ is a combination of the wavevector $\mathbf{k}$, restricted to the first Brillouin zone, and the phonon branch λ dictating the polarization of the phonon. The term corresponding to $\mathbf{q} = \mathbf{0}$ corresponds to a uniform translation of the crystal and should formally not be included in the sum [46].

To express this Hamiltonian in second quantization we assume bulk phonons, i.e. the phonons are assumed to exist in a perfectly periodic lattice. For QDs grown with the Stranski-Krastranow technique, the QDs are typically small and the wetting layers thin, so this approximation is reasonable.

What is excluded in the harmonic approximation is terms of third or higher order in the displacement. These are the so-called anharmonic effects, where the first term has the form

$$\sum_{\substack{\mathbf{kq} \\ \lambda_1\lambda_2\lambda_3}} Q_{\mathbf{k},\lambda_1} Q_{\mathbf{q},\lambda_2} Q_{-\mathbf{k}-\mathbf{q},\lambda_3} M_{\mathbf{kq},\lambda_1\lambda_2\lambda_3}, \tag{2.36}$$

with $Q_i = |\mathbf{Q}_i|$ and where $M_{\mathbf{kq},\lambda_1\lambda_2\lambda_3}$ describes the interaction strength. As we see from Eq. (2.36), the anharmonic effets includes the possibility of one phonon decaying into two or more phonons vice versa. It is reasonable to neglect the anharmonic terms when considering the phonon dispersion relation, but they has to be included when looking at decay of phonon modes [55].

Interaction parts of the Hamiltonian

Electron-photon The interaction of the electrons with the electromagnetic field Eq. (2.15) is in the literature denoted the $\mathbf{A}\cdot\mathbf{p}$-interaction. It is well-known that in the dipole approximation the $\mathbf{A}\cdot\mathbf{p}$-interaction may be replaced by a $\mathbf{d}\cdot\mathbf{E}_t$-interaction, where $\mathbf{d}_i = -e\mathbf{r}_i$ is the electric dipole operator describing the interaction of light with an electron at $\mathbf{r}_i$, [39]. The dipole approximation is valid when the wavelength of the radiation field is much larger than the characteristic size of the atoms in the solid. Typically optical wavelengths $\sim 400 - 700\,\mathrm{nm}$ are used, and the size of the atoms are on the order of a few ångströms, and the requirement is fulfilled, allowing us to consider the vector field as spatially uniform, $\mathbf{A}(\mathbf{r}, t) \approx \mathbf{A}(t)$. In this case, the interaction Hamiltonian becomes [53],

$$H_{\text{elec-rad}} = -\sum_{i} \mathbf{d}_i \cdot \mathbf{E}_t(t). \tag{2.37}$$

The transverse electric field is the sum of a classical and a quantized field, $\mathbf{E}_t(t) = \mathbf{E}_{t,\mathrm{clas}}(t) + \mathbf{E}_{t,\mathrm{QM}}$, where the quantized part is time independent in the Schrödinger picture.

The semi-classical interaction between electrons and a classical field is denoted $U(t)$ and is determined using Eq. (2.29),

$$U(t) = \int \mathrm{d}\mathbf{r}\, \Psi^\dagger(\mathbf{r}) \mathbf{E}_{t,\mathrm{clas}}(t) \Psi(\mathbf{r}) \tag{2.38}$$

$$= E_{\mathrm{clas}}(t) \sum_{\nu_a \nu_b} d_{\nu_a \nu_b} c^\dagger_{\nu_a} c_{\nu_b}, \tag{2.39}$$

in which the projected dipole matrix element has been introduced,

$$d_{\nu_a \nu_b} = \int \mathrm{d}\mathbf{r}\, \psi^*_{\alpha_a}(\mathbf{r}) e\mathbf{r} \cdot \boldsymbol{\xi}_{\mathbf{E}_{\mathrm{clas}}} \psi_{\alpha_b}(\mathbf{r}) \delta_{\sigma_a, \sigma_b}. \tag{2.40}$$

Here $\boldsymbol{\xi}_{\mathbf{E}_{\mathrm{clas}}}$ is the polarisation vector of $\mathbf{E}_{\mathrm{clas}}$, and again the spin-dependence has been extracted from the wavefunctions by writing $\psi_\nu = \psi_\alpha \chi_\sigma$, where χ_σ describes the spin. The time dependence appearing in $U(t)$ is not to be understood in the Heisenberg picture, but rather describes any explicit time dependence in the classical field.

The interaction due to the quantized part of the electrical field is obtained by using the expression for the quantized field in Eq. (2.32). With Eq. (2.29) we obtain in the Schrödinger picture

$$H_{\text{elec-rad}} = \int \mathrm{d}\mathbf{r}\, \Psi^\dagger(\mathbf{r}) e\mathbf{r} \cdot \mathbf{E}_{t,\mathrm{QM}} \Psi(\mathbf{r}) \tag{2.41}$$

$$= \sum_{\nu_a \nu_b n} \hbar g^n_{\nu_a \nu_b} c^\dagger_{\nu_a} c_{\nu_b} (a^\dagger_n + a_n), \tag{2.42}$$

where $\hbar g^n_{\nu_a \nu_b}$ describes the coupling strength,

$$\hbar g^n_{\nu_a \nu_b} = w_n \mathcal{E}_n \int \mathrm{d}\mathbf{r}\, \psi^*_{\alpha_a}(\mathbf{r}) e\mathbf{r} \cdot \boldsymbol{\xi}_{\mathbf{w}_n} \psi_{\alpha_b}(\mathbf{r}) \delta_{\sigma_a \sigma_b}. \tag{2.43}$$

Here $w_n = |\mathbf{w}_n|$ is independent of $\mathbf{r}$ and may be evaluated everywhere due to the dipole approximation.

Electron-phonon The electron-phonon interaction is described by the interaction of the electrons with the ion displacements in the lattice and is given by Eq. (2.16), which may be written as

$$H_{\text{elec-ph}}(\{\mathbf{r}_i\}) = \sum_i H_{\text{elec-ph}}(\mathbf{r}_i) \tag{2.44}$$

where $H_{\text{elec-ph}}(\mathbf{r}_i)$ contains the quantized ionic displacement operator $\mathbf{u}$. Following a standard derivation as in [47, sec. 1.1] or [46, sec. 3.6], the form of the quantized displacement vector in is

$$\mathbf{u}(\mathbf{r}) = \mathrm{i} \sum_\mu \sqrt{\frac{\hbar}{2\rho V \omega_\mu(\mathbf{k})}} \boldsymbol{\xi}_\mu \left(b^\dagger_{\overline{\mu}} + b_\mu \right) \mathrm{e}^{\mathrm{i}\mathbf{k}\cdot\mathbf{r}}, \tag{2.45}$$

where $\overline{\mu} = (-\mathbf{k}, \lambda)$ with λ being the polarization quantum number. Here $\mathbf{u}(\mathbf{r})$ has to be evaluated from the equilibrium points of the ions, $\mathbf{r} = \mathbf{R}^{(0)}_j$. Furthermore ρ is the crystal density, V is

the normalization volume of the phonon modes, $\boldsymbol{\xi}_\mu$ is the polarization vector, and $\omega_\mu(\mathbf{k})$ is the phonon frequency.

Using Eq. (2.29) we may express the interaction using the second quantization formalism,

$$H_{\text{elec-ph}} = \int \mathrm{d}\mathbf{r}\, \Psi^\dagger(\mathbf{r}) H_{\text{elec-ph}}(\mathbf{r}) \Psi(\mathbf{r}) \tag{2.46}$$

$$= \sum_{\nu_a \nu_b, \mu} M^\mu_{\nu_a \nu_b} c^\dagger_{\nu_a} c_{\nu_b} \left(b_\mu + b^\dagger_{\bar{\mu}} \right), \tag{2.47}$$

where the coupling strength is given by

$$M^\mu_{\nu_a \nu_b} = \mathrm{i} \sqrt{\frac{\hbar}{2\rho V \omega_\mu(\mathbf{k})}} \sum_j \mathrm{e}^{\mathrm{i}\mathbf{k}\cdot\mathbf{R}^{(0)}_j} \int \mathrm{d}\mathbf{r}\, \psi^*_{\alpha_a}(\mathbf{r}) \boldsymbol{\xi}_\mu \cdot \boldsymbol{\nabla}_{\mathbf{r}} \left[\frac{e q_j}{4\pi\epsilon} \frac{1}{|\mathbf{r} - \mathbf{R}^{(0)}_j|} \right] \psi_{\alpha_b}(\mathbf{r}) \delta_{\sigma_a \sigma_b}. \tag{2.48}$$

Electron-electron The electron-electron interaction given by Eq. (2.17) and may be written as

$$H_{\text{elec-elec}}(\{\mathbf{r}\}) = \frac{1}{2} \sum_{i \neq j} H_{\text{elec-elec}}(\mathbf{r}_i - \mathbf{r}_j). \tag{2.49}$$

In second quantization this may be expressed as

$$H_{\text{elec-elec}} = \frac{1}{2} \sum_{\nu_i \nu_j \nu_k \nu_l} V_{\nu_i \nu_j, \nu_k \nu_l} c^\dagger_{\nu_i} c^\dagger_{\nu_j} c_{\nu_l} c_{\nu_k}, \tag{2.50}$$

where $V_{\nu_i \nu_j, \nu_k \nu_l}$ is the Coulomb matrix element given by Eq. (2.22),

$$V_{\nu_c \nu_d \nu_a \nu_b} = \int \mathrm{d}\mathbf{r} \int \mathrm{d}\mathbf{r}'\, \psi^*_{\alpha_c}(\mathbf{r}) \psi^*_{\alpha_d}(\mathbf{r}') V(\mathbf{r} - \mathbf{r}') \psi_{\alpha_a}(\mathbf{r}) \psi_{\alpha_b}(\mathbf{r}') \delta_{\sigma_i, \sigma_k} \delta_{\sigma_j, \sigma_l}, \tag{2.51}$$

where the spin dependency notationally have been pulled out of the wavefunctions to clarify with the Kronecker-δs, that the Coulomb interaction is diagonal in spin.

The total Hamiltonian in second quantization

All elements of the Hamiltonian

$$H(t) = H_0 + H_{\text{int}} + U(t), \tag{2.52}$$

have been expressed in second quantization and is summed up in the table below.

Non-interacting part $H_0 = H_{0,\text{elec}} + H_{0,\text{rad}} + H_{0,\text{ph}}$	**Interacting part** $H_{\text{int}} = H_{\text{elec-elec}} + H_{\text{elec-rad}} + H_{\text{elec-ph}}$
$H_{0,\text{elec}} = \sum_\nu \hbar\omega_\nu c^\dagger_\nu c_\nu$	$H_{\text{elec-elec}} = \frac{1}{2} \sum_{\nu_i \nu_j \nu_k \nu_l} V_{\nu_i \nu_j, \nu_k \nu_l} c^\dagger_{\nu_i} c^\dagger_{\nu_j} c_{\nu_l} c_{\nu_k}$
$H_{0,\text{rad}} = \sum_n \hbar\omega_n \left(a^\dagger_n a_n + \frac{1}{2} \right)$	$H_{\text{elec-rad}} = \sum_{\nu_a \nu_b n} \hbar g^n_{\nu_a \nu_b} c^\dagger_{\nu_a} c_{\nu_b} (a^\dagger_n + a_n)$
$H_{0,\text{ph}} = \sum_\mu \hbar\omega_\mu \left(b^\dagger_\mu b_\mu + \frac{1}{2} \right)$	$H_{\text{elec-ph}} = \sum_{\nu_a \nu_b, \mu} M^\mu_{\nu_a \nu_b} c^\dagger_{\nu_a} c_{\nu_b} \left(b_\mu + b^\dagger_{\bar{\mu}} \right)$
Externally applied field	$U(t) = E_{\text{clas}}(t) \sum_{\nu_a \nu_b} d_{\nu_a \nu_b} c^\dagger_{\nu_a} c_{\nu_b}$

The parts of the Hamiltonian describing the photons look similar to the part describing the phonon due to the bosonic nature of both particle types.

2.2 Carrier-phonon interaction

Phonons are quantizations of lattice vibrations, and for crystals with two or more atoms per primitive basis such as GaAs, the phonons may divided into two classes, acoustic and optical phonons, see e.g. [54, chap. 5]. Each of these classes are divided into transverse (respectively TA and TO) phonons and longitudinal (LA and LO) phonons. They are characterized by their dispersion properties seen in Fig. 2.1a: For the acoustic phonons, the ions move in phase with each other. In the long-wavelength limit (close to the center of the Brillouiin zone, Γ) the acoustic phonons have a linear dependence between frequency and wavevector, and the frequency tends to zero for $\lambda \to \infty$ corresponding to sound waves in a lattice, which is the reason for calling them ,,acoustic phonons". In this limit, the speed of the acoustic and transverse phonons may be extracted as the slope of the dispersion curve, which gives a larger sound speed for the LA-phonons than for the TA-phonons.

Optical phonons on the other hand are called optical because they may be excited by infrared radiation. They correspond to a vibrational mode in an ionic crystal when the differently charged ions oscillate out of phase, creating a time-varying electrical dipole moment. Thus optical phonons induce a relative displacement inside the primitive unit cell of the crystal in contrast to the acoustic phonons that are more like a macroscopic strain of the crystal.

The carrier-phonon interaction can be described by three major mechanisms [47]: Deformation potential, piezoelectric interaction and polar coupling. Below we give a description of the three types of interactions, considering that the interaction may happen with both electrons and holes.

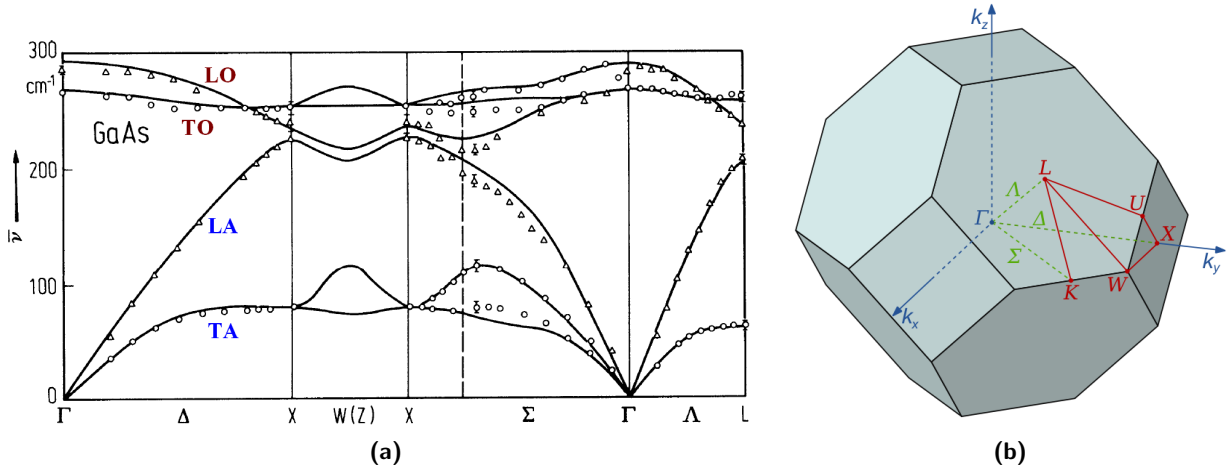

Figure 2.1: **(a)** Phonon dispersion curve for GaAs from calculations (solid line) and experimental points found using neutron diffraction [56]. The plot shows the angular frequency as a function of the wavevector $\mathbf{k}$. In some regions the TA and TO branches split into two different branches. **(b)** GaAs crystallizes in a Zinc-blende structure and is in reciprocal space described by a truncated octahedron shaped Brillouin zone as seen in the figure with indications of some high-symmetry points (picture from Wikipedia.org).

2.2.1 Deformation potential

The concept of deformation potentials was first introduced by Bardeen & Shockley in 1950 [57] and has been discussed and developed in many articles and books, ex. [58, 59]. The deformation potential describes local site deformations that are caused by dilations associated with acoustic lattice waves. For long-wavelength acoustic phonons, the displacement corresponds to a deformation of the crystal leading to a shift of the electronic bands. The deformation potential is defined as the energy change per unit strain of an electronic level.

Following derivations in [60, 61, 62, 63, 64], we for simplicity consider a non-degenerate band which appears e.g. at Γ in Fig. 2.1b. The dilation covers both rotation and strain, but since a rotation of the crystal does not change the energy bands, the energy shift depends only on the strain. To the leading order, the energy shift is proportional to the relative volume change δV, and we may write the the interaction Hamiltonian as

$$H_{\mathrm{e/h}}^{(\mathrm{DP})} = \Delta E_{\mathrm{c/v}} = D_{\mathrm{e/h}} \frac{\delta V}{V} = D_{\mathrm{e/h}} \mathrm{Tr}\{\hat{\sigma}\}, \tag{2.53}$$

where $D_{\mathrm{e/h}}$ is the deformation potential constant for the electron/hole, V is the volume of a unit cell of the crystal, and $\mathrm{Tr}\{\hat{\sigma}\}$ is the trace of the strain tensor. When $D_{\mathrm{e/h}} < 0$, the bottom of the energy bands are shifted toward higher energies in when the crystal is compressed.

The strain tensor for a homogeneous material, assuming that the strains are small and obey Hooke's law, has the elements [54, chap. 3],

$$\sigma_{ij} = \frac{1}{2}\left(\frac{\partial u_i}{\partial r_j} + \frac{\partial u_j}{\partial r_i}\right), \tag{2.54}$$

where u_i is the vector components of the local displacement field of the phonons, $\mathbf{u}(\mathbf{r})$. This allows us to write

$$H_{\mathrm{e/h}}^{(\mathrm{DP})} = D_{\mathrm{e/h}}\left(\frac{\partial u_x}{\partial x} + \frac{\partial u_y}{\partial y} + \frac{\partial u_z}{\partial z}\right) = D_{\mathrm{e/h}} \boldsymbol{\nabla} \cdot \mathbf{u}(\mathbf{r}), \tag{2.55}$$

with $\mathbf{u}(\mathbf{r}) = (u_x(\mathbf{r}), u_y(\mathbf{r}), u_z(\mathbf{r}))$ being the displacement as given in Eq. (2.45).

The displacement may be divided into a longitudinal variation described by $\mathbf{u}_{\mathrm{long}}(\mathbf{r}) = (u_x(x), u_y(y), u_z(z))$ and a transverse variation $\mathbf{u}_{\mathrm{trans}}(\mathbf{r}) = (u_x(y,z), u_y(x,z), u_z(x,y))$. As we see from Eq. (2.55), only the *longitudinal acoustic phonons* contribute to $\boldsymbol{\nabla} \cdot \mathbf{u}(\mathbf{r})$, and the final Hamiltonian in coordinate representation is

$$H_{\mathrm{e/h}}^{(\mathrm{DP})}(\mathbf{r}) = -D_{\mathrm{e/h}} \sum_{\mathbf{k}} k \sqrt{\frac{\hbar}{2\rho V \omega_{\mathrm{LA}}(\mathbf{k})}} \left(b_{-\mathbf{k},\mathrm{LA}}^{\dagger} + b_{\mathbf{k},\mathrm{LA}}\right) \mathrm{e}^{\mathrm{i}\mathbf{k}\cdot\mathbf{r}}. \tag{2.56}$$

In the literature the minus is as standard adapted into the value of $D_{\mathrm{e/h}}$, such that the usually given values of the deformation potential already contains this minus[1] [60]. We will do that from now on. Transforming this into second quantization with respect to the electron/hole

[1] In some publications, other sign conventions are used, so it is always important to check this in details.

states using Eq. (2.29), gives

$$H_{\mathrm{e/h}}^{(\mathrm{DP})} = \sum_{\nu\nu'} \langle \nu | H_{\mathrm{e/h}}^{(\mathrm{DP})}(\mathbf{r}) | \nu' \rangle c_\nu^\dagger c_{\nu'} \tag{2.57}$$

$$= \sum_{\nu\nu'} \int \mathrm{d}\mathbf{r}\, \psi_{\mathrm{e/h},\nu'}^*(\mathbf{r}) H_{\mathrm{e/h}}^{(\mathrm{DP})}(\mathbf{r}) \psi_{\mathrm{e/h},\nu'}(\mathbf{r}) c_\nu^\dagger c_{\nu'} \tag{2.58}$$

$$= D_{\mathrm{e/h}} \sum_{\mathbf{k},\nu\nu'} k \sqrt{\frac{\hbar}{2\rho V \omega_{\mathrm{LA}}(\mathbf{k})}} \mathcal{F}_{\mathrm{e/h},\nu\nu'}(\mathbf{k}) \left(b_{-\mathbf{k},\mathrm{LA}}^\dagger + b_{\mathbf{k},\mathrm{LA}} \right) c_\nu^\dagger c_{\nu'}. \tag{2.59}$$

where the form factor is

$$\mathcal{F}_{\mathrm{e/h},\nu\nu'}(\mathbf{k}) = \int \mathrm{d}\mathbf{r}\, \psi_{\mathrm{e/h},\nu}^*(\mathbf{r}) \psi_{\mathrm{e/h},\nu'}(\mathbf{r}) \mathrm{e}^{\mathrm{i}\mathbf{k}\cdot\mathbf{r}}. \tag{2.60}$$

The form factor has the symmetry properties $\mathcal{F}_{\mathrm{e/h},\nu\nu'}(\mathbf{k}) = \mathcal{F}_{\mathrm{e/h},\nu'\nu}^*(-\mathbf{k})$.

Comparing Eq. (2.59) with the general form of the electron-phonon interaction in Eq. (2.47), we find the interaction matrix element to be given by

$$M_{\mathrm{e/h},\nu\nu'}^{(\mathrm{DP})}(\mathbf{k}) = D_{\mathrm{e/h}} k \sqrt{\frac{\hbar}{2\rho V \omega_{\mathrm{LA}}(\mathbf{k})}} \mathcal{F}_{\mathrm{e/h},\nu\nu'}(\mathbf{k}), \tag{2.61}$$

At some other symmetry points in the crystal, where the bands are degenerate, e.g. at X or L point in Fig. 2.1b, the $D_{\mathrm{e/h}}$ in Eq. (2.53) is not a scalar but rather a tensor and more complex equations involving also TA phonons has to be considered [55].

2.2.2 Piezoelectric interaction

In non-centrosymmetric materials the presence of stress induces a macroscopic electric polarization, and this effect is know as the piezo-electric effect. The effects also works the other way, such that a acoustic phonon will induce a polarization which will interact will the electrons, and this is called the piezoelectric interaction. If the strain tensor $\hat{\sigma}$ describes the crystal deformation, the piezoelectric polarisation is $\mathbf{P} = \hat{d}\hat{\sigma}$, where $\hat{d}$ is the piezoelectric tensor [63].

The piezoelectric interaction is described in details in e.g. [47, 63], and we will only provide the result written in second quantization,

$$H_{\mathrm{e/h}}^{(PE)} = \sum_{\mathbf{k},s,\nu\nu'} M_{\mathrm{e/h},\nu\nu',s}^{(PE)}(\mathbf{k}) \left(b_{-\mathbf{k},s}^\dagger + b_{\mathbf{k},s} \right) c_\nu^\dagger c_{\nu'}, \tag{2.62}$$

where

$$M_{\mathrm{e/h},\nu\nu',s}^{(PE)}(\mathbf{k}) = \mp \mathrm{i} \sqrt{\frac{\hbar}{2\rho V \omega_s(\mathbf{k})}} \frac{de}{\epsilon_0 \epsilon_1} M_s(\hat{\mathbf{k}}) \mathcal{F}_{\mathrm{e/h},\nu\nu'}(\mathbf{k}), \tag{2.63}$$

$d = \{\hat{d}\}_{xyz} = \{\hat{d}\}_{yzx} = \{\hat{d}\}_{zxy}$ for a zinc-blende structure, and $M_s(\hat{\mathbf{k}})$ is a unitless factor depending on the phonon polarization. The form factor is as given in Eq. (2.60). The index s indicates eiter TA or LA phonons in contrast to the deformation potential interaction, where only LA phonons are present.

2.2.3 Fröhlich interaction

Polar coupling appears only in polar crystals, which have two or more atoms in the primitive unit cell with different charge. When an optical field is present, different ions move out of phase and oscillate in different directions creating a polarization field, which scatters the electrons. Only the LO and not the TO phonons set up a field when vibrating that is strong enough for the electrons to couple to. A derivation of the Hamiltonian for this so-called Fröhlich interaction may be found in [47, 65, 63] and is

$$H_{\mathrm{e/h}}^{(Fr)} = \sum_{\mathbf{k},s,\nu\nu'} c_{\nu}^{\dagger} c_{\nu'} M_{\mathrm{e/h},\nu\nu',s}^{(Fr)}(\mathbf{k}) \left(b_{\mathbf{k},\mathrm{LO}} + b_{-\mathbf{k},\mathrm{LO}}^{\dagger} \right), \tag{2.64}$$

where

$$M_{\mathrm{e/h},\nu\nu'}^{(Fr)}(\mathbf{k}) = \mp \frac{e}{k} \sqrt{\frac{\hbar\omega_{\mathrm{LO}}(\mathbf{k})}{2V\epsilon_0\bar{\epsilon}}} \mathcal{F}_{\mathrm{e/h},\nu\nu'}(\mathbf{k}). \tag{2.65}$$

Here $\omega_{\mathrm{LO}}(\mathbf{k})$ is the angular frequency of the LO-phonon, and $\bar{\epsilon} = (1/\epsilon_\infty - 1/\epsilon_s)^{-1}$ is the effective dielectric constant with ϵ_∞ and ϵ_s being respectively the high-frequency and static dielectric constant.

2.3 Summary and discussion

In this chapter we have sketched the derivation of the various parts of the Hamiltonian for a many-body semiconductor system describing interactions between electrons, photons, and phonons.

The three major electron-phonon are introduced to describe the various kinds of electron-phonon interaction mechanisms: The deformation potential coupling, the piezoelectric interaction, and the Fröhlich interaction. The matrix elements describing these interactions all contain the same form factor describing the interaction of the electronic confinement with bulk phonons.

In a QD structure, the Fröhlich coupling give rise to phonon sidebands in the absorption spectrum well separated from the zero phonon line, whereas the acoustical phonons introduce a broadening of the zero phonon line [66]. We only consider a phonon-assisted coupling between the QD and a cavity, where the detuning is much smaller than the energy of the LO-phonons, and thus we will neglect the Fröhlich coupling in our calculations.

The piezoelectric interaction depends strongly on the separation of the electron and hole wavefunctions. In GaAs the deformation potential is dominating the piezoelectric coupling, but a material like GaN possesses strong polarisation charges at the interfaces which gives a strong build in polarisation, in which the piezoelectric interaction will be much stronger than the deformation potential coupling [42]. In our calculations we consider GaAs as bulk substrate, in which case it is reasonable to disregard the piezoelectric coupling too.

Chapter 3

Equations of Motion

The dynamics of a quantum mechanical system is determined by the time-dependent Schrödinger equation,

$$\mathrm{i}\hbar\partial_t|\psi(t)\rangle = H(t)|\psi(t)\rangle, \tag{3.1}$$

with $|\psi(t)\rangle$ being the state vector, and where $H(t)$ in general may have an explicit time dependence. When few particles are considered, Eq. (3.1) may be solved by expanding the Hamiltonian and wavefunction into a many-particle Hilbert space, which converts the problem into a system of linear differential equations.

For an open quantum system, where a small system interacts with a many-body environment, a standard approach to determine the system dynamics is the quantum master-equation approach [67]. The environment is modelled as a reservoir, and the reduced density matrix for the system is obtained by tracing out the reservoir degrees of freedom.

In Section 3.1 we give a brief review of basic quantum dynamics based on [53, 46]. In Section 3.2 we derive specific equations of motion for a quantum system interacting weakly with a large bosonic reservoir, keeping in mind that this general theory later on is going to be applied to a QD-cavity system interaction with a phonon reservoir. Our approach has similarities with the standard Markovian quantum master-equation approach, but we obtain non-Markovian time-local scattering terms which still contain memory. This method also has similarities with the more advanced "time convolutionless approach" [68]. The derivations follow [69] and standard textbooks [70, 71, 72].

3.1 Basic quantum dynamics theory

If an initial state is given at a time $t = t_0$, a solution to the time-dependent Schrödinger equation, Eq. (3.1), may formally be described by a time evolution operator,

$$|\psi(t)\rangle = U(t, t_0)|\psi(t_0)\rangle, \tag{3.2}$$

From Eq. (3.1) we see by insertion that $U(t, t_0)$ must obey

$$\mathrm{i}\hbar\partial_t U(t, t_0) = H(t)U(t, t_0). \tag{3.3}$$

with the initial condition $U(t_0, t_0) = I$, with I being the identity operator, corresponding to an unchanged system. Provided that $H(t)$ is Hermitian and using Eq. (3.3), we have

$$\mathrm{i}\hbar\partial_t \left\{U^\dagger U\right\} = -U^\dagger H^\dagger U + U^\dagger H U = 0. \tag{3.4}$$

This means that $U^\dagger U$ has to be constant, and due to the initial condition we have

$$U^\dagger(t,t_0)U(t,t_0) = I, \tag{3.5}$$

or, said in another way, that $U(t,t_0)$ is a unitary operator.

For a time-dependent Hamiltonian, U may be expressed as a time-ordered exponential [46],

$$U(t,t_0) = \hat{T}\left(\mathrm{e}^{-\mathrm{i}\hbar^{-1}\int_{t_0}^{t}\mathrm{d}t'\,H(t')}\right), \tag{3.6}$$

where $\hat{T}$ is the chronological time-ordering operator, which orders the product of time-dependent operators such their time argument increase from right to left[1]. For an isolated physical system, which is a system that do not interact with the environment at all, the Hamiltonian is time-independent. For time-independent Hamiltonians, Eq. (3.6) reduces to the well-known expression

$$U(t,t_0) = \mathrm{e}^{-\mathrm{i}\hbar^{-1}H(t-t_0)}. \tag{3.7}$$

If the considered system is not in a pure quantum state but instead in a mix of different quantum states, we characterize the ensemble of quantum states by the density matrix operator $\rho(t)$. We consider the time evolution of such a system, which at initial time $t = t_0$ is described by

$$\rho(t_0) = \sum_a w_a|\psi_a(t_0)\rangle\langle\psi_a(t_0)|. \tag{3.8}$$

The initial state is a mix of normalized quantum states, where the probability of the system to be in a given state $|\psi_a\rangle$ is equal to the positive weight factor w_a, $\sum_a w_a = 1$. Each state vector evolves according to Eq. (3.2), so at time t, the system will be in the state

$$\rho(t) = \sum_a w_a U(t,t_0)|\psi_a(t_0)\rangle\langle\psi_a(t)|U^\dagger(t,t_0) = U(t,t_0)\rho(t_0)U^\dagger(t,t_0). \tag{3.9}$$

By simple differentiation of $\rho(t)$ and exploitation of Eq. (3.3), we arrive an equation of motion for the density operator

$$\frac{\mathrm{d}\rho(t)}{\mathrm{d}t} = \frac{1}{\mathrm{i}\hbar}\left[H(t),\rho(t)\right]. \tag{3.10}$$

This is often referred to as the von Neumann equation. Constant terms in H commutes with $\rho(t)$ and thus do not affect the dynamics of the system but only contribute to an energy shift.

A natural initial state for a solid-state system is the thermal equilibrium, described by the density matrix

$$\rho = \frac{\exp(-\beta H)}{\mathrm{Tr}\{\exp(-\beta H)\}}, \tag{3.11}$$

where $\beta = 1/(k_B T)$ and $\mathrm{Tr}\{\cdot\} = \sum_n \langle n|\cdot|n\rangle$ indicates the trace, where the sum is over all possible states.

[1] An elaborate description is provided in many textbooks, e.g. [46].

The Schrödinger, Heisenberg, and Interaction Picture

What is measured in experiments is the expectation value of a physical observable A. It may be calculated using the density matrix of the system and the time evolution operator from Eq. (3.6),

$$\begin{aligned}\langle A(t)\rangle &= \mathrm{Tr}\left[A\rho(t)\right] && (3.12)\\ &= \mathrm{Tr}\left[AU(t,t_0)\rho(t_0)U^\dagger(t,t_0)\right] = \mathrm{Tr}\left[U^\dagger(t,t_0)AU(t,t_0)\rho(t_0)\right] && (3.13)\\ &= \mathrm{Tr}\left[A_{\mathrm{Heis}}(t)\rho(t_0)\right], && (3.14)\end{aligned}$$

where we exploit the invariance of the trace of a product with respect to cyclic permutation. Eqs. (3.12) and (3.14) demonstrate two different frames for calculating the same expectation value. In the *Schrödinger picture* in Eq. (3.12), the time-dependence is contained in the state operator (wave function), and the time evolution is governed by the equation of motion in the Schrödinger picture, Eq. (3.10), in which $H(t)$ is given in the Schrödinger picture. In contradiction to this frame is the *Heisenberg picture* illustrated by Eq. (3.14), where the state operator is independent of time, and the time evolution is contained in the Heisenberg operator $A_{\mathrm{Heis}}(t)$, given by

$$A_{\mathrm{Heis}} = U^\dagger(t,t_0)AU(t,t_0). \tag{3.15}$$

for the Schrödinger operator A. The Schrödinger and Heisenberg pictures are equivalent pictures giving the same expectation value of A, since $\langle A(t)\rangle$ only depends on the relative motion of A and ρ.

A third frame is generally known as the *interaction picture* (IP), which typically is used when H contains a part H_0, with know energy eigen-solutions $\{\varepsilon_n, |n\rangle\}$, and a small perturbation $V(t)$ that may be time dependent,

$$H(t) = H_0(t) + V(t), \qquad H_0(t)|n\rangle = \varepsilon_n|n\rangle. \tag{3.16}$$

The main point by using the IP is to separate trivial time evolution due to H_0 from the total Hamiltonian. This is achieved by applying the unitary time evolution operator U as described in Eq. (3.6) with $H(t)$ replaced by $H_0(t)$ which we indicate notationally as $U_{H_0(t)}$. An operator in the IP is thus given as

$$\tilde{A}(t) = U^\dagger_{H_0(t)}(t,t_0)AU_{H_0(t)}(t,t_0). \tag{3.17}$$

To clarify the purpose of the IP description, we calculate the time derivative of a state $|\tilde{\psi}(t)\rangle = U^\dagger_{H_0(t)}|\psi(t)\rangle$ described in the IP,

$$\mathrm{i}\hbar\partial_t|\tilde{\psi}(t)\rangle = \mathrm{i}\hbar\partial_t\{U^\dagger_{H_0(t)}(t,t_0)\}|\psi(t)\rangle + \mathrm{i}\hbar U^\dagger_{H_0(t)}(t,t_0)\partial_t\{|\psi(t)\rangle\}. \tag{3.18}$$

Using Eqs. (3.3) and (3.1) and the fact that $H_0(t)$ and $U_{H_0(t)}(t,t_0)$ commute, we get

$$\begin{aligned}\mathrm{i}\hbar\partial_t|\tilde{\psi}(t)\rangle &= -U^\dagger_{H_0(t)}(t,t_0)H_0(t)|\psi(t)\rangle + U^\dagger_{H_0(t)}(t,t_0)H(t)|\psi(t)\rangle && (3.19)\\ &= U^\dagger_{H_0(t)}(t,t_0)\Big(H(t) - H_0(t)\Big)|\psi(t)\rangle && (3.20)\\ &= \tilde{V}(t)|\tilde{\psi}(t)\rangle, && (3.21)\end{aligned}$$

where we exploit the unitarity of U as shown in Eq. (3.5) and furthermore Eq. (3.17) to write $V(t)$ in the IP.

In the limit of an infinitely small perturbation, $V(t) \approx 0$, the IP is similar to the Heisenberg picture. In the limit of $H_0 = 0$, $U_{H_0(t)}(t, t_0)$ is equal to the identity operator, and the IP is similar to the Schrödinger picture. The choice on which of the three pictures to use, depends on the specific Hamiltonian for a given problem.

3.2 Equations of motion

In this section we introduce the equation of motion for a system interacting with a large bosonic reservoir. The main focus in the derivation is to trace out the reservoir degrees of freedom and only consider a reduced density matrix description.

The Hilbert space describing the total system, $\mathcal{H}_{\text{total}} = \mathcal{H}_{\text{S}} \otimes \mathcal{H}_{\text{R}}$, is the product of the subspace belonging to the system and the subspace of the reservoir. From the density operator $\chi(t)$ of the total system $\text{S} \oplus \text{R}$, the reduced density opreator for the system can be obtained by tracing out the reservoir as $\rho(t) = \text{Tr}_{\text{R}}\{\chi(t)\}$. If $\hat{O}$ is an operator in the system Hilbert space, S, the average value of $\hat{O}$ is

$$\langle \hat{O} \rangle = \text{Tr}_{\text{R}\oplus\text{S}} \left\{ \hat{O}\chi(t) \right\} = \text{Tr}_{\text{S}} \left\{ \hat{O}\text{Tr}_{\text{R}}\{\chi(t)\} \right\} = \text{Tr}_{\text{S}} \left\{ \hat{O}\rho(t) \right\}. \tag{3.22}$$

Thus to calculate average values of system operators we only need to know the reduced density matrix, $\rho(t)$, and not the full, $\chi(t)$.

We separate the Hamiltonian into three different parts: A Hamiltonian for the system, H_{S}, a part only connected to the reservoir, H_{R}, and a last part H_{SR} describing the interaction between the system and the reservoir,

$$H = H_{\text{S}} + H_{\text{R}} + H_{\text{SR}} = H_0 + H_{\text{SR}}. \tag{3.23}$$

where we limit ourselves to only consider the case of a time-independent Hamiltonian. The time evolution of the total density matrix in the Schrödinger picture is given by

$$\partial_t \chi(t) = \frac{1}{\text{i}\hbar} [H, \chi(t)]. \tag{3.24}$$

To separate the time evolution described by H_0 from the one arising from the interaction H_{SR}, we describe $\chi(t)$ in the interaction picture,

$$\tilde{\chi}(t) = \text{e}^{\frac{\text{i}}{\hbar}H_0 t} \chi(t) \text{e}^{\frac{-\text{i}}{\hbar}H_0 t}. \tag{3.25}$$

If the interaction is weak, the interaction picture provides a good angle for examining the slow motion stemming from H_{SR} because the fast motion due to H_0 is suppressed. Differentiation of $\tilde{\chi}(t)$ gives

$$\partial_t \tilde{\chi}(t) = -\frac{1}{\text{i}\hbar} \text{e}^{\frac{\text{i}}{\hbar}H_0 t} [H_0, \chi(t)] \, \text{e}^{\frac{-\text{i}}{\hbar}H_0 t} + \text{e}^{\frac{\text{i}}{\hbar}H_0 t} \partial_t \{\chi(t)\} \text{e}^{\frac{-\text{i}}{\hbar}H_0 t}. \tag{3.26}$$

By using Eq. (3.24) and that unitary properties of the operator $\text{e}^{-\frac{-\text{i}}{\hbar}H_0 t}$ (described in Eq. (3.7)), we arrive at

$$\begin{aligned} \partial_t \tilde{\chi}(t) &= -\frac{1}{\text{i}\hbar} \text{e}^{\frac{\text{i}}{\hbar}H_0 t} [H_0, \chi(t)] \, \text{e}^{\frac{-\text{i}}{\hbar}H_0 t} + \frac{1}{\text{i}\hbar} \left[\text{e}^{\frac{\text{i}}{\hbar}H_0 t} (H_0 + H_{\text{SR}}) \text{e}^{\frac{-\text{i}}{\hbar}H_0 t}, \text{e}^{\frac{\text{i}}{\hbar}H_0 t} \chi(t) \text{e}^{\frac{-\text{i}}{\hbar}H_0 t} \right] \\ &= \frac{1}{\text{i}\hbar} \left[\tilde{H}_{\text{SR}}(t), \tilde{\chi}(t) \right], \end{aligned} \tag{3.27}$$

where

$$\tilde{H}_{\mathrm{SR}}(t) = \mathrm{e}^{\frac{\mathrm{i}}{\hbar}H_0 t} H_{\mathrm{SR}} \mathrm{e}^{\frac{-\mathrm{i}}{\hbar}H_0 t}. \tag{3.28}$$

We may formally integrate Eq. (3.27),

$$\tilde{\chi}(t) = \tilde{\chi}(t_0) + \frac{1}{\mathrm{i}\hbar}\int_{t_0}^{t} \mathrm{d}t' \, \left[\tilde{H}_{\mathrm{SR}}(t'), \tilde{\chi}(t')\right]. \tag{3.29}$$

By inserting this back into Eq. (3.27), we get

$$\partial_t \tilde{\chi}(t) = \frac{1}{\mathrm{i}\hbar}\left[\tilde{H}_{\mathrm{SR}}(t), \tilde{\chi}(t_0)\right] - \frac{1}{\hbar^2}\int_{t_0}^{t} \mathrm{d}t' \, \left[\tilde{H}_{\mathrm{SR}}(t), \left[\tilde{H}_{\mathrm{SR}}(t'), \tilde{\chi}(t')\right]\right]. \tag{3.30}$$

We consider the expression for $\rho(t)$ in the interaction picture,

$$\tilde{\rho}(t) = \mathrm{e}^{\frac{\mathrm{i}}{\hbar}H_{\mathrm{S}} t} \rho(t) \mathrm{e}^{-\frac{\mathrm{i}}{\hbar}H_{\mathrm{S}} t}, \tag{3.31}$$

noting that $\rho(t)$ in the interaction picture only is described by the free Hamiltonian of the *system* and not the total H_0 as in Eq. (3.25). Exploiting the cyclic properties of the trace, we have

$$\begin{aligned}
\mathrm{Tr}_{\mathrm{R}}\left\{\tilde{\chi}(t)\right\} &= \mathrm{Tr}_{\mathrm{R}}\left\{\mathrm{e}^{\frac{\mathrm{i}}{\hbar}H_0 t}\chi(t)\mathrm{e}^{\frac{-\mathrm{i}}{\hbar}H_0 t}\right\} && (3.32)\\
&= \mathrm{e}^{\frac{\mathrm{i}}{\hbar}H_{\mathrm{S}} t}\mathrm{Tr}_{\mathrm{R}}\left\{\mathrm{e}^{\frac{\mathrm{i}}{\hbar}H_{\mathrm{R}} t}\chi(t)\mathrm{e}^{\frac{-\mathrm{i}}{\hbar}H_{\mathrm{R}} t}\right\}\mathrm{e}^{-\frac{\mathrm{i}}{\hbar}H_{\mathrm{S}} t} && (3.33)\\
&= \mathrm{e}^{\frac{\mathrm{i}}{\hbar}H_{\mathrm{S}} t}\rho(t)\mathrm{e}^{-\frac{\mathrm{i}}{\hbar}H_{\mathrm{S}} t} && (3.34)\\
&= \tilde{\rho}(t). && (3.35)
\end{aligned}$$

Using this we may trace over the reservoir in Eq. (3.30),

$$\partial_t \tilde{\rho}(t) = \frac{1}{\mathrm{i}\hbar}\mathrm{Tr}_{\mathrm{R}}\left\{\left[\tilde{H}_{\mathrm{SR}}(t), \tilde{\chi}(t_0)\right]\right\} - \frac{1}{\hbar^2}\int_{t_0}^{t}\mathrm{d}t' \, \mathrm{Tr}_{\mathrm{R}}\left\{\left[\tilde{H}_{\mathrm{SR}}(t), \left[\tilde{H}_{\mathrm{SR}}(t'), \tilde{\chi}(t')\right]\right]\right\}. \tag{3.36}$$

This expression is exact, but still contains expressions related to the reservoir. To handle these terms, we have to make a couple of assumptions.

Factorization and assumptions

We assume that there is no correlation between the subsystems S and R when the system is turned on at an initial time $t = t_0$, meaning that we may factorize the density operator,

$$\chi(t_0) = \rho(t_0) \otimes R_0, \tag{3.37}$$

where R_0 is the initial density operator for the reservoir.

If the reservoir is very large and the coupling between the system and reservoir is weak, we may assume that the reservoir remains in the thermal state $R_0 = \frac{\exp(-\beta H_{\mathrm{R}})}{\mathrm{Tr}_{\mathrm{R}}\{\exp(-\beta H_{\mathrm{R}})\}}$ at all times, $\beta = 1/(k_B T)$. We assume that H_{SR} contains terms with exactly one bosonic operator, $b^\dagger$ or b, and because R_0 contains only terms with an even number of bosonic operators (seen by a Taylor-expansion of the exponential because H_{R} contains only quadratic terms in bosonic operators),

$\tilde{H}_{\mathrm{SR}}(t)R_0$ will contain an odd number of bosonic operators. In that case $\mathrm{Tr}_{\mathrm{R}}\left\{\tilde{H}_{\mathrm{SR}}(t)R_0\right\} = 0$ due to the fact that $\langle n|b^\dagger|n\rangle = \langle n|b|n\rangle = 0$, and thus the first term in Eq. (3.36) becomes zero.

The assumption that the reservoir remains in the same state furthermore allows us to factorize $\chi(t)$ for all t,

$$\tilde{\chi}(t) = \tilde{\rho}(t) \otimes R_0 + O(H_{\mathrm{SR}}), \tag{3.38}$$

where the deviations from the uncorrelated state should be on the order of H_{SR} due to the weak coupling [72, sec. 1.2].

To proceed we make our first major approximation, the so-called Born approximation. When inserting Eq. (3.38) into Eq. (3.36) we neglect terms higher than second order in H_{SR},

$$\partial_t\tilde{\rho}(t) = -\frac{1}{\hbar^2}\int_{t_0}^{t}\mathrm{d}t'\,\mathrm{Tr}_{\mathrm{R}}\left\{\left[\tilde{H}_{\mathrm{SR}}(t),\left[\tilde{H}_{\mathrm{SR}}(t'),\tilde{\rho}(t')\otimes R_0\right]\right]\right\}. \tag{3.39}$$

This gives a closed integro-differential equation for the density operator $\rho(t)$ of the system in the interaction picture. More detailed analysis of the Born approximation may be carried out by the *projection operator formalism*, see [68] for details.

To further simplify Eq. (3.39), we have to specify the interaction Hamiltonian. Thus we assume that H_{SR} may be written on the form

$$H_{\mathrm{SR}} = \sum_{\nu\nu'} P_{\nu\nu'} \otimes B_{\nu\nu'}, \tag{3.40}$$

where $P_{\nu\nu'}$ is a pure system operator and $B_{\nu\nu'}$ is a pure reservoir operator. Using this notation and omitting the use of $\otimes$, we have

$$\partial_t\tilde{\rho}(t) = -\frac{1}{\hbar^2}\int_{t_0}^{t}\mathrm{d}t'\,\mathrm{Tr}_{\mathrm{R}}\left\{\sum_{\nu_1\nu_2\nu_1'\nu_2'}\left[\tilde{P}_{\nu_1\nu_1'}(t)\tilde{B}_{\nu_1\nu_1'}(t),\left[\tilde{P}_{\nu_2\nu_2'}(t')\tilde{B}_{\nu_2\nu_2'}(t'),\tilde{\rho}(t')R_0\right]\right]\right\}. \tag{3.41}$$

The system part may now be distinguished from the reservoir part. This may be realized by exploiting the cyclic property of the trace and by the procedure of operator averaging defined in Eq. (3.14). The averaging is with respect to the reservoir Hamiltonian only, i.e. $\mathrm{Tr}_{\mathrm{R}}\{AR_0\} = \langle A\rangle$, giving

$$\begin{aligned}\partial_t\tilde{\rho}(t) \;=\; & -\frac{1}{\hbar^2}\int_{t_0}^{t}\mathrm{d}t'\sum_{\nu_1\nu_1'\nu_2\nu_2'}\Big\{\\ & \left[\tilde{P}_{\nu_1\nu_1'}(t)\tilde{P}_{\nu_2\nu_2'}(t')\tilde{\rho}(t') - \tilde{P}_{\nu_2\nu_2'}(t')\tilde{\rho}(t')\tilde{P}_{\nu_1\nu_1'}(t)\right]\langle\tilde{B}_{\nu_1\nu_1'}(t)\tilde{B}_{\nu_2\nu_2'}(t')\rangle\\ & + \left[\tilde{\rho}(t')\tilde{P}_{\nu_2\nu_2'}(t')\tilde{P}_{\nu_1\nu_1'}(t) - \tilde{P}_{\nu_1\nu_1'}(t')\tilde{\rho}(t')\tilde{P}_{\nu_2\nu_2'}(t)\right]\langle\tilde{B}_{\nu_2\nu_2'}(t')\tilde{B}_{\nu_1\nu_1'}(t)\rangle\Big\}.\end{aligned} \tag{3.42}$$

Due to the t' dependence of $\tilde{\rho}$ in the integral, the evolution of $\rho(t)$ is non-Markovian, meaning that the evolution depends on the past due to interaction with earlier states that are reflected back.

The Markov approximation

To handle Eq. (3.42), further approximations have to be introduced. A commonly used but simple approach is the Markov approximation described in [70, 71, 72, 68] which is obtained by the substitution $\tilde{\rho}(t') \to \tilde{\rho}(t)$ such that the time evolution only depends on the present state $\tilde{\rho}(t)$. This assumption seems reasonable if we consider a large bath in thermal equilibrium, since we expect minor changes to be equalized so fast that they do not affect the dynamics of the system. According to [72, sec. 1.2], the Markov approximation is only valid if the correlation time of the reservoir τ_R is small compared to the time scale describing changes in $\tilde{\rho}(t)$ described by H_{SR}. What is important is that the substitution is made in the interaction picture such that Eq. (3.42) still contains memory related to the dynamics caused by H_{S}, and in that way the system behaviour is still non-Markovian in our description.

The Born- and Markov-approximations together are often just denoted the Born-Markov approximations. The important point for the assumptions is that the time scale over which the system varies is much larger than decay times of the reservoir correlation functions.

A non-Markovian description could also be obtained with other theories such as the *time-convolutionless approach* (TCLA), where the time evolution depends solely on the present state of the system, but where the reservoir interaction appears in time-dependent coefficients [68, 73, 74]. The second order result of the TCLA is actually equal to the result in Eq. (3.42), as long as the substitution $\tilde{\rho}(t') \to \tilde{\rho}(t)$ is done in the interaction picture [68].

The dynamics of $\rho(t)$ is only governed by the Hamiltonian of the system, H_{S}, given by the cavity-QD Hamiltonian and may as in Eq. (3.6) be described using the unitary operator

$$U_{\mathrm{S}}(t,t_0) = \hat{T}\left(\mathrm{e}^{-\mathrm{i}\hbar^{-1}\int_{t_0}^{t}\mathrm{d}t'\,H_{\mathrm{S}}(t')}\right). \tag{3.43}$$

Transforming back to the Schrödinger picture using U_S and Eq. (3.3), gives

$$\partial_t\rho(t) = \partial_t\Big\{U_{\mathrm{S}}(t,t_0)\tilde{\rho}(t)U_{\mathrm{S}}^{\dagger}(t,t_0)\Big\} = -\frac{\mathrm{i}}{\hbar}\left[H_{\mathrm{S}},\rho(t)\right] + S(t), \tag{3.44}$$

where $S(t)$ defines the time-local scattering terms induced by the reservoir,

$$S(t) = U_{\mathrm{S}}(t,t_0)\left(\partial_t\{\tilde{\rho}(t)\}\right)U_{\mathrm{S}}^{\dagger}(t,t_0). \tag{3.45}$$

By exploiting the properties of U_S, we have the two relations

$$\begin{aligned} U_{\mathrm{S}}(t,t_0)\tilde{\rho}(t')U_{\mathrm{S}}^{\dagger}(t,t_0) &= U_{\mathrm{S}}(t,t_0)U_{\mathrm{S}}^{\dagger}(t',t_0)\rho(t')U_{\mathrm{S}}(t',t_0)U_{\mathrm{S}}^{\dagger}(t,t_0) &(3.46)\\ &= U_{\mathrm{S}}(t,t')\rho(t')U_{\mathrm{S}}^{\dagger}(t,t'), &(3.47)\end{aligned}$$

and similarly

$$U_{\mathrm{S}}(t,t_0)\tilde{P}_{\nu_1\nu_1'}(t')U_{\mathrm{S}}^{\dagger}(t,t_0) = U_{\mathrm{S}}(t,t')P_{\nu_1\nu_1'}U_{\mathrm{S}}^{\dagger}(t,t'). \tag{3.48}$$

Using these, the time-local scattering term may be achieved from Eq. (3.42) by substituting $\tilde{\rho}(t') \to \tilde{\rho}(t)$, before transforming back to the Schrödinger picture,

$$\begin{aligned} S(t) = -\frac{1}{\hbar^2}\int_{t_0}^{t}\mathrm{d}t' \sum_{\nu_1\nu_1'\nu_2\nu_2'}\Big\{ \\ \Big[P_{\nu_1\nu_1'}U_{\mathrm{S}}(t,t')P_{\nu_2\nu_2'}U_{\mathrm{S}}^{\dagger}(t,t')\rho(t) - U_{\mathrm{S}}(t,t')P_{\nu_2\nu_2'}U_{\mathrm{S}}^{\dagger}(t,t')\rho(t)P_{\nu_1\nu_1'}\Big]\langle\tilde{B}_{\nu_1\nu_1'}(t)\tilde{B}_{\nu_2\nu_2'}(t')\rangle \\ + \Big[\rho(t)U_{\mathrm{S}}(t,t')P_{\nu_2\nu_2'}U_{\mathrm{S}}^{\dagger}(t,t')P_{\nu_1\nu_1'} - P_{\nu_1\nu_1'}\rho(t)U_{\mathrm{S}}(t,t')P_{\nu_2\nu_2'}U_{\mathrm{S}}^{\dagger}(t,t')\Big]\langle\tilde{B}_{\nu_2\nu_2'}(t')\tilde{B}_{\nu_1\nu_1'}(t)\rangle\Big\}. \end{aligned} \tag{3.49}$$

3.3 Summary

In this chapter we have reviewed the basics of quantum dynamics. By applying a quantum master equation approach, we have derived an equation of motion for the reduced density matrix of a system, where the reservoir degrees of freedom have been traced out. In this way the equation of motion, Eq. (3.44), contains a term describing the pure system evolution, and a time-local scattering term in Eq. (3.49), where interaction with the reservoir enters.

Chapter 4

Model: Cavity QED system

The model considered in this thesis is a system consisting of a QD coupled to a cavity, interacting with the surroundings through various loss mechanisms, including interaction with a large phonon reservoir. In this chapter we apply the equation of motion derived in Chapter 3 to the many-body Hamiltonians stated in Chapter 2, and by doing this we treat only the electron-phonon interaction as a perturbation. This leads to a linear differential equation system for the elements of the reduced density matrix, which may be solved numerically by standard procedures. The derivation given here is a detailed description of the derivation given in [69].

In the rest of this thesis we refer to the two states of the two-level QD as either being an electron in the excited state or an electron in the ground state. In the electron-hole picture this is equal to having a single excitation of an electron-hole pair or no excitation, respectively.

4.1 Model description

In this work we consider a cavity-QD system interacting with a phonon bath, see Fig. 4.1. The total system may be described by the Hamiltonian

$$H = H_{\mathrm{s}} + H_{0,\mathrm{ph}} + H_{\text{e-ph}} + H_{\mathrm{loss}}, \tag{4.1}$$

where H_{s} represents the cavity-QD system, $H_{0,\mathrm{ph}}$ describes the part of the Hamiltonian representing the phonon bath, and $H_{\text{e-ph}}$ describes the interaction between the cavity-QD system and the phonons. The last term, H_{loss}, describe various interactions with the environment, represented by Lindblad terms and described by the population decay rates Γ, κ, and dephasing rate γ.

In this thesis we limit ourselves to only consider a single excitation of a two-level QD that may be in either the ground state $|g\rangle$ or the excited state $|e\rangle$. The energy of the electron is described by Eq. (2.31) and no electron-electron interaction is present. We consider coupling to a single cavity-mode, where the photons may be described by Eq. (2.34), neglecting the 1/2-term describing the vacuum field, which does not contribute to the dynamics. The electron-photon interaction is obtained from Eq. (2.42), where the standard rotating wave approximation have

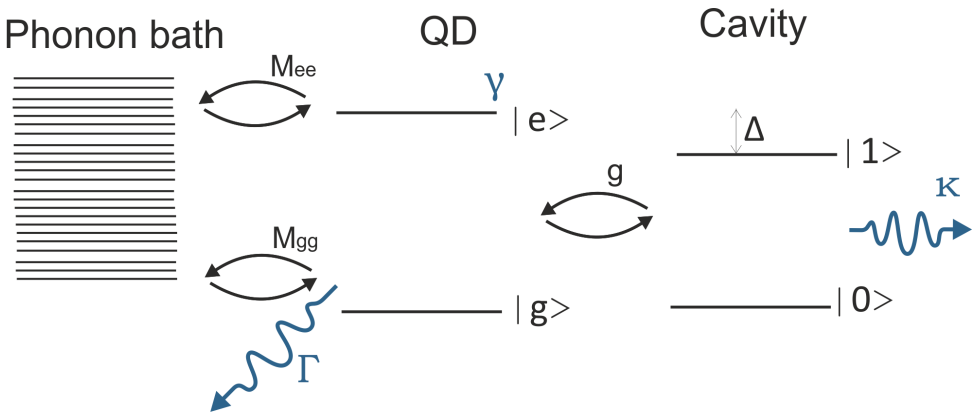

Figure 4.1: The considered cavity-QED system including interaction with a phonon bath and loss rates (blue symbols). An explanation of the different coupling rates and loss rates is given in the main text. The QD-cavity detuning, Δ, is positive when the transition frequency in the QD is larger than the frequency of the cavity mode.

been applied[1],

$$H_{\mathrm{s}} = \sum_{i=e,g} \hbar\omega_i c_i^\dagger c_i + \hbar\omega_{\mathrm{cav}} a^\dagger a + \hbar g \left(a^\dagger c_g^\dagger c_e + c_e^\dagger c_g a \right), \tag{4.2}$$

where the energy of the excited (ground) state is $\hbar\omega_e$ ($\hbar\omega_g$) and the energy of a cavity photon is $\hbar\omega_{\mathrm{cav}}$. The phonon bath is described by Eq. (2.35),

$$H_{0,\mathrm{ph}} = \sum_{j,\mathbf{k}} \hbar\omega_j(\mathbf{k}) b_{j,\mathbf{k}}^\dagger b_{j,\mathbf{k}}, \tag{4.3}$$

where the 1/2-term also is omitted. Finally, the interaction between the electrons and the phonons is expressed by Eq. (2.47)

$$H_{\text{e-ph}} = \sum_{j,\mathbf{k}} \left(M_{j,gg}^{\mathbf{k}} c_g^\dagger c_g + M_{j,ee}^{\mathbf{k}} c_e^\dagger c_e \right) \left(b_{j,-\mathbf{k}}^\dagger + b_{j,\mathbf{k}} \right). \tag{4.4}$$

Here, we set the matrix elements $M_{j,ge}^{\mathbf{k}}$ and $M_{j,ge}^{\mathbf{k}}$ to zero because the interlevel distance is much larger than the phonon energies considered in this thesis.

4.1.1 Electron-phonon interaction

In the derivations of the Hamiltonian we assumed bulk phonon mode, which was reasonable when the QD was small and the wetting layer thin. As discussed in [69], the LO phonons have energies, $\sim 37\,\mathrm{meV}$ in GaAs, which are much larger than the relevant phonon energies in this model, and we may neglect the Fröhlich coupling. According to the discussion in Section 2.3, the piezoelectric interaction may also be neglected when considering GaAs.

The only electron-phonon interaction that is included in the following calculations is thus the deformation potential interaction through LA-phonons, and the sum over the phonon branches

[1] In the rotating wave approximation, fast oscillating terms are ignored, because they will average out to a net contribution of zero as the time increases, see [75] for more details.

j in Eq. (4.4) is only over these LA-phonons. We express the interaction matrix elements in a notational slightly simpler way from now on,

$$M^{\mathbf{k}}_{\nu\nu} = D_\nu k \sqrt{\frac{\hbar}{2\rho V \omega_{\mathrm{LA}}(\mathbf{k})}} \mathcal{F}_\nu(\mathbf{k}), \quad \mathcal{F}_\nu(\mathbf{k}) = \int \mathrm{d}\mathbf{r}\, |\psi_\nu(\mathbf{r})|^2 \mathrm{e}^{\mathrm{i}\mathbf{k}\cdot\mathbf{r}}, \tag{4.5}$$

where $\nu = e$ describes an electron in the excited QD state and $\nu = g$ an electron in the ground state. For bulk phonons, $\omega_{\mathrm{LA}}(\mathbf{k}) = c_l|\mathbf{k}|$, with c_l being the longitudinal speed of sound.

The value of c_l and $D_{e/h}$ both posses a large uncertainty. The value of c_l varies depending on the propagation direction in the crystal, and may in GaAs vary from $4.8 - 5.4\,\mathrm{km/s}$. In the literature, many different values of $D_{e/g}$ appear, because the value of $D_{e/g}$ is difficult to estimate experimentally. We use same parameters as in other articles close to our subject, [43, 76, 66], and for an elaborating discussion of parameter values, see Appendix A.

4.1.2 Lindblad loss terms

Losses are included in a phenomenological way by including the possibility for the cavity-QD system to interact with other reservoirs than the phonon bath. We describe the losses by decay terms according to the the Lindblad formalism, which was introduced by Lindblad in 1976 [77] and is described in various articles and textbooks [68, 78, 70]. According to Lindblad, each loss mechanism γ_i contributes with a term

$$L\{O_i, \gamma_i\}\rho(t) = -\frac{\gamma_i}{2}\left[O^\dagger O\rho(t) + \rho(t)O^\dagger O - 2O\rho(t)O^\dagger\right], \tag{4.6}$$

that has to be added to the equation of motion for $\rho(t)$. The term $L\{O_i, \gamma_i\}$ describes the decay of the ith loss mechanism by the rate γ_i of the transition determined by the operator O_i. By including the loss mechanisms as decay rates, we implicitly assume that the interaction with the surroundings only is included as a mean, giving a Markovian description of the losses.

For the specific system, three loss mechanisms are considered: The first one described by the rate Γ is the population decay of the excited QD state due to spontaneous emission of photons into a large reservoir containing a continuum of non-radiant modes. The parameter κ describes the rate at which photons are lost in the cavity, e.g. due to a finite reflectivity of the cavity mirrors. The last rate γ concerns the pure dephasing of all transitions connected to the QD.

The LA phonons contribute to the pure dephasing rate [66], and we wish to describe this contribution separately, so this effect is not included into γ. Instead γ covers the pure dephasing that appears by including a finite lifetime of the phonons, e.g. from anharmonic effects [79, 65] or the optical transitions to higher energy levels of the QD assisted by phonons [80, 81].

4.2 Transforming the Hamiltonian

Because we are only considering a single electron in a two-level QD interacting with a single-mode cavity, it is convenient to consider a subspace of the full QD-cavity Hilbert space including only one electron or photon. The transformation of the Hamiltonian is goes as follows, where each part of the Hamiltonian Eq. (4.1) is treated separately.

Our model includes only a single electron in a two-level system, which results in the completeness relation

$$c_g^\dagger c_g + c_e^\dagger c_e = 1, \tag{4.7}$$

which is used to eliminate $c_g^\dagger c_g$ from Eq. (4.2) to give

$$H_s = \hbar\omega_g + \hbar\omega_{eg} c_e^\dagger c_e + \hbar\omega_{\text{cav}} a^\dagger a + \hbar g(a^\dagger c_g^\dagger c_e + c_e^\dagger c_g a), \tag{4.8}$$

where the transition frequency of the quantum dot is defined as $\omega_{eg} = \omega_e - \omega_g$. The first term $\hbar\omega_g$ is just a constant added to the total Hamiltonian and is neglected.

The electron-phonon interaction Hamiltonian Eq. (4.4) is also rewritten using Eq. (4.7),

$$H_{\text{e-ph}} = \sum_{\mathbf{k}} M^{\mathbf{k}} c_e^\dagger c_e \left(b_{-\mathbf{k}}^\dagger + b_{\mathbf{k}}\right) + \sum_{\mathbf{k}} M_{gg}^{\mathbf{k}} \left(b_{-\mathbf{k}}^\dagger + b_{\mathbf{k}}\right), \tag{4.9}$$

with $M^{\mathbf{k}} = M_{ee}^{\mathbf{k}} - M_{gg}^{\mathbf{k}}$.

The last term in Eq. (4.9) describes the phonon interaction with a fully occupied ground state of the electron. In thermal equilibrium the ground state of the whole system consists of an electron in the QD surrounded by a lattice deformation due to phonons. Because we want to describe deviations from this combined ground state, we take into account the phonon interaction with this new, combined ground state by shifting the phonon operators by [82, 69],

$$b_{\mathbf{k}} \to b_{\mathbf{k}} - \frac{M_{gg}^{-\mathbf{k}}}{\hbar\omega_{\mathbf{k}}}. \tag{4.10}$$

corresponding to a unitary transformation of the phonon operators. The Hamiltonians including phonon operators become

$$H_{0,\text{ph}} \to \sum_{\mathbf{k}} \hbar\omega_{\mathbf{k}} b_{\mathbf{k}}^\dagger b_{\mathbf{k}} - \sum_{\mathbf{k}} M_{gg}^{\mathbf{k}} \left(b_{\mathbf{k}} + b_{-\mathbf{k}}^\dagger\right) + \sum_{\mathbf{k}} \frac{1}{\hbar\omega_{\mathbf{k}}} M_{gg}^{\mathbf{k}} M_{gg}^{-\mathbf{k}}, \tag{4.11}$$

$$H_{\text{e-ph}} \to \sum_{\mathbf{k}} M^{\mathbf{k}} \left(b_{-\mathbf{k}}^\dagger + b_{\mathbf{k}}\right) c_e^\dagger c_e - 2\sum_{\mathbf{k}} \frac{1}{\hbar\omega_{\mathbf{k}}} M^{\mathbf{k}} M_{gg}^{-\mathbf{k}} c_e^\dagger c_e \tag{4.12}$$

$$+ \sum_{\mathbf{k}} M_{gg}^{\mathbf{k}} \left(b_{-\mathbf{k}}^\dagger + b_{\mathbf{k}}\right) - 2\sum_{\mathbf{k}} \frac{1}{\hbar\omega_{\mathbf{k}}} M_{gg}^{\mathbf{k}} M_{gg}^{-\mathbf{k}}, \tag{4.13}$$

where we in the calculation of $H_{0,\text{ph}}$ use that the sum is over all $\mathbf{k}$'s and we thus may substitute $\mathbf{k}$ with $-\mathbf{k}$ in the terms which are summed. Furthermore, we have assumed that the dispersion relation is symmetric in $\mathbf{k}$, i.e. $\omega_{\mathbf{k}} = \omega_{-\mathbf{k}}$ (due to the symmetry of the Brillouin zone in Fig. 2.1b), meaning that $\left(M_{gg}^{\mathbf{k}}\right)^* = M_{gg}^{-\mathbf{k}}$ according to the description of M_{gg} in Eq. (4.5).

Eq. (4.13) now contains non-interacting terms, but those are cancelled by terms in Eq. (4.11), meaning that the non-interacting phonon part, $H_{0,\text{ph}}$, may be considered unchanged after the transformation, and that

$$H_{\text{e-ph}} = \sum_{\mathbf{k}} M^{\mathbf{k}} c_e^\dagger c_e \left(b_{-\mathbf{k}}^\dagger + b_{\mathbf{k}}\right). \tag{4.14}$$

Here we removed the term $-2\sum_{\mathbf{k}} \frac{1}{\hbar\omega_{\mathbf{k}}} M^{\mathbf{k}} M_{gg}^{-\mathbf{k}} c_e^\dagger c_e$ by an energy renormalization by absorbing this term into the bare excited state energy $\hbar\omega_e$ [69], and we also omit the term $-\sum_{\mathbf{k}} \frac{1}{\hbar\omega_{\mathbf{k}}} M^{\mathbf{k}} M_{gg}^{-\mathbf{k}}$ because it is a constant term that do not contribute to the dynamics of the system as discussed in Section 3.1. This transformation does not have significant impact on H_{loss} [2].

[2] From discussions with Per Kær Nielsen

The subspace of the QD-cavity Hilbert space including one electron is spanned by the three basis states: $|1\rangle = |e, n = 0\rangle$, $|2\rangle = |g, n = 1\rangle$, and $|3\rangle = |g, n = 0\rangle$. The first index corresponds to the state of the electron in the QD, and the second index refers to the number of photons in the cavity.

The parts of H containing operators of the QD-cavity system can be expressed in this basis by calculating the matrix elements $\langle i|H|j\rangle$, $i, j = 1, 2, 3$, giving

$$H_s = \hbar\omega_{eg}\sigma_{11} + \hbar\omega_{\text{cav}}\sigma_{22} + \hbar g(\sigma_{12} + \sigma_{21}), \tag{4.15}$$

$$H_{\text{e-ph}} = B\sigma_{11}, \tag{4.16}$$

where $B = \sum_{\mathbf{k}} M^{\mathbf{k}}(b^\dagger_{-\mathbf{k}} + b_{\mathbf{k}})$ and $\sigma_{ij} = |i\rangle\langle j|$.

The system Hamiltonian may be further simplified by moving into a rotating frame determined by the unitary operator $T(t) = \exp(-\mathrm{i}\omega_{\text{cav}}[\sigma_{11} + \sigma_{22}]t)$ as described in details in Appendix B. By introducing the cavity-QD detuning $\Delta = \omega_{eg} - \omega_{\text{cav}}$, the system Hamiltonian is transformed into

$$H_s = \hbar\Delta\sigma_{11} + \hbar g(\sigma_{12} + \sigma_{21}). \tag{4.17}$$

Summarizing the derivations, we have obtained a final expression for the total Hamiltonian (excluding the loss terms),

$$H = H_s + H_{0,\text{ph}} + H_{\text{e-ph}} \tag{4.18}$$

$$= \hbar\Delta\sigma_{11} + \hbar g(\sigma_{12} + \sigma_{21}) + \sum_{\mathbf{k}} \hbar\omega_{\mathbf{k}} b^\dagger_{\mathbf{k}} b_{\mathbf{k}} + B\sigma_{11}. \tag{4.19}$$

with $B = \sum_{\mathbf{k}} M^{\mathbf{k}}(b^\dagger_{-\mathbf{k}} + b_{\mathbf{k}})$.

The explicit Lindblad terms

With the introduction of the QD-cavity subspace, we are able to identify the decay mechanisms with operators describing the relevant transitions. The decay of the population of the excited QD is described by $L\{\sigma_{31}, \Gamma\}$, the decay of the cavity population by $L\{\sigma_{32}, \kappa\}$, and the pure dephasing rate[3] $L\{\sigma_{11}, 2\gamma\}$.

4.3 Equation of motion for the system

The simple expression for the Hamiltonian in Eq. (4.19) may now be used in the calculation of the equations of motion derived in Chapter 3, where the phonon interaction appeared as a scattering term.

By comparing the interaction part in Eq. (4.19) with the general form of the electron-phonon interaction in Eq. (3.40), we see that $P_{\nu\nu'} = \sigma_{11}\delta_{1\nu}\delta_{1\nu'}$ and $B_{\nu\nu'} = B\delta_{1\nu}\delta_{1\nu'}$. Using this, the electron-phonon scattering term in Eq. (3.49) becomes

$$S_{\text{LA}}(t) = -\frac{1}{\hbar^2}\int_{t_0}^{t} \mathrm{d}t' \Big[\Big(\sigma_{11}U(t,t')\sigma_{11}U^\dagger(t,t')\rho(t) - U(t,t')\sigma_{11}U^\dagger(t,t')\rho(t)\sigma_{11}\Big) \langle \tilde{B}(t)\tilde{B}(t')\rangle + \Big(\rho(t)U(t,t')\sigma_{11}U^\dagger(t,t')\sigma_{11} - \sigma_{11}\rho(t)U(t,t')\sigma_{11}U^\dagger(t,t')\Big) \langle \tilde{B}(t')\tilde{B}(t)\rangle \Big], \tag{4.20}$$

[3] We use 2γ and not just γ for notational simplicity, such that the rate equations for the polarisations contain a term $\partial_t\langle\sigma_{12}(t)\rangle = \ldots - \gamma\langle\sigma_{12}(t)\rangle$ and not $\ldots - \frac{1}{2}\gamma\langle\sigma_{12}(t)\rangle$, as will be shown later on.

omitting to write the S-subscript on the Us indicating that the time evolution is determined by H_s.

From Eq. (3.7) we know that U depends only on the time difference, $U(t,t') = U(t-t')$. Thus, an integral on the following form, with f being a function that only depends on the time difference $t-t'$, may be rewritten

$$\begin{aligned}\int_{t_0}^{t} \mathrm{d}t'\, f(t-t')\langle\tilde{B}(t)\tilde{B}(t')\rangle &= \int_{0}^{t-t_0} \mathrm{d}t'\, f(t')\langle\tilde{B}(t)\tilde{B}(t-t')\rangle &(4.21)\\ &= \int_{0}^{t-t_0} \mathrm{d}t'\, f(t')\langle\tilde{B}(t')\tilde{B}(0)\rangle, &(4.22)\end{aligned}$$

where we in the last equality use the cyclic property of the trace. This leads as in [69] to the definition of the phonon bath correlation function

$$D^{\gtrless}(t-t') = \langle\tilde{B}(\pm[t-t'])\tilde{B}(0)\rangle, \tag{4.23}$$

noting that $[D^{>}(t)]^* = D^{<}(t)$ due to the swap of plus and minus in the time evolution. The final expression of the scattering term becomes

$$\begin{aligned}S_{\mathrm{LA}}(t) = -\frac{1}{\hbar^2}\int_0^t \mathrm{d}t' \Big[&\Big(\sigma_{11}U(t')\sigma_{11}U^\dagger(t')\rho(t) - U(t')\sigma_{11}U^\dagger(t')\rho(t)\sigma_{11}\Big) D^{>}(t') \\ &+ \Big(\rho(t)U(t')\sigma_{11}U^\dagger(t')\sigma_{11} - \sigma_{11}\rho(t)U(t')\sigma_{11}U^\dagger(t')\Big) D^{<}(t')\Big]\end{aligned} \tag{4.24}$$

where we for simplicity set $t_0 = 0$.

By including the loss terms discussed in Section 4.1.2, the equation of motion for the reduced density matrix operator in Eq. (3.44) becomes

$$\partial_t\rho(t) = -\mathrm{i}\hbar^{-1}\left[H_s, \rho(t)\right] + \left(L\{\sigma_{31},\Gamma\} + L\{\sigma_{32},\kappa\} + L\{\sigma_{11},2\gamma\}\right)\rho(t) + S_{\mathrm{LA}}(t). \tag{4.25}$$

Converting to a matrix problem

The equation of motion in Eq. (4.25) is linear in the reduced density matrix, making it preferable to describe the problem using linear algebra, where we follow the approach in [69]. Using the notation $\langle\sigma_{qp}\rangle = \mathrm{Tr}_s\{\rho(t)\sigma_{qp}\} = \rho_{pq}(t)$, where Tr_s indicates the trace with respect to the QD-cavity system, the reduced density matrix is mapped onto the vector

$$\langle\boldsymbol{\sigma}(t)\rangle = \Big[\langle\sigma_{11}(t)\rangle, \langle\sigma_{22}(t)\rangle, \langle\sigma_{12}(t)\rangle, \langle\sigma_{21}(t)\rangle, \langle\sigma_{23}(t)\rangle, \langle\sigma_{32}(t)\rangle, \langle\sigma_{13}(t)\rangle, \langle\sigma_{31}(t)\rangle\Big]^T. \tag{4.26}$$

We omit the population of the QD-cavity ground state $\langle\sigma_{33}(t)\rangle$ because it does not contribute to the dynamics, and it may be calculated through population conservation. As in [69], the coupling between the different matrix elements is split into three main contributions,

$$\partial_t\langle\boldsymbol{\sigma}(t)\rangle = \left[M_{\mathrm{coh}} + M_{\mathrm{Lindblad}} + M_{\mathrm{LA}}(t)\right]\langle\boldsymbol{\sigma}(t)\rangle = M(t)\langle\boldsymbol{\sigma}(t)\rangle. \tag{4.27}$$

Here, M_{coh} denotes terms stemming from the coherent evolution of the QD-cavity system, M_{Lindblad} the loss terms described in Section 4.1.2, and $M_{\mathrm{LA}}(t)$ is the scattering terms from

the electron coupling to phonons. In the following derivations we will simplify the notation by realizing that $M(t)$ may be divided into two submatrices,

$$M(t) = \begin{bmatrix} m^{(11)}(t) & 0 \\ 0 & m^{(22)}(t) \end{bmatrix}, \tag{4.28}$$

where $m^{(11)}(t)$ couples the first four elements of Eq. (4.26) and $m^{(22)}(t)$ couples the last four. An important point here is that due to the form of $M(t)$, there is no coupling between the two systems described by the two submatrices, and Eq. (4.27) may be solved independently for the two subsystems as 4×4 matrix problems.

Inserting the Hamiltonian

We now want to apply the matrix formulation to the Hamilton described in Eq. (4.19). With this Hamiltonian, the excited QD population is $\langle c_e^\dagger(t)c_e(t)\rangle = \langle\sigma_{11}(t)\rangle$ and the population of the cavity is $\langle a^\dagger(t)a(t)\rangle = \langle\sigma_{22}(t)\rangle$. The matrix elements of M_{coh} may be calculated for example as

$$\begin{aligned}
\langle\sigma_{12}(t)\rangle_{\text{coh}} &= \rho_{21,\text{coh}}(t) = -\mathrm{i}\hbar^{-1}\langle 2|[H_s, \rho(t)]|1\rangle && (4.29)\\
&= -\mathrm{i}\langle 2|\Big([\Delta|1\rangle\langle 1| + g\left(|1\rangle\langle 2| + |2\rangle\langle 1|\right), \rho(t)]\Big)|1\rangle && (4.30)\\
&= -\mathrm{i}\Big(g\rho_{11}(t) - \Delta\rho_{21}(t) - g\rho_{22}(t)\Big) && (4.31)\\
&= -\mathrm{i}g\langle\sigma_{11}(t)\rangle + \mathrm{i}g\langle\sigma_{22}(t)\rangle + \mathrm{i}\Delta\langle\sigma_{12}(t)\rangle && (4.32)
\end{aligned}$$

giving the third line in the first of the two submatrices

$$m_{\text{coh}}^{(11)} = \begin{bmatrix} 0 & 0 & -\mathrm{i}g & \mathrm{i}g \\ 0 & 0 & \mathrm{i}g & -\mathrm{i}g \\ -\mathrm{i}g & \mathrm{i}g & \mathrm{i}\Delta & 0 \\ \mathrm{i}g & -\mathrm{i}g & 0 & -\mathrm{i}\Delta \end{bmatrix}, \qquad m_{\text{coh}}^{(22)} = \begin{bmatrix} 0 & 0 & \mathrm{i}g & 0 \\ 0 & 0 & 0 & \mathrm{i}g \\ \mathrm{i}g & 0 & \mathrm{i}\Delta & 0 \\ 0 & -\mathrm{i}g & 0 & -\mathrm{i}\Delta \end{bmatrix}. \tag{4.33}$$

The Lindblad terms are calculated using Eq. (4.6) for the three loss terms $L\{\sigma_{31}, \Gamma\}$, $L\{\sigma_{32}, \kappa\}$, and $L\{\sigma_{11}, 2\gamma\}$. As an example we show the calculation of the matrix elements of $L\{\sigma_{31}, \Gamma\}$,

$$\begin{aligned}
\langle n|L\{\sigma_{31}, \Gamma\}\rho(t)|m\rangle &= -\frac{\Gamma}{2}\langle n|\left[\sigma_{31}^\dagger\sigma_{31}\rho(t) + \rho(t)\sigma_{31}^\dagger\sigma_{31} - 2\sigma_{31}\rho(t)\sigma_{31}^\dagger\right]|m\rangle && (4.34)\\
&= -\frac{\Gamma}{2}\left[\delta_{n1}\rho_{1m}(t) + \rho_{n1}(t)\delta_{1m} - 2\delta_{n3}\rho_{11}(t)\delta_{3m}\right]. && (4.35)
\end{aligned}$$

The total Lindblad matrix becomes a diagonal matrix,

$$\text{diag}\{M_{\text{Lindblad}}\} = -\frac{1}{2}[2\Gamma, 2\kappa, \Gamma + \kappa + 2\gamma, \Gamma + \kappa + 2\gamma, \kappa, \kappa, \Gamma + 2\gamma, \Gamma + 2\gamma]. \tag{4.36}$$

The scattering matrix is more complicated, and we provide an example on how to calculate some of the matrix elements. By calculating the element $\langle 1|S_{\text{LA}}(t)|1\rangle$, with S_{LA} given in Eq. (4.24), we find that $\langle 1|S_{\text{LA}}(t)|1\rangle = 0$ because the terms cancel each other. In the same way we find $\langle 2|S_{\text{LA}}(t)|2\rangle = 0$, but now all the terms are identically zero. Thus phonon scattering does not affect the population in the QD and the cavity directly. This is a consequence of our assumption

about neglecting the possibility of transitions in the QD only by emission/absorption of a phonon by letting $M_{eg}^{\mathbf{k}} = M_{ge}^{\mathbf{k}} = 0$ in Eq. (2.47), because the interlevel distance in our model is much larger than the phonon energies.

As an example, we calculate an element of M_{LA} from Eq. (4.24) using the completeness relation $\sum_n |n\rangle\langle n| = I$, where I is the identity operator,

$$\begin{aligned}\langle 2|S(t)|1\rangle &= -\frac{1}{\hbar^2}\int_0^t \mathrm{d}t' \,\langle 2|\Big[0 - U(t')\sigma_{11}U^\dagger(t')I\rho(t)\sigma_{11}D^>(t') \\ &\qquad +\rho(t)IU(t')\sigma_{11}U^\dagger(t')\sigma_{11}D^<(t') - 0\Big]|1\rangle \qquad (4.37)\\ &= -\frac{1}{\hbar^2}\int_0^t \mathrm{d}t' \Big[- U_{21}(t')\left(U_{11}^\dagger(t')\rho_{11}(t) + U_{12}^\dagger(t')\rho_{21}(t)\right)D^>(t') \\ &\qquad +\Big(\rho_{21}(t)U_{11}(t') + \rho_{22}(t)U_{21}(t')\Big)U_{11}^\dagger(t')D^<(t')\Big], \qquad (4.38)\end{aligned}$$

defining $U_{ij}(t) = \langle i|U(t)|j\rangle$ with the form of $U(t)$ as given in Eq. (3.7) describing the time evolution of the cavity-QD system,

$$U(t) = \mathrm{e}^{-\mathrm{i}\hbar^{-1}H_S t}. \qquad (4.39)$$

Physically $U(t)$ may be interpreted as an operator which introduces a photon-dressed QD into the phonon scattering terms. By defining also

$$\begin{aligned}\mathcal{G}^{\gtrless}(t) &= \mathrm{i}\hbar^{-2}\int_0^t \mathrm{d}t'\, U_{11}^*(t')U_{21}(t')D^{\gtrless}(t'), &(4.40)\\ \gamma_{12}(t) &= \hbar^{-2}\int_0^t \mathrm{d}t'\,\left[|U_{11}(t')|^2D^<(t') - |U_{21}(t')|^2D^>(t')\right], &(4.41)\\ \gamma_{13}(t) &= \hbar^{-2}\int_0^t \mathrm{d}t'\,|U_{11}(t')|^2D^<(t'), &(4.42)\\ \Delta_{\mathrm{pol}} &= \mathrm{Im}\{\gamma_{12}(\infty)\}, &(4.43)\\ \Delta'_{\mathrm{pol}} &= \mathrm{Im}\{\gamma_{13}(\infty)\}, &(4.44)\end{aligned}$$

we may write

$$\langle\sigma_{12}(t)\rangle_{\mathrm{scat}} = \langle 2|S(t)|1\rangle = -\mathrm{i}\mathcal{G}^>(t)\langle\sigma_{11}(t)\rangle + \mathrm{i}\mathcal{G}^<(t)\langle\sigma_{22}(t)\rangle - \gamma_{12}(t)\langle\sigma_{12}(t)\rangle, \qquad (4.45)$$

giving the third line in the first of the two submatrices that describe the scattering,

$$m_{\mathrm{LA}}^{(11)} = \begin{bmatrix} 0 & 0 & 0 & 0 \\ 0 & 0 & 0 & 0 \\ -\mathrm{i}\mathcal{G}^>(t) & \mathrm{i}\mathcal{G}^<(t) & -[\gamma_{12}(t) - \mathrm{i}\Delta_{\mathrm{pol}}] & 0 \\ \mathrm{i}[\mathcal{G}^>(t)]^* & -\mathrm{i}[\mathcal{G}^<(t)]^* & 0 & -[\gamma_{12}^*(t) + \mathrm{i}\Delta_{\mathrm{pol}}] \end{bmatrix}, \qquad (4.46)$$

and

$$m_{\mathrm{LA}}^{(22)} = \begin{bmatrix} 0 & 0 & 0 & 0 \\ 0 & 0 & 0 & 0 \\ \mathrm{i}\mathcal{G}^<(t) & 0 & -[\gamma_{13}(t) - \mathrm{i}\Delta'_{\mathrm{pol}}] & 0 \\ 0 & -\mathrm{i}[\mathcal{G}^<(t)]^* & 0 & -[\gamma_{13}^*(t) + \mathrm{i}\Delta'_{\mathrm{pol}}] \end{bmatrix}. \qquad (4.47)$$

To provide a physical interpretation of the effects of the electron-phonon scattering, we compare $m_{\mathrm{LA}}^{(11)}$ with $m_{\mathrm{coh}}^{(11)}$ in Eq. (4.33) and M_{Lindblad} in Eq. (4.36) as done also in [69]; similar arguments may be carried out for the elements of $m_{\mathrm{LA}}^{(22)}$.

The function $\gamma_{12}(t)$ appears as a diagonal element in $m_{\mathrm{LA}}^{(11)}$ and is multiplied by $\langle\sigma_{12}(t)\rangle$ as seen e.g. in Eq. (4.45). In this way $\mathrm{Re}\{\gamma_{12}(t)\}$ may be interpreted as a pure dephasing rate caused by the electron-phonon interaction, because $\gamma_{12}(t)$ only introduces a decay/gain in the polarisation and not in the populations. The imaginary part of $\gamma_{12}(t)$ introduces an energy shift, and to be consistent with the unitary transformation in Eq. (4.10), the long-time value of the energy shift, Δ_{pol}, has to be subtracted from $\gamma_{12}(t)$. This compensate for the energy shift which is introduced for the system ground state in the transformation when a combined electron-phonon ground state is considered. A similar discussion applies to $\gamma_{13}(t)$.

Furthermore the phonons introduce a cavity-QD coupling strength taking into account the electron-phonon interaction,

$$g \to g + \mathcal{G}^{\gtrless}(t), \tag{4.48}$$

where $>$ is for terms containing $\langle\sigma_{11}(t)\rangle$ and $<$ is for terms with $\langle\sigma_{22}(t)\rangle$. The real part of $\mathcal{G}^{\gtrless}(t)$ gives a renormalisation of g, but in general $\mathrm{Re}\{\mathcal{G}^{\gtrless}(t)\} \neq \mathrm{Re}\{\mathcal{G}^{<}(t)\}$, introducing an asymmetry in the polarisations $\langle\sigma_{12}(t)\rangle$ and $\langle\sigma_{21}(t)\rangle$. This will be studied in great details later on. Thus additional decoherence is obtained from $\mathrm{Im}\{\mathcal{G}^{\gtrless}(t)\}$ if $\langle\sigma_{11}(t)\rangle$ or $\langle\sigma_{22}(t)\rangle$ is non-zero.

The phonon bath correlation function

The phonons are described by the phonon bath correlation function,

$$D^{\gtrless}(t) = \langle\tilde{B}(\pm t)\tilde{B}(0)\rangle, \tag{4.49}$$

with $B = \sum_{\mathbf{k}} M^{\mathbf{k}}(b_{-\mathbf{k}}^{\dagger} + b_{\mathbf{k}})$ and by the Hamiltonian $H_{0,\mathrm{ph}} = \sum_{\mathbf{k}} \hbar\omega_{\mathbf{k}} b_{\mathbf{k}}^{\dagger} b_{\mathbf{k}}$. For such a time-independent Hamiltonian, the time evolution of $b^{\dagger}$ and b is trivial [46],

$$b_{\mathbf{k}}^{\dagger}(t) = \mathrm{e}^{\mathrm{i}\omega_{\mathbf{k}}t} b_{\mathbf{k}}^{\dagger}, \quad b_{\mathbf{k}}(t) = \mathrm{e}^{-\mathrm{i}\omega_{\mathbf{k}}t} b_{\mathbf{k}}. \tag{4.50}$$

In thermal equilibrium, we define the thermal occupation factor for the phonon mode with wavevector $\mathbf{k}$,

$$n_{\mathbf{k}} = \langle b_{\mathbf{k}}^{\dagger} b_{\mathbf{k}}\rangle = \frac{1}{\exp(\beta\hbar\omega_{\mathbf{k}}) - 1}, \tag{4.51}$$

with $\beta = 1/(k_B T)$. Using these expressions and standard bosonic commutation relations, and that $[M^{-\mathbf{k}}]^* = M^{\mathbf{k}}$, the correlation function may be written as

$$\begin{aligned} D^{\gtrless}(t) &= \sum_{\mathbf{k}} |M^{\mathbf{k}}|^2 \left[n_{\mathbf{k}} \mathrm{e}^{\pm\mathrm{i}\omega_{\mathbf{k}}t} + (n_{\mathbf{k}}+1)\mathrm{e}^{\mp\mathrm{i}\omega_{\mathbf{k}}t}\right] && (4.52)\\ &= \sum_{\mathbf{k}} |M^{\mathbf{k}}|^2 \left[(2n_{\mathbf{k}}+1)\cos(\omega_{\mathbf{k}}t) \mp \mathrm{i}\sin(\omega_{\mathbf{k}}t)\right]. && (4.53) \end{aligned}$$

The real part of $D^{\gtrless}(t)$ increases with temperature, whereas the imaginary part of $D^{\gtrless}$ is temperature independent.

4.4 Summary

In this chapter we inserted the many-body Hamiltonian derived in Chapter 2 into the equations of motion from Chapter 3 to arrive at a linear differential equation description in the reduced density matrix of the system with time-dependent coefficients as in Eq. (4.27), which we are able to solve numerically. Many different quantities and functions have been introduced in the model, and we will go through the description of these in details in the following chapter.

Chapter 5

Exploring the Model

In this chapter we explore the physics contained in our model step by step, starting from the lossless QD-cavity system in Section 5.1 and ending with the full model in Section 5.2, where phonon scattering from a non-Markovian phonon reservoir and the other loss mechanisms are included. On the way we verify the numerical implementation of the linear differential matrix equation from Chapter 4 by comparing to known results from the literature. In Section 5.3 we relate the features of this model to recent publications.

The parameters used in the simulation are described in details in Appendix A, if nothing else is stated.

5.1 Neglecting phonon scattering

The basics of the model described in Chapter 4 are first described without including the phonon scattering.

5.1.1 No loss, no phonon scattering

To get a basic understanding of the behaviour of the cavity-QD system, we first consider a lossless system without electron-phonon scattering, i.e. $M(t) = M_{\text{coh}}$ in Eq. (4.27), and we assume that the initial state of the system is $|1\rangle$, corresponding to an excited QD and no photons in the cavity. In this case the system is described by the (lossless) Jaynes-Cummings model[1], and the population of the QD evolves according to

$$\langle \sigma_{11}(t) \rangle = 1 - \frac{g^2}{g^2 + (\Delta/2)^2} \sin^2 \left(\sqrt{g^2 + (\Delta/2)^2} t \right), \tag{5.1}$$

which is derived in Appendix C. In Fig. 5.1a the simulation results are plotted, and these agree with Eq. (5.1). According to the Jaynes-Cummings model, the dynamics of the QD-cavity system is described by Rabi-oscillations, where the system evolves as a superposition of state $|1\rangle$, and state $|2\rangle$ (defined as a single photon in the cavity mode without excitations in the QD). Physically Fig. 5.1a should be interpreted as the probability of finding an excited QD when measuring on the system at a given time, meaning that for $\Delta = 0$ at $t = 10\,\text{ps}$, the probability of measuring an excited QD is $\approx 40\%$ and an excited cavity mode is $\approx 60\%$.

[1] This model is discussed in many textbooks, see e.g. [39].

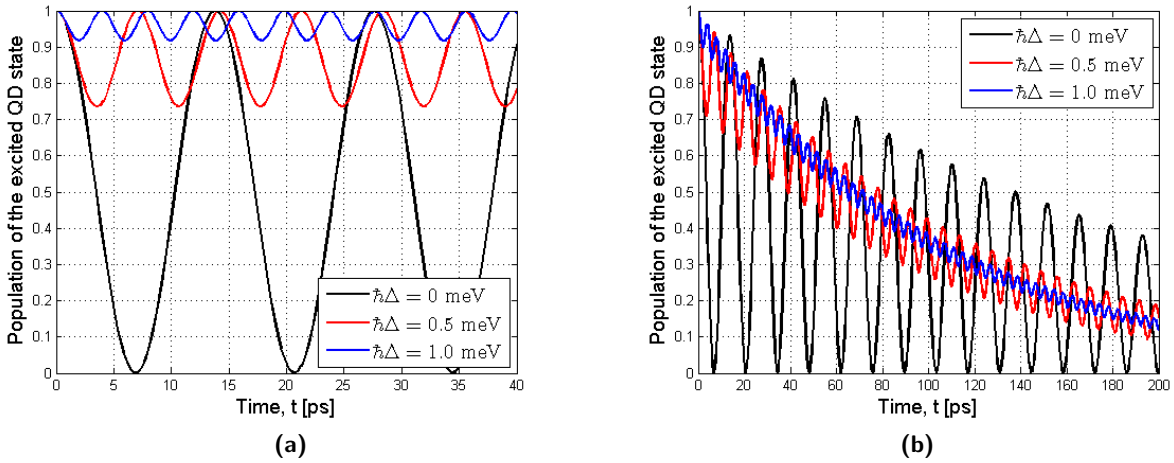

Figure 5.1: **(a)** Time-evolution of the population of the excited QD state, where loss and phonon-scattering is neglected; the different curves are for different detunings with $\hbar g = 150\,\mu$eV. The simulations agree with Eq. (5.1), and the results are the same if the sign of the detuning is changed. **(b)** Same as in (a), but where the loss term $\Gamma = 10\,\text{ns}^{-1}$ (corresponding to $7\,\mu$eV) is included.

At resonance, $\Delta = 0$, the system oscillates between a fully populated QD and a fully populated cavity, and the population transfer occurs with a period $\frac{2\pi}{2g}$, where the factor of 2 in front of g is due to the fact that $\sin^2(\cdot)$ oscillates with twice the frequency of $\sin(\cdot)$. Out of resonance, $\Delta \neq 0$, the coupling is not perfect, meaning that the excited state is never fully depleted, and the oscillation period is decreased. In the limit of infinite detuning or $g = 0$, $\langle\sigma_{11}(t)\rangle \approx 1$, no coupling will appear, and the system will remain in the excited QD state $|1\rangle$.

Physically this model states that when no losses are present, the spontaneous emission from the QD is a reversible process, where a photon is emitted into the cavity, then absorbed again in the QD, emitted, and so on. The dynamics in this model remains unchanged if the sign of the detuning is changed, which also may be realized from Eq. (5.1).

5.1.2 Loss included, no phonon scattering

When including the losses as discussed in Section 4.1.2, but still not phonon scattering, $M(t) = M_{\text{coh}} + M_{\text{Lindblad}}$, where $M(t)$ still is time-independent. Three different coupling terms are included: Γ and κ are the population decay rates from the excited QD state and the cavity mode respectively, and γ indicates the rate of pure dephasing for all transitions connected to the QD. We present a discussion of each of the loss effects separately, keeping the other two loss mechanisms turned off.

Having a non-zero Γ leads to decay of the system towards $|3\rangle$, where the QD is in the ground state and no photons in the cavity, see Fig. 5.1b. The oscillating behaviour is maintained throughout the decay, because all energy coupled to a cavity mode returns to the QD by virtue of the loss-free cavity. The value of Γ in Fig. 5.1b is choosen such that the dynamics of the three loss mechanisms may be considered on the same time scale for realistic values of κ and γ, see Appendix A for details on the parameter values. In practice $\Gamma \sim 1\,\text{ns}^{-1}$ [26], which gives a slower decay than illustrated in Fig. 5.1b.

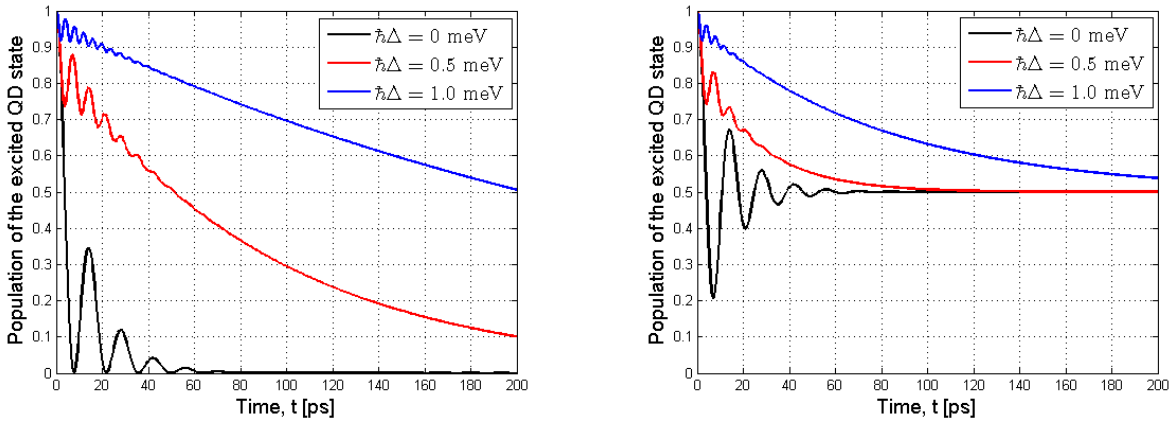

Figure 5.2: **(a)** Time evolution of population of excited QD state, plotted for different detunings with $\hbar\kappa = 100\,\mu$eV as the only loss mechanism. **(b)** The same simulation as in (a), but with $\hbar\gamma = 100\,\mu$eV as the only loss mechanism.

A non-zero κ also makes the system decay into $|3\rangle$ as shown in Fig. 5.2a. Now only the part of the excitation coupled to the cavity experiences loss, and thus the oscillating behaviour of the decay curve dies out, in contrast to the Γ-decay. As expected, the κ-decay is fastest for the smallest detunings where the coupling to the lossy cavity is largest.

At last, a non-zero γ introduces pure dephasing to all transitions connected to the QD. When no other losses are present, we may thus expect the coupling between the QD and the cavity to die out, and the better coupling between the cavity and the QD, the more the pure dephasing influences, giving the fastest population decays for the lowest detuning, see Fig. 5.2b. From the equation of motion for the polarization in Section 4.3,

$$\partial_t\langle\sigma_{12}(t)\rangle = -\mathrm{i}g(\langle\sigma_{11}(t)\rangle - \langle\sigma_{22}(t)\rangle) + (\mathrm{i}\Delta - \gamma)\langle\sigma_{12}(t)\rangle, \tag{5.2}$$

we see that in the long time limit, $(\langle\sigma_{11}(t)\rangle - \langle\sigma_{22}(t)\rangle) = 0$. Because the no population losses are included, we have from population conservation, $\langle\sigma_{11}(t)\rangle + \langle\sigma_{22}(t)\rangle = 1$, that the population of the excited state has to be $1/2$ in the long time limit, which we see in Fig. 5.2b.

It is important to note that in all cases the decay curves still look similar for simulations with detunings with the same magnitude but opposite sign. We use $\gamma = 0$ in the simulations in this thesis for simplicity, such that anharmonic effects are negelected and we only consider the pure dephasing induced by phonons.

Different coupling regimes

Depending on the magnitude of the loss terms compared to the coupling strength g, the cavity QD system evolves in qualitatively different ways or in different *regimes*.

The dynamics are described by the *lossy* or *dissipative* Jaynes-Cummings model. A basic description of this model is provided in [83, chap. 8] or [84, chap. 18], where $\gamma = 0$ is considered. Two regimes exist, the strong and the weak coupling regime. In the strong coupling regime, the coupling strength is much larger than the dissipative terms, i.e. the decoherence period is slow

compared to the period of the Rabi-oscillations ($= 2g$ for $\Delta = 0$), and the Rabi-oscillations will appear on the decay curves. In the weak coupling regime, the decoherence rate is much larger than the coupling strength. The decay curves decreases monotonically and the spontaneous emission of the photons is now an irreversible process. In the weak coupling regime, the presence of a cavity enhances the rate of spontaneous emission, where the enhancement is determined by the so-called Purcell factor, which will be described shortly.

When pure dephasing is included in the model, a lot of different definitions of regimes appear [85, 86]. Because γ decreases the polarisation $\langle\sigma_{12}(t)\rangle$ and $\langle\sigma_{21}(t)\rangle$ describing the transition between $|1\rangle$, $|2\rangle$, a new possibility appears, namely that a photon is emitted from the QD and stays in the cavity mode for some time *without* being absorbed back into the QD if κ is small. In the previous model the photon was re-absorbed in the strong coupling regime, and in the weak coupling regime the cavity acts like a loss source only.

To define relevant regimes for the model where γ is included, we and consider first the case where g is small compared to the decoherence rates and $g < \Delta$. In this case the terms $\langle\sigma_{12}(t)\rangle$ and $\langle\sigma_{21}(t)\rangle$ describing the transition may be adiabatically eliminated, see Appendix D.1, giving the two coupled equations,

$$\partial_t\langle\sigma_{11}(t)\rangle = -(\Gamma + R)\langle\sigma_{11}(t)\rangle + R\langle\sigma_{22}(t)\rangle, \tag{5.3}$$

$$\partial_t\langle\sigma_{22}(t)\rangle = -(\kappa + R)\langle\sigma_{22}(t)\rangle + R\langle\sigma_{11}(t)\rangle. \tag{5.4}$$

where

$$R = 2g^2\frac{\gamma_{\text{tot}}}{\gamma_{\text{tot}}^2 + \Delta^2}, \tag{5.5}$$

with the total dephasing rate being $\gamma_{\text{tot}} = (\Gamma + \kappa)/2 + \gamma$. In this way R appears as an effective coupling rate between the QD and the cavity.

Following [85] we may define two new coupling regimes, the good cavity regime and the bad cavity regime. The good cavity regime is achieved when $R > \kappa$, where the cavity damping time is longer than the QD-cavity coupling time. In this regime, the phonon emitted from the QD may stay in the cavity mode before it is re-absorbed in the QD or lost to the environment. The good-cavity regime becomes more demanding that the strong-coupling regime if γ becomes non-negligibel, see [85] for further details.

The bad cavity regime is characterized by $\kappa > R$, in which the cavity behaves like an extra loss channel, where the photon exits the cavity as soon as it is emitted from the QD. In this regime the QD-cavity transmission is incoherent, and R may be interpreted as an effective spontaneous emission rate. An important point here is that a system in the good cavity regime may turn into the bad cavity regime only by increasing the pure dephasing rate.

The Purcell regime described the dynamics of the system when $R \ll \kappa$, and in this case we may calculate the relaxation rate of the QD from Eqs. (5.3) and (5.4), see Appendix D.1. The rate is given by $\Gamma + R$, consisting with the fact that the cavity acts as an additional channel through which the QD can decay with the rate R. In this way we may define a generalized Purcell factor $F^* = R/\Gamma$, which described the enhancement of the spontaneous emission due to the cavity. Details about this generalized Purcell factor and an a detailed analysis of the different coupling regimes is provided in [85] and [86].

5.2 Including phonon scattering

We include the electron-phonon interaction by first assuming a memoryless phonon reservoir and afterwards consider the full, non-Markovian phonon reservoir.

The matrix element describing the LA-phonon-electron interaction is given in Eq. (4.5) and contains the wavefunction of an electron in the QD in the ground and excited state. We here assume that the wavefunction appearing in the form factor is spherically shaped and is the same for the excited and ground state (i.e. the electron and hole wavefunction are equal). This approximation is very crude and will be intensively discussed in Chapter 7, but is useful for the purpose of illustrating the behaviour of the system. The normalized wavefunction is

$$\phi_\nu(\mathbf{r}) = \frac{1}{\pi^{3/4}L^{3/2}}\mathrm{e}^{-r^2/(2L^2)}, \tag{5.6}$$

where L is a parameter describing the width of the wavefunction. We will refer to this as the crude wavefunction approximation.

5.2.1 Memoryless phonon reservoir

The interaction with the phonon bath is turned on at $t = 0$, but initially we assume that the phonon bath has no memory, i.e. that the phonon bath correlation function in Eq. (4.52) becomes proportional to a delta-function,

$$D^{\gtrless}(t) = \langle B^2\rangle\delta(t) = \sum_{\mathbf{k}} |M_{\mathbf{k}}|^2(2n_{\mathbf{k}}+1)\delta(t). \tag{5.7}$$

In this case the three functions $\mathcal{G}^{\gtrless}(t)$, $\gamma_{12}(t)$, and $\gamma_{13}(t)$ from Eq. (4.40)-(4.42) become,

$$\begin{aligned}
\mathcal{G}^{\gtrless}(t) &= \mathrm{i}\hbar^{-2}U_{11}^*(0)U_{21}(0)\langle B^2\rangle = 0, &(5.8)\\
\gamma_{12}(t) &= \hbar^{-2}\left[|U_{11}(0)|^2 - |U_{21}(0)|^2\right]\langle B^2\rangle = \hbar^{-2}\langle B^2\rangle, &(5.9)\\
\gamma_{13}(t) &= \hbar^{-2}|U_{11}(0)|^2\langle B^2\rangle = \hbar^{-2}\langle B^2\rangle, &(5.10)
\end{aligned}$$

using that the time evolution operator $U(t)$ given in Eq. (4.39) is equal to the identity operator for $t = 0$. When the cavity-QD system interacts with a memoryless phonon reservoir, the only contribution of the phonons is a pure dephasing rate of the polarisations concerning the transition between $|1\rangle$ and $|2\rangle$ and also between $|1\rangle$ and $|3\rangle$, which is realized by considering the expressions for $m_{\mathrm{LA}}^{(11)}$ and $m_{\mathrm{LA}}^{(22)}$ in Eqs. (4.46) and (4.47). In this case $\gamma_{12} = \gamma_{13}$ are constant in time, and both are real and positive, meaning that the electron-phonon coupling always enlarges the decay rate, and they increase with increasing temperature.

In Figs. 5.3a and 5.3b the decay curves from a simulation including a memoryless phonon reservoir is without, where only the loss mechanisms described by Γ, κ, and γ are present. As expected from the discussion on the loss mechanisms, the fastest decay appears when the detuning between the cavity and the QD is smallest, where the system is influenced by both the loss in the QD and in the cavity. From Eq. (5.5) the system is in the strong coupling regime when $|\Delta| < \gamma_{\mathrm{tot}}\sqrt{2g^2/(\kappa\gamma_{\mathrm{tot}}) - 1} = 0.1\,\mathrm{meV}$ using the described parameters. Thus the oscillations seen for $\Delta = 0$ is due to coherent transfer of energy between the QD and the cavity. Oscillations also appear for higher values of Δ for small times, although the system is in the weak coupling regime. This is due to non-Markovian behaviour of the QD-cavity coupling, which explains why the amplitude if the oscillations becomes small for large detunings.

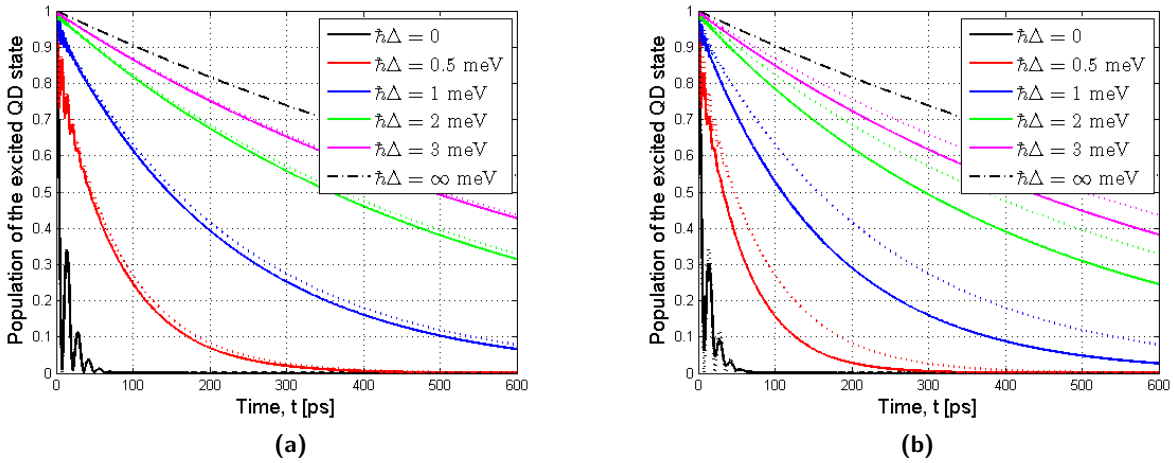

Figure 5.3: **(a)** Population of the excited QD state as a function of time for different detunings. The solid lines describes a simulation including a memoryless phonon reservoir, and the dotted lines are the results of a simulation without the reservoir where only loss mechanisms are enabled. Here we use $L = 5$ nm, $\hbar g = 150\,\mu$eV, $\Gamma = 1\,$ns, $\hbar\kappa = 100\,\mu$eV and $\hbar\gamma = 0$. The temperature is $T = 0\,$K. **(b)** The same as in Fig. 5.4a, but at $T = 40\,$K.

In Figs. 5.3a and 5.3b we observe that at a temperature of $T = 0\,$K, the decay rates are increased slightly compared to the simulation where the phonon reservoir not is include. At $T = 40\,$K the difference in decay rates is larger, as expected from Eq. (5.9), because the phonon-induced pure dephasing rate is increased. The black dash-dot line indicates the slowest decay possible, which appears when the cavity and QD are strongly detuned such that no coupling to the cavity is present, and the decay rate is given by Γ.

The effect of the phonon bath is largest at mid-range detunings, $\Delta = 1 - 2\,$meV, which is a feature of $M^{\mathbf{k}}$ which we go into further details with later on.

5.2.2 A phonon reservoir with memory

Now we apply the full phonon model as described in Section 4.3, where the phonon bath is assumed to have memory described by the phonon bath correlation function $D^{\gtrless}(t)$ given in Eq. (4.52). In this case $\mathcal{G}^{\gtrless}(t) \neq 0$, and $\gamma_{12}(t)$ and $\gamma_{13}(t)$ are no longer constants.

The decay curves are plotted in Figs. 5.4a and 5.4b for $T = 0\,$K and $T = 40\,$K. A significant effect appears here compared to the previously shown decay curves, namely that the decay curves are no longer similar if the sign of the detuning is flipped. Mathematically $\gamma_{12}(t)$ and $\gamma_{13}(t)$ remains symmetric in Δ, but the now non-zero $\mathcal{G}^{\gtrless}(t)$ is not symmetric in Δ and thus introduces an anharmonicity in the system.

Physically we may understand it in the way, that in a case with $\Delta < 0$ the transition energy of the QD is smaller than the energy of the cavity photons, and for $T = 0\,$K no excited phonons are present meaning that no phonon-assisted coupling between the QD and cavity may occur. For $\Delta > 0$ the QD may emit a phonon and couple to the cavity, giving a faster decay than the case with negative detuning, which is also seen in Fig. 5.4a. When increasing the temperature as in Fig. 5.4b, this asymmetry due to the phonons is less pronounced due to the thermal excitation

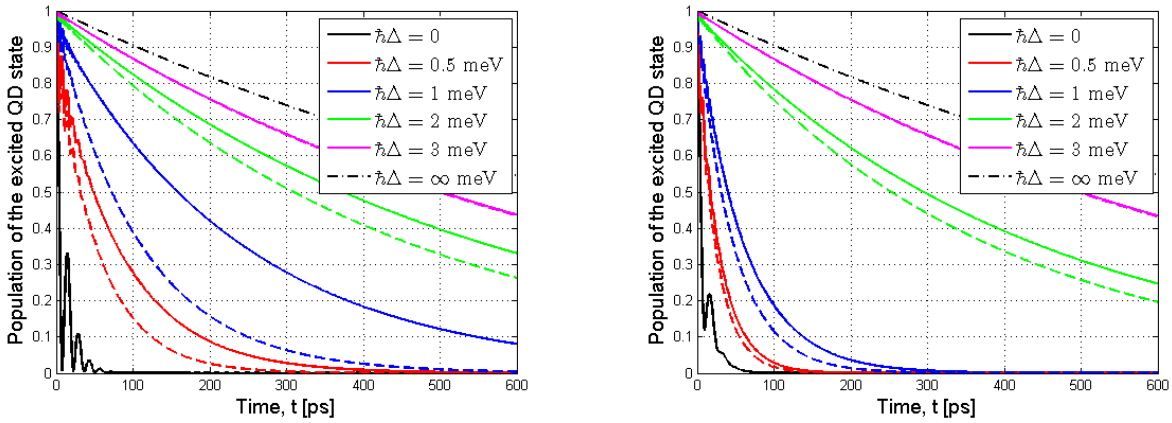

Figure 5.4: **(a)** Population of the excited QD state as a function vs. time, including loss and phonon scattering. The solid (dashed) curve is for negative (positive) detuning with the parameters $L = 5$ nm, $\hbar g = 150\,\mu$eV, $\Gamma = 1$ ns, $\hbar\kappa = 100\,\mu$eV and $\hbar\gamma = 0$. The temperature is $T = 0$ K, and for clarity the two purple lines describing ± 3 meV are almost coinciding. **(b)** The same as in Fig. 5.4a, but at $T = 40$ K. In this case the anharmony of the decay curves due to the phonons becomes smaller.

of phonons, making the probability of emitting a phonon almost the same as absorbing a phonon (these probabilities are equal at $T \to \infty$). Due to the increased probabilities, the decays happen faster than at $T = 0$ K.

An important aspect of this model is discussed in [1] and is worth mentioning here. If we set $g = 0$ in $U(t)$ only, the anharmonicity in the decay curves in Figs. 5.4a and 5.4b is lost, and the decay is described by the solid curves, i.e. for $\Delta < 0$. Remembering that $U(t)$ is the operator which introduces a photon-dressed QD into the phonon scattering terms, setting $g = 0$ may be interpreted as letting the phonon interact with the bare electron only and not the electron-photon quasiparticle, called the polariton, which actually appears in the cavity-QD system. In conclusion it is stressed out in [1], that it is important to take the nature of the polaronic quasiparticle in strongly coupled cavity-QD systems into account when describing the interaction with a non-Markovian phonon reservoir. Another effect of the phonon-induced pure dephasing is, consistent with the good/bad coupling discussion in Section 5.1.2, that the limits for strong and weak QD-cavity coupling is shifted, see [1] for further details.

As we see in Figs. 5.4a and 5.4b, the phonon anharmonicity is also largest for middle-valued detunings. This is discussed in the following, where we to get a more detailed picture on the electron-phonon scattering study the phonon bath correlation function in details.

5.2.3 The phonon reservoir correlation function

As we saw in the discussion above, all information about the phonons are contained in the phonon correlation function $D^{\gtrless}(t)$, so it is worth spending a little time considering this.

We recall from Section 4.3 the expression for the phonon bath correlation function,

$$D^{\gtrless}(t) = \sum_{\mathbf{k}} |M^{\mathbf{k}}|^2 \left[n_{\mathbf{k}} \mathrm{e}^{\pm \mathrm{i}\omega_{\mathbf{k}} t} + (n_{\mathbf{k}} + 1)\mathrm{e}^{\mp \mathrm{i}\omega_{\mathbf{k}} t} \right]. \tag{5.11}$$

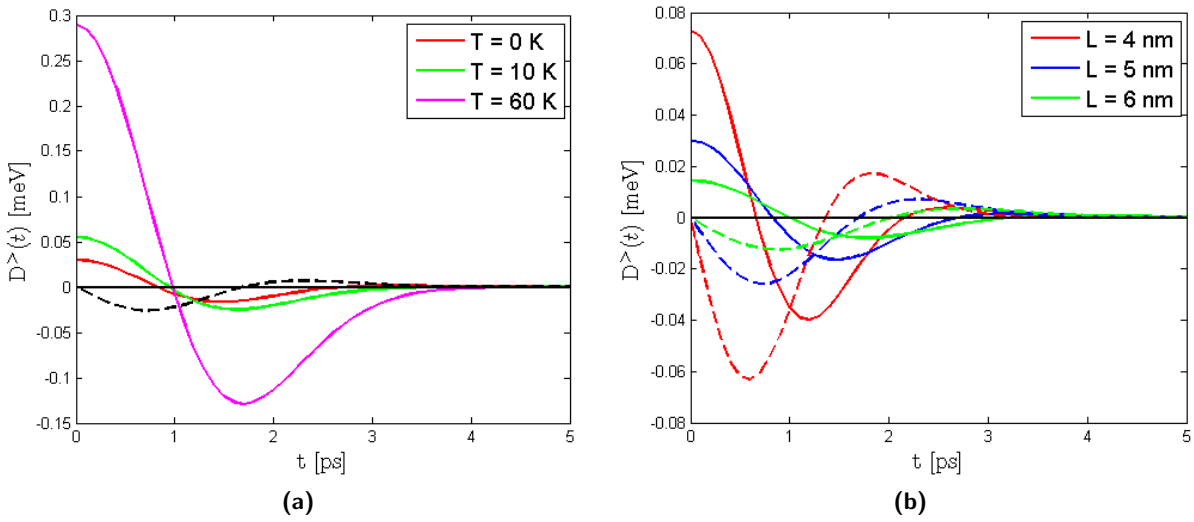

Figure 5.5: **(a)** The phonon reservoir correlation function versus time for different temperatures. The solid (dotted) lines are the real (imaginary) part of the correlation function. **(b)** The phonon correlation function versus time for different value of L.

with $M^{\mathbf{k}} = M^{\mathbf{k}}_{ee} - M^{\mathbf{k}}_{gg}$, where $M^{\mathbf{k}}_{ee}$ and $M^{\mathbf{k}}_{gg}$ are the electron-phonon interaction matrix elements of an electron in the excited and ground state of QD, respectively. For bulk phonons with the linear dispersion relation $\omega_{\mathbf{k}} = c_l|\mathbf{k}| = c_l k$, the matrix elements are calculated from Eq. (4.5),

$$M^{\mathbf{k}}_{ee/gg} = D_{e/h}\sqrt{\frac{\hbar k}{2\rho V c_l}}\int \mathrm{d}\mathbf{r}\,|\phi_{e/h}(\mathbf{r})|^2 \mathrm{e}^{\mathrm{i}\mathbf{k}\cdot\mathbf{r}}. \tag{5.12}$$

The sum over $\mathbf{k}$ in Eq. (5.11) may be transformed into an integral, assuming that the quantuzation volume is large,

$$\sum_{\mathbf{k}} = \frac{V}{(2\pi)^3}\int \mathrm{d}\mathbf{k}\,. \tag{5.13}$$

The phonon correlation is plotted for different temperatures and values of L in Figs. 5.5a and 5.5b. The correlation function is non-zero only for $t < 5\,\mathrm{ps}$, meaning that $\mathcal{G}^{\gtrless}(t)$, $\gamma_{12}(t)$ and $\gamma_{13}(t)$ attains constant for after 5 ps. The amplitude of $D^{\gtrless}(t)$ increases when increasing the temperature due to thermal excitation of more phonons. A small width of the wavefunction also increase $D^{\gtrless}(t)$, and this may be explained from the interaction matrix element in Eq. (5.12) which contains the Fourier transform of the electron wavefunction. A small wavefunction gives a wider function in momentum space, allowing the electrons to interact with more phonon modes.

Rather than considering the correlation function in the time domain, it may be more insightful to determine how the effect of the electron-phonon coupling appears in the frequency domain[2]. The real part of the phonon correlation function, Eq. (5.11), in the frequency domain

[2]In some articles, the electron-phonon interaction is described by a spectral density $J(\omega)$ instead of a correlation function, as we do here [87]. The spectral density is given by $J(\omega) = \sum_{\mathbf{k}} |M^{\mathbf{k}}|^2\delta(\omega - \omega_{\mathbf{k}})$ and is related to $D^{\gtrless}(t)$ in the way that at $T = 0\,\mathrm{K}$, $D^{\gtrless}(t) = \int_0^\infty \mathrm{d}\omega\, J(\omega)$ and thus $J(\omega)$ describe the phonon distribution in energy.

is,

$$\mathrm{Re}\{D^{>}(\omega)\} = \pi \sum_{\mathbf{k}} |M^{\mathbf{k}}|^2 \left[n_{\mathbf{k}} \delta(\omega + \omega_{\mathbf{k}}) + [n_{\mathbf{k}} + 1] \delta(\omega - \omega_{\mathbf{k}}) \right], \tag{5.14}$$

where the Fourier transform is defined as

$$f(\omega) = \int_0^\infty \mathrm{d}t \, \mathrm{e}^{\mathrm{i}(\omega + \mathrm{i}0^+)t} f(t), \tag{5.15}$$

with 0^+ being a positive infinitesimal number that is included to ensure convergence of the integral. Here we use the well-known relation to evaluate integrals on the form $\int_{-\infty}^{\infty} \mathrm{d}\omega \, \frac{1}{\omega + \mathrm{i}0^+} f(\omega)$ for well-behaved function $f(\omega)$,

$$\frac{1}{\omega + \mathrm{i}0^+} = \mathcal{P}\frac{1}{\omega} - \mathrm{i}\pi\delta(\omega), \tag{5.16}$$

where $\mathcal{P}$ indicates the Cauchy principle part. As mentioned in [69], Eq. (5.14) contains information about the electron-phonon interaction and may be considered as en effective phonon density, which is described in units of $\mathrm{meV}^2\,\mathrm{ps}$.

A way to physically understand $\mathrm{Re}\{D^{<}(\omega)\}$ is discussed in [69]. In the limit $g \ll \Delta$, the involved polarizations may be adiabatically eliminated, and $U(t)$ may be expanded in g/Δ to low order, in which case the total decay rate including phonon scattering may be expressed as

$$\Gamma_{\mathrm{tot}} \approx \Gamma + 2g^2 \frac{\gamma_{\mathrm{tot}}}{\gamma_{\mathrm{tot}}^2 + \Delta^2} \left[1 + \frac{1}{\hbar^2 \gamma_{\mathrm{tot}}} \mathrm{Re}\{D^{>}(\omega = \Delta)\} \right], \tag{5.17}$$

where the total dephasing rate is given as $\gamma_{\mathrm{tot}} = \gamma + (\Gamma + \kappa)/2$. A proof of this expression is however not given in [69], and therefore we present a thorough exposition of the derivation in Appendix D.

The term "1" in the brackets in Eq. (5.17) expresses the loss from the direct decay of the QD through interaction with the cavity through the Purcell-effect as described in Section 5.1.2. This term modifies the decay in the same way for positive as for negative detunings, giving symmetric decay curves. The second term contains the electron-phonon interaction through $\mathrm{Re}\{D^{>}(\omega)\}$ if it is non-zero when evaluated at $\omega = \Delta$.

With the crude wavefunction assumption in Eq. (5.6), the interaction matrix element becomes

$$M_{\nu\nu}^{\mathbf{k}} = \sqrt{\frac{\hbar k}{2 d c_l V}} D_\nu \mathrm{e}^{-k^2 L^2/4}, \tag{5.18}$$

and Eq. (5.14) reduces to

$$\mathrm{Re}\{D^{>}(\omega)\} = \frac{\hbar}{4\pi d c_l^5} \cdot \frac{\omega^3}{1 - \mathrm{e}^{-\beta\hbar\omega}} \cdot (D_e - D_g)^2 \mathrm{e}^{-\omega^2 L^2/(2c_l^2)}. \tag{5.19}$$

where ω is the phonon frequency. The expression is written in this way to point out that $\mathrm{Re}\{D^{>}(\omega)\}$ is a product of three terms: A constant term depending on the macroscopic properties of the material, a term depending entirely on the temperature, and at last a temperature independent integral depending on the material constants and the properties of the QD.

By introducing a "cut-off"-frequency $\omega_c = \sqrt{2} c_l / L$, Eq. (5.19) for $T = 0\,\mathrm{K}$ may be written as

$$\mathrm{Re}\{D^{>}(\omega)\} = \alpha \frac{\omega^3}{\omega_c^3} \mathrm{e}^{-\omega^2/\omega_c^2}, \tag{5.20}$$

where $\alpha = \hbar(D_e - D_g)^2/(\sqrt{2}\pi^2\rho c_l^2 L^3)$, which is an amplitude parameter describing the electron-phonon interaction strength. For the used parameters and $L = 5\,\text{nm}$, we get $\alpha = 0.26$, but what is more important is that $\alpha \propto L^{-3}$, which shows a significant dependence on the width of the carrier wavefunction. L though appears in ω_c, so the rest of the expression in Eq. (5.20) increases when L is increased. A plot of Eq. (5.20) is given in Fig. 5.6, from which we see that the electron-phonon interaction only is significant for $\omega \lesssim 3\omega_c$. As $\omega_c \propto L^{-1}$, we see that for the crude wavefunctions the energy span, over which electron-phonon coupling influences, decreases when the width of the QD wavefunction increases, corresponding to interaction with fewer phonon modes.

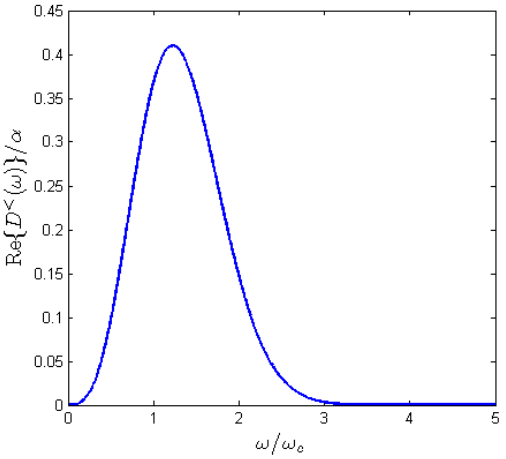

Figure 5.6: The normalized efective phonon spectrum vs. normalized frequency, $T = 0\,\text{K}$.

Eq. (5.20) gives a basic understanding of the phonon influence, although it does not include temperature dependence. $\text{Re}\{D^>(0)\} = 0$ due to intrinsic properties of the interaction matrix element because $\omega = 0$ corresponds to the infinite-wavelength of the phonons, which is a

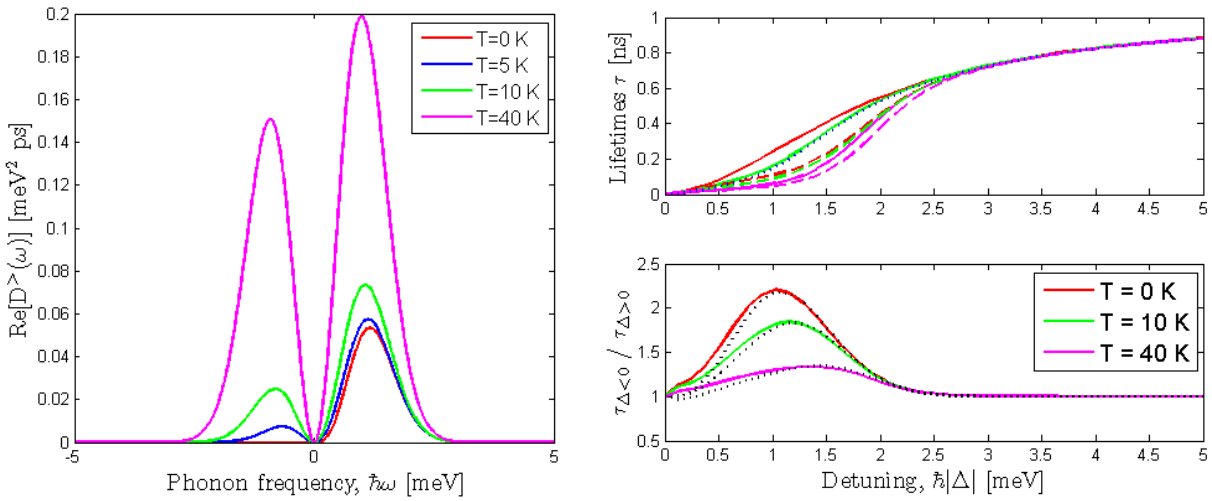

(a) **(b)**

Figure 5.7: **(a)** Effective phonon spectrum versus phonon frequency plotted for different temperatures under the assumption of a crude wavefunction, plotted from Eq. (5.19). For $T = 0$ the spectrum is zero for negative detuning as expected since no excited phonons are present for the QD to absorb. Simulation parameters are described in Appendix A and $L = 5\,\text{nm}$. **(b)** Top figure: Lifetimes of the excited QD state plotted versus the detuning for different temperatures. The solid (dashed) curves is for negative (positive) detunings. The black dotted line is the approximate solution from Eq. (5.17) for $T = 10\,\text{K}$ and negative detuning. Bottom figure: The degree of asymmetry defined as the ratio of the lifetime for opposite signs of the detuning. The black dotted lines indicates the values obtained with the approximate expression for Γ_{tot} at the specific temperature in Eq. (5.17).

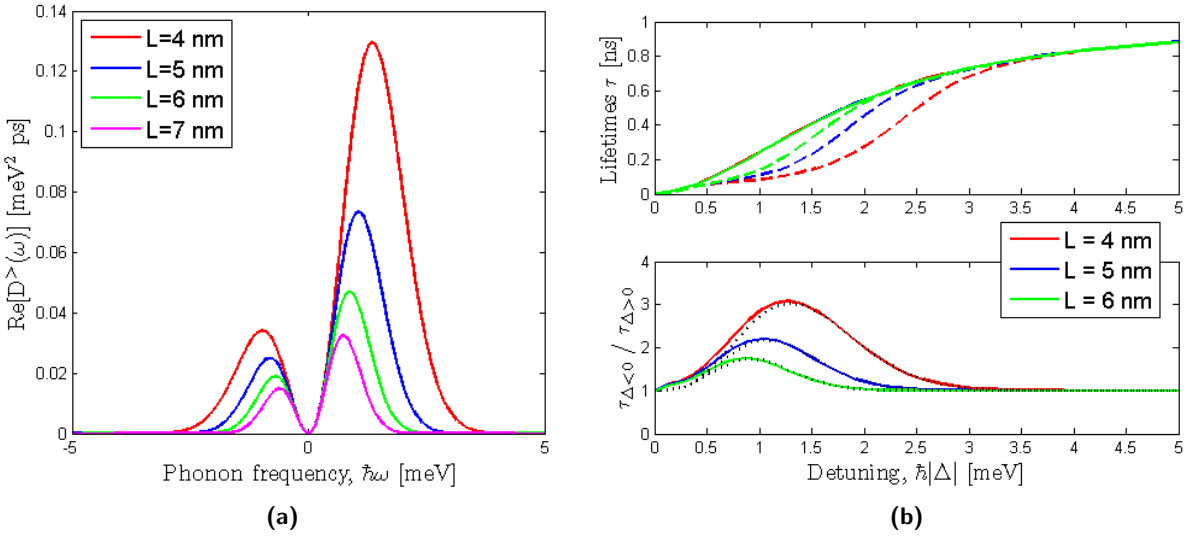

Figure 5.8: **(a)** Effective phonon spectrum versus phonon frequency plotted for different wavefunction widths under the assumption of a crude wavefunction, plotted from Eq. (5.19). Simulation parameters are described in Appendix A and $T = 10\,\mathrm{K}$. **(b)** Top figure: Lifetimes of the excited QD state plotted versus the detuning for different wavefunction widths calculated for $T = 0\,\mathrm{K}$. The solid (dashed) curves is for negative (positive) detunings. The curves for negative detunings are coinciding because at $T = 0\,\mathrm{K}$ no thermally excited phonons contribute exists, no matter the value of L. Bottom figure: The degree of asymmetry defined as the ratio of the lifetime for opposite signs of the detuning. The black dotted lines indicates the values obtained with the approximate expression for Γ_{tot}, Eq. (5.17).

translation of the whole crystal and thus not introduce any electron-phonon interaction.

Eq. (5.19) indicates how $\mathrm{Re}\{D^{>}(\omega)\}$ scales with temperature, and we plot it for different temperatures, see Fig. 5.7a. Note that for $T = 0$ K, $\mathrm{Re}\{D^{>}(\omega)\} = 0$ for $\omega < 0$. Physically this makes sense as discussed earlier, because when $\Delta < 0$ the QD must absorb a phonon to match the cavity mode, but there are no excited phonons to absorb when $T = 0$ K. For high temperatures, the possibility of emitting and absorbing a phonon is almost equal and we expect a symmetric spectrum as also indicated by Fig. 5.7a. This figure illustrates, as pointed out in Section 5.2, that the phonon interaction is largest for detunings around $1 - 2\,\mathrm{meV}$.

In an experiment, the effective phonon spectrum would be difficult to extract. What usually is measured is decay curves of the excited QD state, and from these curves the lifetime of the excited QD state can be determined. To make our model comparable with physical results we extract the lifetime from our calculations by making a single-exponential fit to the calculated decay curves as the one in Fig. 5.4a. The oscillating behaviour of the decay curve for small times makes it difficult to extract precise lifetimes for small Δ, introducing a small uncertainty here. The lifetime for varying detuning is shown in Fig. 5.7b for different temperatures. Agreeing with the asymmetry discussion above, the asymmetry is largest when T is low with fewest thermally excited phonons, and in the limit of infinite detuning, no coupling exists between the cavity and the QD, giving a lifetime of the excited QD state of $1/\Gamma = 1\,\mathrm{ns}$. Varying the temperature does not change the detuning range, at which the asymmetry is seen, because the electron-phonon matrix element, $M^{\mathbf{k}}$, is temperature independent.

Furthermore we see, that the approximate expression for the total decay rate in Eq. (5.17)

quite well describes the asymmetry for large detunings, but deviates for low detuning. Eq. (5.17) was however derived in the limit $\Delta \gg g = 150\,\mu\text{eV}$, so it is not valid for low detuning.

Another parameter that may be varied it the coupling strength, g. We do not make a specific plot of the lifetimes but refer to a plot in [69], which shows that the lifetime decreases as g increases, consistent with the Purcell effect. The asymmetry between lifetimes for positive and negative detuning is increased when g is increased, which is expected since the QD decays *through* the cavity by emission of a phonon. Thus when the QD-cavity coupling is increased, we expect a faster decay and thereby shorter lifetime for $\Delta > 0$ but not for $\Delta < 0$.

Quantum dots may have many different sizes. Thus we vary the width of the QD wavefunction, L, to determine how the effective phonon spectrum changes, see Fig. 5.8a. As discussed below Eq. (5.20), both the amplitude and the energy span of the electron-phonon interaction increases when L decreases. This applies also to the lifetimes of the excited QD state, see Fig. 5.8b, where the plot of the relative lifetimes "adapts" the shape of the effective phonon spectrum for $\Delta \gg g$, such that a higher lifetime asymmetry is achieved for lower wavefunction widths.

5.3 Relating the model to present research

Having realized some the physical properties of the considered model, it would be worth relating the model to the recent developments in the research field.

A standard way of describing the impact of electron-phonon interaction on dephasing in a QD-cavity system is by including the effect of phonons by a pure dephasing rate only [86, 88, 85]. This corresponds to a memoryless phonon reservoir, the so-called Markovian description, and this model has been shown to be inadequate in describing the decoherence due to the electron-phonon interaction [1].

Our model in this thesis goes beyond the Markovian dynamics by introducing a phonon reservoir that do have memory, described by a correlation function. Several recent publications consider decoherence of the polarisation in a bare QD due to electron-phonon interaction in a QD excited by a classical laser pulse, and they demonstrate that the phonons have a big influence on the coherent optical response [89, 76, 66]. Several ways are proposed to reduce the decoherence, e.g. by controlling the excitation pulses [90].

Several articles discuss a non-Markovian phonon bath interacting with a QD inside an optical cavity [1, 91, 92, 43, 93]. In these the asymmetry due to phonon-assisted cavity-feeding is discussed, which is present for $\Delta > 0$ but not for $\Delta < 0$, and the possibility of phonon-assisted electron-cavity coupling have also been addressed experimentally in a photonic crystal cavity [94].

5.4 Summary

In steps we have described the physics contained in our coupled QD-cavity model interacting with a non-Markovian phonon reservoir. For a memoryless reservoir, the phonons only contribute by a pure dephasing rate, but in the full non-Markovian description, the phonons induce an asymmetry in the lifetime when changing the sign of the detuning. With a crude approximation for the electron wavefunction, we observed that the influence of the electron-phonon interaction becomes larger when 1) the temperature is increased due to more thermally excited phonons, 2) the QD-cavity coupling strength is increased, such that more energy is transferred between the QD and the cavity, which thus to a higher degree is affected by pure dephasing, and 3) the electron wavefunction width is decreased, due to interaction with more phonon modes.

We have demonstrated that the memoryless description of the phonon reservoir is insufficient in describing the full effect of the phonons on the system dynamics, as also concluded in [1]. Only few approaches have been done in the literature in describing the QD-cavity interacting with a non-Markovian reservoir

Until this point in this thesis, we have not demonstrated any new physical features with this model, which are not seen in the literature. But we have provided a solid understanding of the physics covered in the model, and in the rest of the thesis we will exploit it to gain new insight of the physics in this model, which to our knowledge not have been demonstrated in the literature.

Chapter 6

Pure Dephasing and Indistinguishability

Recently we have been able to improve the calculation scheme for the system dynamics described in Section 4.3, originally presented in [1, 69]. In Section 6.1 we present a way to determine an analytic expression for the time evolution operator $U(t)$, which may be used to find reduced expressions for both $\gamma_{12}(t)$ and $\mathcal{G}^{\gtrless}(t)$, which are the terms describing the interaction between the cavity-QD system and the phonon bath, relevant when considering an initially excited QD. We exploit this to divide the phonon-induced pure dephasing rate into a long- and short-time contribution. Furthermore an analytic expression for the long-time pure dephasing rate is derived. In relation to these calculations and to the model in general, we discuss in Section 6.2 how to reduce the indistinguishability of the emitted photons by minimizing the pure dephasing from phonons.

6.1 Analytic expression for the phonon scattering terms

We recall from Section 4.3 that for an initially excited QD at $t = 0$, the important terms for the electron-phonon interaction are given by

$$\mathcal{G}^{\gtrless}(t) = \mathrm{i}\hbar^{-2}\int_0^t \mathrm{d}t'\, U_{11}^*(t')U_{21}(t')D^{\gtrless}(t'), \tag{6.1}$$

$$\gamma_{12}(t) = \hbar^{-2}\int_0^t \mathrm{d}t'\, \left[|U_{11}(t')|^2 D^{<}(t') - |U_{21}(t')|^2 D^{>}(t')\right], \tag{6.2}$$

where the time evolution operator for the QD-cavity system is

$$U(t) = \mathrm{e}^{-\mathrm{i}H_{\mathrm{S}}t/\hbar}, \quad H_{\mathrm{S}} = \hbar\begin{bmatrix} \Delta & g & 0 \\ g & 0 & 0 \\ 0 & 0 & 0 \end{bmatrix}, \tag{6.3}$$

and the phonon reservoir correlation function is

$$D^{\gtrless}(t) = \sum_{\mathbf{k}} |M^{\mathbf{k}}|^2 \left[n_{\mathbf{k}}\mathrm{e}^{\pm\mathrm{i}\omega_{\mathbf{k}}t} + (n_{\mathbf{k}}+1)\mathrm{e}^{\mp\mathrm{i}\omega_{\mathbf{k}}t}\right]. \tag{6.4}$$

6.1.1 Analytic expression for $U(t)$

To determine an analytic expression for $U(t)$, without any operators as in Eq. (6.3), we use Gram-Schmidt orthonormalisation to determine a basis, in which H_{S} is diagonal. The coordinate transformation matrix is denoted Q and the diagonal form of H_{S} in the new basis is denoted $\tilde{H}_{\mathrm{S}} = Q^{\mathrm{T}} H_{\mathrm{S}} Q$, where Q^{T} is the transposed of Q. The diagonalisation goes as follows and is described in standard textbooks on linear algebra [95]. In the case of $g = 0$, H_{S} is already diagonal, where $U(t)$ easily is evaluated, so we only consider the case $g \neq 0$.

The eigensolutions of the eigenvalue equation $H_{\mathrm{S}}\mathbf{v}_i = \hbar\lambda_i \mathbf{v}_i$, where $\mathbf{v}_i$ is the eigenvector corresponding to the eigenvector λ_i, are given by

$$\lambda_\pm = \frac{\Delta}{2} \pm \frac{1}{2}\sqrt{\Delta^2 + 4g^2}, \quad \mathbf{v}_\pm = \begin{bmatrix} g/\lambda_\mp \\ 1 \\ 0 \end{bmatrix}, \quad \lambda_0 = 0, \quad \mathbf{v}_0 = \begin{bmatrix} 0 \\ 0 \\ 1 \end{bmatrix}, \tag{6.5}$$

where $g \neq 0$ ensures that $\lambda_- \neq 0$. Each of the eigenvalues have the same algebraic and geometric multiplicity, meaning that the eigenvectors $\mathbf{v}_0$, $\mathbf{v}_+$, and $\mathbf{v}_-$ span a basis for the vector space in which H_{S} is diagonal.

The coordinate transformation matrix Q must consist of three normalized and ortogonal basis vectors, i.e. $\mathbf{v}_i \cdot \mathbf{v}_j = \delta_{ij}$. The Gram-Schmidt normalisation algorithm provides these from the set $\{\mathbf{v}_+, \mathbf{v}_-, \mathbf{v}_0\}$ and gives

$$Q = \begin{bmatrix} \frac{\lambda_+}{\sqrt{g^2+\lambda_+^2}} & -\frac{g}{\sqrt{g^2+\lambda_+^2}} & 0 \\ \frac{g}{\sqrt{g^2+\lambda_+^2}} & \frac{\lambda_+}{\sqrt{g^2+\lambda_+^2}} & 0 \\ 0 & 0 & 1 \end{bmatrix}, \quad \tilde{H}_{\mathrm{S}} = \hbar \begin{bmatrix} \lambda_+ & 0 & 0 \\ 0 & \lambda_- & 0 \\ 0 & 0 & 0 \end{bmatrix}, \tag{6.6}$$

where the eigenvalues appear in the diagonal of $\tilde{H}_{\mathrm{S}}$. The coordinate transformation is orthogonal, meaning $Q^T Q = QQ^T = I$, where I is the identity operator. In this new basis, $U(t)$ is given by

$$\begin{aligned}
\tilde{U}(t) &= Q^T U(t) Q \\
&= Q^T \left[I + (-\mathrm{i}t/\hbar) H_{\mathrm{S}} + (-\mathrm{i}t/\hbar)^2 H_{\mathrm{S}}^2 + \ldots \right] Q \\
&= I + (-\mathrm{i}t/\hbar) Q^T H_{\mathrm{S}} Q + (-\mathrm{i}t/\hbar)^2 Q^T H_{\mathrm{S}} Q Q^T H_{\mathrm{S}} Q + \ldots \\
&= I + (-\mathrm{i}t/\hbar)\tilde{H}_{\mathrm{S}} + (-\mathrm{i}t/\hbar)^2 \tilde{H}_{\mathrm{S}}^2 + \ldots \\
&= \begin{bmatrix} 1 + (-\mathrm{i}t)\lambda_+ + (-\mathrm{i}t)^2\lambda_+^2 + \ldots & 0 & 0 \\ 0 & 1 + (-\mathrm{i}t)\lambda_- + (-\mathrm{i}t)^2\lambda_-^2 + \ldots & 0 \\ 0 & 0 & 1 \end{bmatrix} \\
&= \begin{bmatrix} \mathrm{e}^{-\mathrm{i}t\lambda_+} & 0 & 0 \\ 0 & \mathrm{e}^{-\mathrm{i}t\lambda_-} & 0 \\ 0 & 0 & 1 \end{bmatrix}.
\end{aligned} \tag{6.7}$$

By transforming back to the original basis, we obtain a final expression for $U(t)$,

$$U(t) = Q\tilde{U}(t)Q^T = \begin{bmatrix} \frac{\lambda_+^2 \mathrm{e}^{-\mathrm{i}t\lambda_+} + g^2 \mathrm{e}^{-\mathrm{i}t\lambda_-}}{g^2+\lambda_+^2} & \frac{\lambda_+ g\left(\mathrm{e}^{-\mathrm{i}t\lambda_+} - \mathrm{e}^{-\mathrm{i}t\lambda_-}\right)}{g^2+\lambda_+^2} & 0 \\ \frac{\lambda_+ g\left(\mathrm{e}^{-\mathrm{i}t\lambda_+} - \mathrm{e}^{-\mathrm{i}t\lambda_-}\right)}{g^2+\lambda_+^2} & \frac{g^2 \mathrm{e}^{-\mathrm{i}t\lambda_+} + \lambda_+^2 \mathrm{e}^{-\mathrm{i}t\lambda_-}}{g^2+\lambda_+^2} & 0 \\ 0 & 0 & 1 \end{bmatrix}, \tag{6.8}$$

with $\lambda_\pm = \frac{\Delta}{2} \pm \frac{1}{2}\sqrt{\Delta^2 + 4g^2}$. This expression fulfils the unitary requirement $U(t)U^\dagger(t) = I$.

For the calculations of $\gamma_{12}(t)$ and $\mathcal{G}^{\gtrless}(t)$ we need the three products between matrix elements of $U(t)$, where we use that $\lambda_+ - \lambda_- = \sqrt{\Delta^2 + 4g^2}$,

$$|U_{11}(t)|^2 = \frac{1}{(g^2+\lambda_+^2)^2}\left[\lambda^4 + g^4 + \lambda^2 g^2\left(\mathrm{e}^{-\mathrm{i}t\sqrt{\Delta^2+4g^2}} + \mathrm{e}^{\mathrm{i}t\sqrt{\Delta^2+4g^2}}\right)\right] \tag{6.9}$$

$$= 1 - \frac{2\lambda_+^2 g^2}{(g^2+\lambda_+^2)^2}\left[1 - \cos(t\sqrt{\Delta^2+4g^2})\right], \tag{6.10}$$

and

$$|U_{21}(t)|^2 = \frac{\lambda_+^2 g^2}{(g^2+\lambda_+^2)^2}\left[2 - \mathrm{e}^{-\mathrm{i}t\sqrt{\Delta^2+4g^2}} - \mathrm{e}^{\mathrm{i}t\sqrt{\Delta^2+4g^2}}\right] \tag{6.11}$$

$$= \frac{2\lambda_+^2 g^2}{(g^2+\lambda_+^2)^2}\left[1 - \cos(t\sqrt{\Delta^2+4g^2})\right], \tag{6.12}$$

where we confirm that $|U_{11}(t)|^2 + |U_{21}(t)|^2 = 1$, caused by the unitarity of $U(t)$. As the last product, we calculate

$$U_{11}^*(t)U_{21}(t) = \frac{\lambda_+ g}{(g^2+\lambda_+^2)^2}\left(\lambda_+^2 - g^2 - \lambda_+^2\mathrm{e}^{\mathrm{i}t\sqrt{\Delta^2+4g^2}} + g^2\mathrm{e}^{-\mathrm{i}t\sqrt{\Delta^2+4g^2}}\right) \tag{6.13}$$

$$= \frac{\lambda_+ g}{g^2+\lambda_+^2}\left[\frac{\lambda_+^2 - g^2}{g^2+\lambda_+^2}\Big(1 - \cos(t\sqrt{\Delta^2-4g^2})\Big) + \mathrm{i}\sin(t\sqrt{\Delta^2-4g^2})\right], \tag{6.14}$$

using that for any value of a variable x, $a\exp(\mathrm{i}x) + b\exp(-\mathrm{i}x) = (a+b)\cos(x) + \mathrm{i}(a-b)\sin(x)$.

6.1.2 The scattering terms

The function $\gamma_{12}(t)$ in Eq. (6.2) may be calculated with Eqs. (6.10) and (6.12),

$$\gamma_{12}(t) = \hbar^{-2}\int_0^t \mathrm{d}t'\, D^<(t') - \hbar^{-2}\frac{4\lambda_+^2 g^2}{(g^2+\lambda_+^2)^2}\int_0^t \mathrm{d}t'\, \left[1 - \cos(t'\sqrt{\Delta^2+4g^2})\right]\mathrm{Re}\{D^<(t')\}, \tag{6.15}$$

exploiting that $[D^>(t)]^* = D^<(t)$. The first term in Eq. (6.15) does not contain Δ or g and is solely described from the bare electron-phonon interaction. The second term is real and cavity-dependent, and we see that $\gamma_{12}(t)$ attains the same value for $\pm\Delta$, which is should according to the discussion in Section 5.2. Thus we only discuss γ_{12} for $\Delta > 0$. We recall from Section 4.3 that $\mathrm{Im}\{\gamma_{12}(t)\}$ was an energy shift introduced due to the electron-phonon quasiparticle. Thus we should not expect it to be dependent on the presence of the cavity, which is also what we see.

In Eq. (6.15) it is clearly pointed out, that the rate pure dephasing rate consists of a part only due to the electron-phonon interaction, and a part which is zero for $g = 0$ and thus describes interaction of the electron-phonon quasiparticle with the cavity mode. By inserting the expression for $D^<(t)$ into Eq. (6.15) and evaluating the integrals, the contribution to the

pure dephasing rate $\gamma_{12}(t) = \gamma_{12,\text{e-ph}}(t) + \gamma_{12,\text{cavity}}(t)$ becomes

$$\text{Re}\{\gamma_{12,\text{e-ph}}(t)\} = \hbar^{-2}\sum_{\mathbf{k}}|M^{\mathbf{k}}|^2(2n_{\mathbf{k}}+1)\frac{\sin(\omega_{\mathbf{k}}t)}{\omega_{\mathbf{k}}} \tag{6.16}$$

$$\begin{aligned}\text{Re}\{\gamma_{12,\text{cavity}}(t)\} &= \hbar^{-2}\frac{4\lambda_+^2 g^2}{(g^2+\lambda_+^2)^2}\sum_{\mathbf{k}}|M^{\mathbf{k}}|^2(2n_{\mathbf{k}}+1) \\ &\times\left[-\frac{\sin(\omega_{\mathbf{k}}t)}{\omega_{\mathbf{k}}}+\frac{1}{2}\frac{\sin([\omega_{\mathbf{k}}-\sqrt{\Delta^2+4g^2}]t)}{\omega_{\mathbf{k}}-\sqrt{\Delta^2+4g^2}}+\frac{1}{2}\frac{\sin([\omega_{\mathbf{k}}+\sqrt{\Delta^2+4g^2}]t)}{\omega_{\mathbf{k}}+\sqrt{\Delta^2+4g^2}}\right]\end{aligned} \tag{6.17}$$

The imaginary part of $\gamma_{12}(t)$ may easily be calculated from Eq. (6.15).

The function $\mathcal{G}^{\gtrless}(t)$ may also be calculated by evaluating the integral in the same way, but is the expression becomes longer,

$$\begin{aligned}\mathcal{G}^{\gtrless}(t) &= \mathrm{i}\hbar^{-2}\frac{\lambda_+ g}{g^2+\lambda_+^2}\int_0^{t'}\mathrm{d}t\left[\frac{\lambda_+^2-g^2}{g^2+\lambda_+^2}\Big(1-\cos(t'\sqrt{\Delta^2+4g^2})\Big)+\mathrm{i}\sin(t'\sqrt{\Delta^2+4g^2})\right]D^{\gtrless}(t') \\ &= \mathrm{i}\hbar^{-2}\frac{\lambda_+ g}{g^2+\lambda_+^2}\sum_{\mathbf{k}}|M^{\mathbf{k}}|^2 f(t)\end{aligned} \tag{6.18}$$

where the function $f(t)$ is a long expression containing terms constant in time plus both imaginary and real terms proportional to $\sin(at)/a$ and $\cos(at)/a$ where $a \in \{\omega_{\mathbf{k}}, \omega_{\mathbf{k}} \pm \sqrt{\Delta^2+4g^2}\}$. $f(t)$ may easily be calculated, so we will not state the explicit expression here.

Summarizing, we have with an analytic expression of $U(t)$ been able to carry out the t-integration. In the numerical implementation of the model, only the $\mathbf{k}$-sum has to be carried out, giving a reduced calculation time when using Eq. (6.16), (6.17), and (6.18), compared to calculating $\gamma_{12}(t)$ and $\mathcal{G}^{\gtrless}(t)$ all numerically.

The limit $t \to \infty$

As we saw in Section 5.2.3, the phonon bath correlation function, $D^{\gtrless}(t)$, only varies in the first $\sim 5\,\text{ps}$, after which $D^{\gtrless}(t)$ more or less is zero. Thus $\mathcal{G}^{\gtrless}(t)$ and $\gamma_{12}(t)$ attains an almost constant value after $\sim 5\,\text{ps}$, which may be calculated as the limit $t \to \infty$. This could be obtained by taking the limit in Eqs. (6.17) and (6.18), but may more easily be calculated from the expressions before the t-integration is carried out. We will only consider $\gamma_{12}(t \to \infty)$, since we at present not have obtained any new physical insight from the expression of $\mathcal{G}^{\gtrless}(t \to \infty)$. By using the definition of the Fourier transform given in Eq. (5.15) to transform Eqs. (6.9) and (6.11) in the limit $t \to \infty$, and by using the property of the D-function $[D^{<}(\omega)]^* = D^{>}(-\omega)$, we obtain by simple algebraic manipulation

$$\begin{aligned}\gamma_{12}(t\to\infty) &= \hbar^{-2}D^{<}(\omega=0)+\hbar^{-2}\frac{4\lambda_+^2 g^2}{(g^2+\lambda_+^2)^2}\Big[-\text{Re}\{D^{>}(\omega=0)\} \\ &\quad+\frac{1}{2}\text{Re}\{D(\omega=\sqrt{\Delta^2+4g^2})\}+\frac{1}{2}\text{Re}\{D(\omega=-\sqrt{\Delta^2+4g^2})\}\Big],\end{aligned} \tag{6.19}$$

using the relation $2\,\mathrm{Re}\{z\} = z + z^*$ for a complex parameter z. Using that $\mathrm{Re}\{D^>(\omega = 0)\} = 0$, we divide $\gamma_{12}(t \to \infty)$ into a real and an imaginary part,

$$\begin{aligned}\mathrm{Re}\{\gamma_{12}(t\to\infty)\} &= \hbar^{-2}\frac{4\lambda_+^2 g^2}{(g^2+\lambda_+^2)^2}\cdot\frac{1}{2}\Big[\mathrm{Re}\{D^>(\omega=\sqrt{\Delta^2+4g^2})\} \\ &\qquad +\mathrm{Re}\{D^>(\omega=-\sqrt{\Delta^2+4g^2})\}\Big], \qquad (6.20)\\ \mathrm{Im}\{\gamma_{12}(t\to\infty)\} &= \hbar^{-2}\mathrm{Im}\{D^<(\omega=0)\}. \qquad (6.21)\end{aligned}$$

In general we are not able to determine $\mathrm{Im}\{D^<(\omega = 0)\}$ and thus the imaginary part of $\gamma_{12}(t)$. But the real part is everywhere non-negative and is described as the product of factor $4\lambda_+^2 g^2/(g^2+\lambda_+^2)^2$ describing the coupling to the cavity and a factor only related to the electron-phonon coupling by the effective phonon spectrum, $\mathrm{Re}\{D^>(\omega)\}$. From this we are able to draw important physical conclusions, which will be discussed in the following section.

6.2 Indistinguishability

As introduced in Chapter 1, indistinguishability of the emitted photons plays an important role in the realization of a good single photon source. From Eq. (1.1) we may express the degree of indistinguishability, defined as the coherence time divided by the lifetime of the excited QD state, by rates, in a phenomenological way,

$$\text{Degree of indistinguishability} = \frac{\Gamma_{\mathrm{tot}}}{\Gamma_{\mathrm{tot}} + \gamma_{\mathrm{tot}} + \mathrm{Re}\{\gamma_{12}\}} \qquad (6.22)$$

where Γ_{tot} is the total decay rate of the excited QD state, and $\gamma_{\mathrm{tot}} = (\Gamma+\kappa)/2 + \gamma$ is the total dephasing rate without including the phonons.

In the limit $g \ll \Delta$, we saw in Eq. (5.17) that Γ_{tot} was increased by electron-phonon scattering, which would increase the indistinguishability. But as stated in Eq. (6.15), the interaction also contribute by a pure dephasing rate, which would decrease the indistinguishability. The problem is now to determine the optimal balance between these two effects to achieve the highest indistinguishability.

According to the matrix elements described in Section 4.3, both $\mathrm{Im}\{\mathcal{G}^{\gtrless}(t)\}$ and $\mathrm{Re}\{\gamma_{12}(t)\}$ give phonon-contributions to dephasing, whereas only the latter is given by a pure dephasing rate. Both of these have to be taken into account, when calculating a precise effect of the dephasing, but it is difficult to tell exactly how $\mathcal{G}^{\gtrless}(t)$ influences, see [1] for an elaborating discussion of the dynamics due to $\mathcal{G}^{\gtrless}(t)$. In this thesis we discuss how to reduce the phonon-induced decoherence *only* by minimizing the pure dephasing without including the effect of $\mathcal{G}^{\gtrless}(t)$, which gives an incomplete, but still gainful picture.

Pure dephasing for small times

A plot of $\gamma_{12}(t)$ is given in Fig. 6.1a where the dependence of the temperature and the wavefunction width is examined. $\mathrm{Re}\{\gamma_{12}(t)\}$ increases initially and peaks around $t = 1\,\mathrm{ps}$, from which it decreases and converges toward a non-zero value $\mathrm{Re}\{\gamma_{12}(\infty)\}$. It is reasonable to believe that the total effect of pure dephasing from electron-phonon interaction depends both on the amplitude of the peak appearing at low times and of $\mathrm{Re}\{\gamma_{12}(\infty)\}$. The peak appears due to

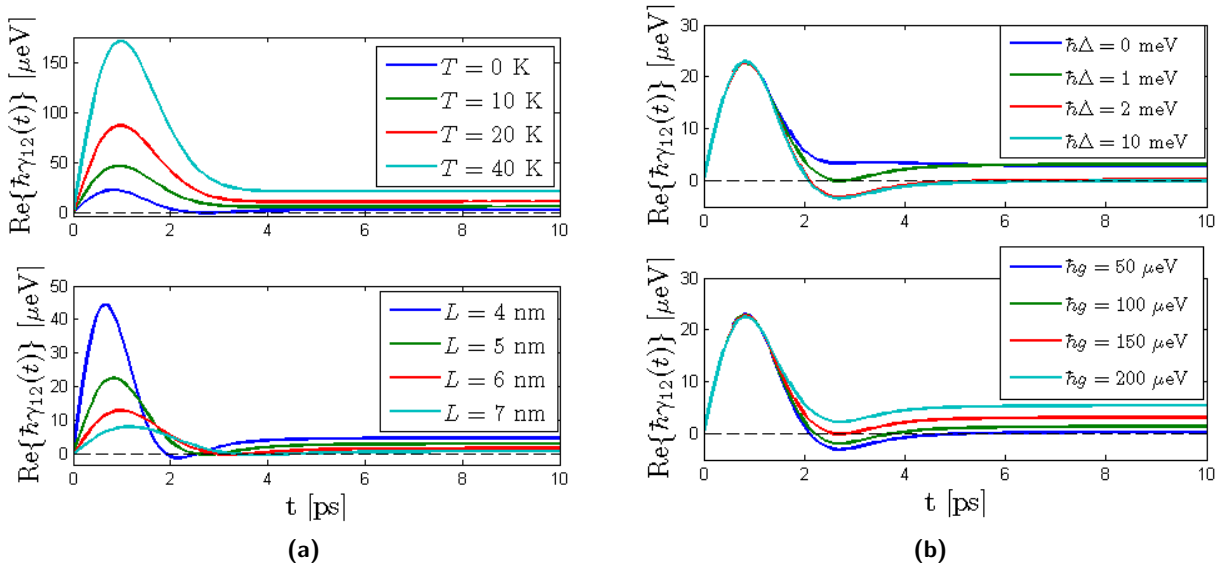

Figure 6.1: **(a)** The time evolution of the pure dephasing rate, $\mathrm{Re}\{\gamma_{12}(t)\}$, plotted for different temperatures and widths of the carrier wavefunction. When nothing else is mentioned, $T = 0\,\mathrm{K}$, $L = 5\,\mathrm{nm}$, $\hbar\Delta = 1\,\mathrm{meV}$, and $\hbar g = 150\,\mu\mathrm{eV}$. **(b)** The pure dephasing rate $\mathrm{Re}\{\gamma_{12}(t)\}$ plotted for different values of the detuning and of the coupling strengths. When nothing else is mentioned, $T = 0\,\mathrm{K}$, $L = 5\,\mathrm{nm}$, $\hbar\Delta = 1\,\mathrm{meV}$, and $\hbar g = 150\,\mu\mathrm{eV}$.

the behaviour of $D^{\gtrless}(t)$, which varies initially until $\sim 5\,\mathrm{ps}$ and then dies out. The D-function depends on the electron and phonon properties only, so we expect that the appearance of the peak is not affected by the cavity-related parameters.

It should though be noted from Fig. 6.1a, that an increase in either T or L enhances both the peak amplitude and the long-time value. This agrees with Eqs. (6.16) and (6.17) and the discussion in Chapter 5, where it was shown that an increase in either T or L enhances the electron-phonon interaction.

The parameters concerning the cavity-coupling, Δ and g, are varied in Fig. 6.1b for $\gamma_{12}(t)$. The magnitude of the peak does not change when varying Δ or g as we expected, since the peak appears due to the bare electron-phonon interaction. In the case of $\Delta \to \infty$ or $g = 0$, the cavity no longer couples to the electron-phonon system, and $\gamma_{12}(\infty) = 0$, and thus the pure dephasing of a bare electron-phonon system depends on the amplitude of the peak only.

Pure dephasing in the large time limit

With crude wavefunction assumption in Eq. (5.6), the pure dephasing in the large-time limit may be obtained an all analytical expression. An insertion of Eq. (5.19) into Eq. (6.20), gives

$$\mathrm{Re}\{\gamma_{12}(t\to\infty)\} = \frac{2\lambda_+^2 g^2}{\hbar^2(g^2+\lambda_+^2)^2}\frac{\hbar(D_e-D_g)^2}{4\pi\rho c_l^5}\omega_+^3 \mathrm{e}^{-\omega_+^2 L^2/(2c_l^2)}\coth\left(\frac{\beta\hbar\omega_+}{2}\right), \tag{6.23}$$

where $\lambda_+ = \frac{\Delta}{2}+\frac{1}{2}\sqrt{\Delta^2+4g^2}$, $\omega_+ = \sqrt{\Delta^2+4g^2}$, and $\coth(\beta\hbar\omega_+/2) = (1+\mathrm{e}^{-\beta\hbar\omega_+})/(1-\mathrm{e}^{-\beta\hbar\omega_+})$.

In Fig. 6.2a we compare the value of $\mathrm{Re}\{\gamma_{12}(\infty)\}$ achieved from the simulation with the exact solution, plotted for varying Δ. The deviations between the two results are due to numerical

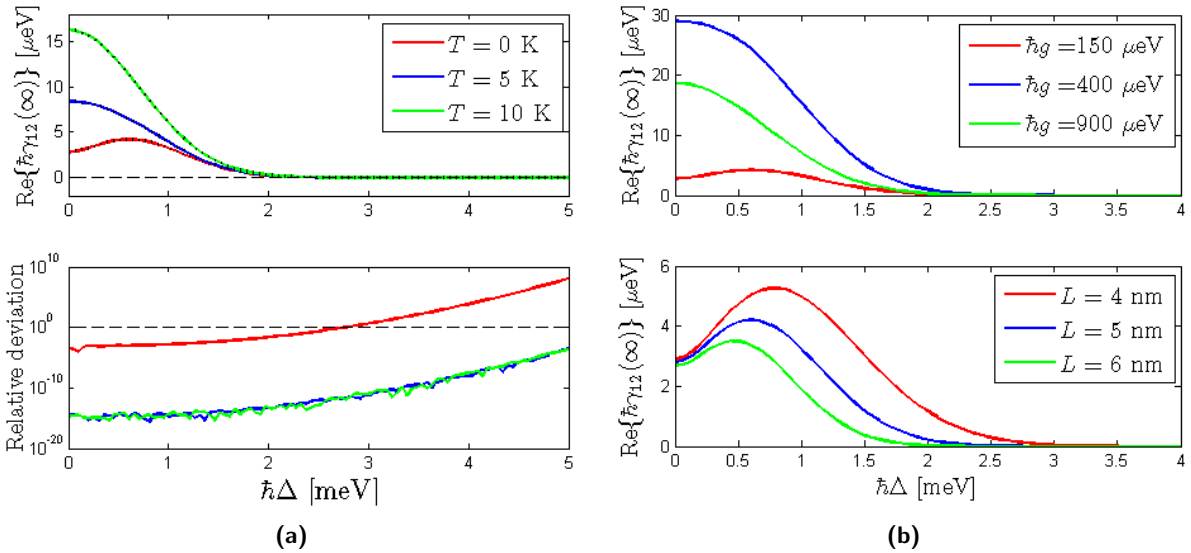

Figure 6.2: **(a)** (Top) $\mathrm{Re}\{\gamma_{12}(\infty)\}$ vs. detuning for varying temperatures extracted from simulations. The black dotted lines are the corresponding values obtained from the analytic expression in Eq. (6.23), and the parameters values are similar to those in Fig. 6.1a when nothing else is mentioned. (Bottom) The relative deviation between the analytic expression and the simulated values, calculated as $|\mathrm{Re}\{\gamma_{12,\mathrm{sim}}(\infty)\} - \mathrm{Re}\{\gamma_{12,\mathrm{ana}}(\infty)\}|/\mathrm{Re}\{\gamma_{12,\mathrm{ana}}(\infty)\}$ **(b)** The same as the top figure in Fig. 6.2a, but varying g (top) and L (bottom), using $T = 0\,\mathrm{K}$.

inaccuracies and the deviations become significant only when $\mathrm{Re}\{\gamma_{12}(\infty)\}$ is almost zero, which confirms that enough points are used in the simulation. An important thing to notice, is that for low temperatures, the smallest highest value of $\mathrm{Re}\{\gamma_{12}(\infty)\}$ not necessarily is achieved for $\Delta = 0$. A way to understand this is obtained by considering Eq. (6.20), which states that $\mathrm{Re}\{\gamma_{12}(\infty)\}$ is a cavity-dependent pre-factor times the sum of the values of the effective phonon spectrum at $\omega = \pm\sqrt{\Delta^2 + 4g^2}$. The effective phonon spectrum was plotted in Fig. 5.7a and had two peaks at around $\omega = \pm 1\,\mathrm{meV}$, meaning that the value of $\mathrm{Re}\{\gamma_{12}(\infty)\}$ is largest when the value $\sqrt{\Delta^2 + 4g^2}$ is around $1\,\mathrm{meV}$. For a near-resonant system (small Δ) at low temperatures, when the thermal effects not are significant, we may actually expect a smaller contribution to the pure dephasing rate from the cavity-coupling for low coupling strengths than when g is increased (until the peak is reached). To our knowledge this effect has not been demonstrated in the litterature, but as seen in Fig. 6.2a this effect only appears for very low temperature, so in practice this effect probably will be insignificant.

The pure dephasing rate for different g is also calculated, see Fig. 6.2b. It is clearly seen that there exists a value of g, for which the largest dephasing is achieved, here demonstrated for $g = 400\,\mu\mathrm{eV}$. The experimentally achievable value of g is though typically below $200\,\mu\mathrm{eV}$, see Appendix A. Furthermore the behaviour in the limits of strong $g \gg \Delta$ and weak $g \ll \Delta$ cavity influence is illustrated clearly, and this should be compared to Eq. (6.20):

- For $g \gg \Delta$, the cavity pre-factor in Eq. (6.20) is equal to 1, but the effective phonon spectrum is small when evaluated at large frequencies, and in the limit $g \to \infty$, $\mathrm{Re}\{\gamma_{12}(\infty)\}$ is zero for all Δ. A high g decouples the phonons from the polarition, such that no acoustic phonons have high enough energy to assist in the QD-cavity coupling.

- For $g \ll \Delta$, the cavity pre-factor in Eq. (6.20) is zero and thus $\mathrm{Re}\{\gamma_{12}(\infty)\} = 0$. Physically the QD cannot decay through the cavity and the pure dephasing of the phonons is only caused by the bare electron-phonon interaction.

To determine how the electronic confinement affect the dephasing, we plot $\mathrm{Re}\{\gamma_{12}(\infty)\}$ for different values of L, see Fig. 6.2b. As L decreases, the pure dephasing rate increases due to enhanced electron-phonon coupling as discussed in Chapter 5.

6.3 Summary and discussion

We have shown how to obtain reduced expressions for $\gamma_{12}(t)$ and $\mathcal{G}^{\gtrless}$ by determining an analytic expression of $U(t)$. These expression may be used to improve the calculation in the numerical implementation of the model[1]. We have shown that the derived expression for $\mathrm{Re}\{\gamma_{12}(t \to \infty)\}$ fits very well with the values obtained from the simulations. We divided the phonon contribution to the pure dephasing rate, $\mathrm{Re}\{\gamma_{12}\}$, into two parts, the long- and the short-time effects:

- The long-time rate in Eq. (6.20) depends on the value of the effective phonon spectrum in $\omega = \pm\sqrt{\Delta^2 + 4g^2}$. For the crude wavefunction approximation, the pure dephasing is minimized when $\Delta = 0$ for small g, where the cavity-coupling strength is low and where the value of the effective phonon spectrum, $\mathrm{Re}\{D^{>}(\omega)\}$ given in Fig. 5.7a, when evaluated in $\omega = \pm\sqrt{\Delta^2 + 4g^2}$, is close to zero.

- The short-time effect depends solely on the electron-phonon coupling. In contrast to the long-time limit rate which depends on the value of the effective phonon spectrum evaluated at specific frequencies, the short time rate depends on a sampling over the whole effective phonon spectrum. This is due to the incomplete Fourier transform in Eq. (6.15), because the upper limit in the integral is t and not ∞. To minimize this contribution to the pure dephasing rate, the amplitude of the whole effective phonon spectrum should be decreased.

According to the differential equation system in Section 4.3, the phonon-induced pure dephasing rate is added to $\gamma_{\mathrm{tot}} = (\Gamma + \kappa)/2 + \gamma \approx 50\,\mu\mathrm{eV}$ to give the total decay rate of the polarisation $\langle\sigma_{12}(t)\rangle$ in the equations of motion. For low temperatures, the long-time rate is negligible, and the cavity-contribution to the pure dephasing rate may be neglected. At higher temperatures, both the short- and long- time rates are comparable to γ_{tot} and should be included.

The phonon-assisted cavity feeding introduces higher shorter lifetimes of the QD, which would improve the indistinguishability, but the phonons also induce dephasing, which decreases the indistinguishability. The optimal indistinguishability is obtained when these effects are in balance. We only considered the pure dephasing contribution from the phonons by γ_{12}. In a complete description, the dephasing effect in $\mathcal{G}^{\gtrless}$ should also be included, but this is not straight-forward so we only discuss indistinguishability in relation to γ_{12}.

When considering the crude wavefunction approximation and bulk phonons, the optimal design of a single-photon emitter with high indistinguishability would have $\Delta = 0$, where the excited QD state has a low lifetime, and the long-time contribution to the pure dephasing is almost zero (the effective phonon spectrum evaluated in $\pm g$ is small for realistic values of g for the used parameters. In the next two chapters we will examine if a change in the electronic or phononic confinement will make it viable to consider $\Delta \neq 0$.

[1]This was, however, realized late in the working process, so we did not have time to implement it in our calculations. We used the full approach by determining $U(t)$ numerically and carrying out the integration over t.

Chapter 7

Engineering the Electronic Confinement

In some publications concerning electron-phonon interaction, the electronic confinement is described by the crude wavefunction in Eq. (5.6) where the an electron in the ground and excited state are assume to be described by the same, spherical wavefunction [44]. The effective mass of an electron in the excited state (described by the conduction band) is though smaller than for an electron in the ground state (described by the valence band), giving a larger wavefunction width of the excited state than for the ground state. Some publications on electron-phonon interaction uses this more physical wavefunction [76], and some even consider the possibility of having an ellipsoidal wavefunction which take into account the confinement in the growth direction of the QD [43, 90, 87]. Common to all of them is that a an extensive examination of the influence of the wavefunction shape and width on the electron-phonon interaction never has been carried out. To our knowledge, the closest approach is made in [42], where the electronic confinement is changed by an applied field or a built-in field. Their analysis is restricted to only described the effect of the acoustic phonons by a pure dephasing, and they model the quantum dot structure by a potential well in the growth direction of the QD and by a two-dimensional harmonic-oscillator potential perpendicular to the growth direction. The only conclusion about the electronic confinement is that a small QD gives a large electron-acoustic interaction, which we also previously have demonstrated. They focus more on the difference between GaAs and GaN-quantum dots, as discussed in Section 2.3.

In this chapter we investigate in details of how the electronic confinement affects the dynamics in the system, when considering bulk LA-phonons obeying the linear dispersion relation $\omega_{\mathbf{k}} = |\mathbf{k}|c_l$. The is done by analytical considerations in Section 7.1, where we assume an ellipsoidal wavefunction. Realistic quantum dot structures may have different sizes and shapes, see Figs. 7.1a and 7.1b. By calculating actual wavefunctions in QD structures using the finite element method (FEM) in Section 7.2, we test how well the ellipsoidal approximation may be used to describe the wavefunctions of the calculated structures. In both sections we discuss how the electronic confinement affects the lifetime asymmetry introduced in Chapter 5 and the indistinguishability treated in Chapter 6.

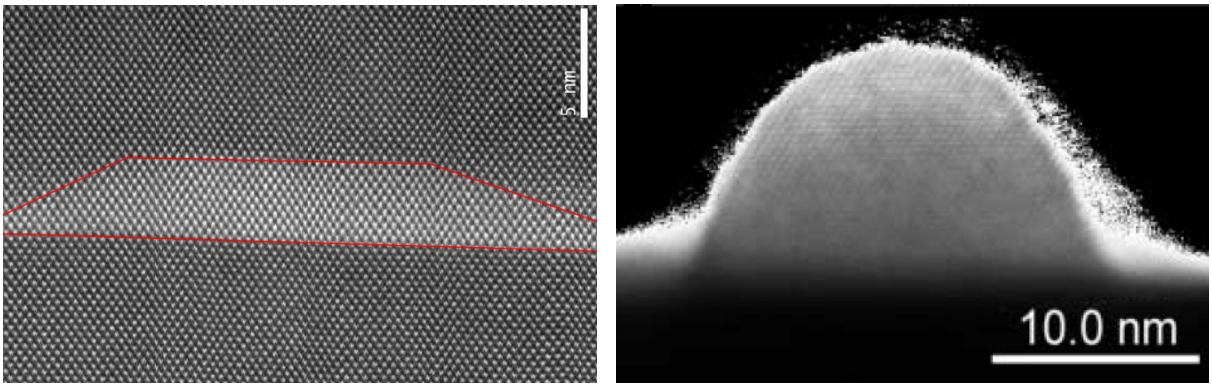

Figure 7.1: **(a)** InAs/InP QD grown at Danchip and characterized at CEN, both at DTU (courtesy of K. Yvind, DTU). The white bar in the upper corner is 5 nm long. **(b)** TEM picture of a lens-shaped InAs QD grown on GaAs [23] (courtesy of Dr. J. P. McCaffrey, IMS NRC Canada).

7.1 Analytic wavefunction

In the analytic part we assume an ellipsoidal wavefunction on the (normalized) form

$$\phi_\nu(\mathbf{r}) = \frac{1}{\pi^{3/4} l_{\nu,xy} l_{\nu,z}^{1/2}} \mathrm{e}^{-(x^2+y^2)/(2l_{\nu,xy}^2)} \mathrm{e}^{-z^2/(2l_{\nu,z}^2)}. \tag{7.1}$$

Here we assume that the QD is grown in the z-direction, such that it has one width parameters concerning the confinement in that direction, $l_{\nu,z}$, and another width $l_{\nu,xy}$ describing the confinement in the plane perpendicular to the growth direction. The index $\nu \in \{g, e\}$ refers to the wavefunction width of an electron in either the ground or the excited state.

From Eq. (4.5) we recall the expression for the interaction matrix element, which for bulk phonons is

$$M_{\nu\nu}^{\mathbf{k}} = \sqrt{\frac{\hbar k}{2 d c_l V}} D_\nu \int \mathrm{d}\mathbf{r} \, |\phi_\nu(\mathbf{r})|^2 \mathrm{e}^{\mathrm{i}\mathbf{k}\cdot\mathbf{r}}, \tag{7.2}$$

where the density in this chapter is denoted d instead of ρ, which in this chapter refers to the radial component in a cylindrical coordinate system. For the ellipsoidal model we may advantageous use cylindrical coordinate representation and split up the wavevector $\mathbf{k}$ into a radial part, $\mathbf{k}_\rho$, and an axial part, k_z,

$$\int \mathrm{d}\mathbf{r} \, |\phi_\nu(\mathbf{r})|^2 \mathrm{e}^{\mathrm{i}\mathbf{k}\cdot\mathbf{r}} = \frac{1}{\pi^{3/2} l_{\nu,xy}^2 l_{\nu,z}} \int \mathrm{d}\boldsymbol{\rho} \, \mathrm{e}^{-\rho^2/l_{\nu,xy}^2 + \mathrm{i}\mathbf{k}_\rho\cdot\boldsymbol{\rho}} \times \int_{-\infty}^{\infty} \mathrm{d}z \, \mathrm{e}^{-z^2/l_{\nu,z}^2 + \mathrm{i}k_z z}. \tag{7.3}$$

The first integral is calculated in [96], and the second is easily evaluated, giving

$$\begin{aligned} \int \mathrm{d}\mathbf{r} \, |\phi_\nu(\mathbf{r})|^2 \mathrm{e}^{\mathrm{i}\mathbf{k}\cdot\mathbf{r}} &= \frac{1}{\pi^{3/2} l_{\nu,xy}^2 l_{\nu,z}} \times \pi l_{\nu,xy}^2 \mathrm{e}^{-k_\rho^2 l_{\nu,xy}^2/4} \times \sqrt{\pi} l_{\nu,z} \mathrm{e}^{-k_\rho^2 l_{\nu,z}^2/4} \\ &= \mathrm{e}^{-k_\rho^2 l_{\nu,xy}^2/4 - k_z^2 l_{\nu,z}^2/4}. \end{aligned} \tag{7.4}$$

Using Eq. (5.13) to transform the **k**-sum into an integral, and remembering the definition $M^{\mathbf{k}} = M^{\mathbf{k}}_{ee} - M^{\mathbf{k}}_{gg}$, the phonon bath correlation function may be written as

$$D(t) = \sum_{\mathbf{k}} |M^{\mathbf{k}}|^2 \left[n_{\mathbf{k}} \mathrm{e}^{\pm \mathrm{i}\omega_{\mathbf{k}} t} + (n_{\mathbf{k}}+1)\mathrm{e}^{\mp \mathrm{i}\omega_{\mathbf{k}} t} \right] \tag{7.5}$$

$$= \frac{\hbar}{4\pi^2 d c_l} \int_0^\infty \mathrm{d}k_\rho \, k_\rho \int_0^\infty \mathrm{d}k_z \, k \Big| D_e \mathrm{e}^{-k_\rho^2 l_{e,xy}^2/4 - k_z^2 l_{e,z}^2/4} - D_g \mathrm{e}^{-k_\rho^2 l_{g,xy}^2/4 - k_z^2 l_{g,z}^2/4} \Big|^2 \times \left[n_{\mathbf{k}} \mathrm{e}^{\pm \mathrm{i}\omega_{\mathbf{k}} t} + (n_{\mathbf{k}}+1)\mathrm{e}^{\mp \mathrm{i}\omega_{\mathbf{k}} t} \right], \tag{7.6}$$

with $k_\rho = |\mathbf{k}_\rho|$, and where we exploit that the integrand is an even function in k_z to change the integration limits.

7.1.1 The effective phonon spectrum

As in Section 5.2.3, information about the phonons may be gained by considering the effective phonon spectrum, $\mathrm{Re}\{D^>(\omega)\}$, which may be obtained by applying the Fourier transform from Eq. (5.15). In the derivations we changed the integration parameter in the k_ρ-integral to an integral over frequency using the relations $k = \sqrt{k_\rho^2 + k_z^2}$ and $\omega_{\mathbf{k}} = c_l |\mathbf{k}|$, giving

$$\mathrm{Re}\{D^>(\omega)\} = \frac{\hbar}{4\pi d c_l^4} \int_0^\infty \mathrm{d}k_z \int_{k_z c_l}^\infty \mathrm{d}\omega_{\mathbf{k}} \, \omega_{\mathbf{k}}^2 \Big| D_e \mathrm{e}^{-[(\omega_{\mathbf{k}}/c_l)^2 - k_z^2] l_{e,xy}^2/4 - k_z^2 l_{e,z}^2/4} \tag{7.7}$$

$$- D_g \mathrm{e}^{-[(\omega_{\mathbf{k}}/c_l)^2 - k_z^2] l_{g,xy}^2/4 - k_z^2 l_{g,z}^2/4} \Big|^2 \times \left[n_{\mathbf{k}} \delta(\omega + \omega_{\mathbf{k}}) + (n_{\mathbf{k}}+1)\delta(\omega - \omega_{\mathbf{k}}) \right]. \tag{7.8}$$

By mathematical considerations we have that for any even function $g(\omega_{\mathbf{k}})$, with $k_z > 0$,

$$\int_{k_z c_l}^\infty \mathrm{d}\omega_{\mathbf{k}} \, g(\omega_{\mathbf{k}}) \left[n_{\mathbf{k}} \delta(\omega + \omega_{\mathbf{k}}) + (n_{\mathbf{k}}+1)\delta(\omega - \omega_{\mathbf{k}}) \right] = g(\omega) n_{\omega_{\mathbf{k}} = -\omega} \frac{-|\omega|}{\omega} \theta(|\omega| - k_z c_l). \tag{7.9}$$

using that $n_{\omega_{\mathbf{k}}=-\omega} = -(n_{\omega_{\mathbf{k}}=\omega} + 1)$ from the definition of $n_{\mathbf{k}}$ in Eq. (4.51). By applying this, we obtain a reduced expression for the phonon spectrum,

$$\mathrm{Re}\{D^>(\omega)\} = \frac{\hbar}{4\pi d c_l^4} \frac{\omega|\omega|}{1 - \mathrm{e}^{-\beta\hbar\omega}} \int_0^{|\omega|/c_l} \mathrm{d}k_z \left| D_e \mathrm{e}^{-[(\omega/c_l)^2 - k_z^2] l_{e,xy}^2/4 - k_z^2 l_{e,z}^2/4} \right. \tag{7.10}$$

$$\left. - D_g \mathrm{e}^{-[(\omega/c_l)^2 - k_z^2] l_{g,xy}^2/4 - k_z^2 l_{g,z}^2/4} \right|^2. \tag{7.11}$$

By introducing the unit-less integration parameter, $\tilde{\omega} = k_z c_s / |\omega|$,

$$\mathrm{Re}\{D^>(\omega)\} = \frac{\hbar}{4\pi d c_l^5} \frac{\omega^3}{1 - \mathrm{e}^{-\beta\hbar\omega}} \int_0^1 \mathrm{d}\tilde{\omega} \left| D_e \mathrm{e}^{-(1-\tilde{\omega}^2)\omega^2 l_{e,xy}^2/(4c_l^2) - k_z^2 l_{e,z}^2/4} \right. \tag{7.12}$$

$$\left. - D_g \mathrm{e}^{-(1-\tilde{\omega}^2)\omega^2 l_{g,xy}^2/(4c_l^2) - k_z^2 l_{g,z}^2/4} \right|^2. \tag{7.13}$$

This expression is similar to the expression for the crude wavefucntion in Eq. (5.19) and only differ in the last factor concerning the electronic dependence. The temperature dependence still appears as a separate factor.

Spherical wavefunction

To develop an understanding of Eq. (7.13), we start by considering the case of spherical wave functions, where the difference in wavefunctions widths due to different effective masses of the conduction and valence is taken into account, i.e. $L_e = l_{e,xy} = l_{e,z}$ and $L_g = l_{g,xy} = l_{g,z}$, in which case Eq. (7.13) reduces to

$$\mathrm{Re}\{D^{>}(\omega)\} = \frac{\hbar}{4\pi d c_l^5} \frac{\omega^3}{1 - \mathrm{e}^{-\beta\hbar\omega}} \left[D_e \mathrm{e}^{-\omega^2 L_e^2/(4c_l^2)} - D_g \mathrm{e}^{-\omega^2 L_g^2/(4c_l^2)} \right]^2 . \tag{7.14}$$

This expression has zeros

$$\omega = 0 \quad \vee \quad \omega^2 = \frac{4c_l^2}{L_e^2 - L_g^2} \ln\left(\frac{D_e}{D_g}\right), \tag{7.15}$$

while the maxima are more cumbersome to determine analytically.

To attain a physical explanation for the appearance of these holes, we must remember origin of the deformation potential coupling as discussed in Section 2.2.1. In general a compression of a crystal increases the band gap [97]. For a number of III-V semiconductors including GaAs it has been demonstrated by first-principles calculations that the valence band and the conduction band actually are shifted the same way [98], but is is generally agreed that the conduction band is shifted faster with pressure, such that the bandgap is increased anyway [97]. This means that the sign of D_e and D_g is the same, which as we see from Eq. (7.15) is a requirement for the zeros to appear.

The wavefunction widths are related to the effective masses in the different bands. The effective mass in the conduction band is lowest, giving less confinement, and thus $L_e > L_g$. The zeros appear when the energy shift of each band and the effective masses are balancing each other. We use values of D_e and D_g which is widely used in the literature concerning electron-phonon interaction [43, 66, 99], but in general the values deviates much in the literature, see Appendix A for further information.

As we see from Eq. (7.14) and Fig. 7.2a, increasing the temperature does not change the width or shift the zeros of the spectrum, but only leads to an increase of the amplitude of the spectrum as discussed in Section 5.2.3. Thus when making plots of the effective phonon spectrum from now on, we will primarily consider $T = 0\,\mathrm{K}$, keeping this temperature scaling in mind.

In practice the wavefunction widths would depend on the material specific parameters and the QD geometry. By neglecting this fact and imagining that L_e and L_g may be varied freely, we plot the spectrum for $L_g = 4\,\mathrm{nm}$ and varying L_e. The spectrum is clearly largest when the lengths are the same, because the smallest QD dimensions gives the largest phonon interaction – the zeros lie at infinity for $L_e = L_g$, so they do not affect this statement. This case is, however, unrealistic due to the different mass of the electron and the hole. In agreement with Eq. (7.15), the position of the zeros moves toward $\omega = 0$ when the difference between L_e and L_g is increased. In the other limit the zeros for $L_e = L_g$, the zeros are at $\omega = \pm\infty$.

We wish to determine how this observed hole in the effective phonon spectrum affects the lifetime asymmetry as discussed in Chapter 5 and the indistinguishability from Chapter 6. The lifetimes are shown in Fig. 7.3a for varying L_e. The lifetime asymmetry follows the shape of the effective phonon spectrum in Fig. 7.2b, such that detuning exists where no asymmetry appears. At these detunings, properties of the electronic confinement described by $M^{\mathbf{k}}$ allows no

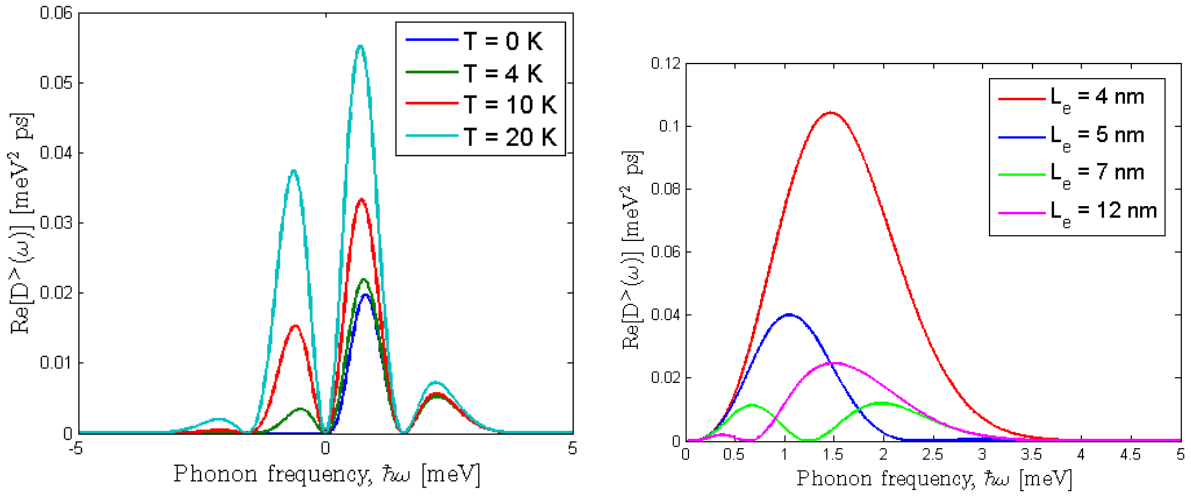

Figure 7.2: **(a)** Effective phonon spectrum plotted for different temperatures with $L_g = 4$ nm and $L_e = 6$ nm. **(b)** Effective phonon spectrum plotted for $T = 0$ K with $L_g = 4$ nm and different L_e. In practice due to the lower effective mass in the conduction band than in the valence band, $L_e > L_g$.

interaction between the electrons and the phonons, such that a phonon-assisted cavity-coupling is present.

The short-time effect of the pure dephasing on the indistinguishability is determined by the initial dynamics of $\mathrm{Re}\{\gamma_{12}(t)\}$. As discussed in Chapter 6, this effect can only be minimized by decreasing amplitude of the effective phonon spectrum. In Fig. 7.2b for the case with $L_e = 7\,\mathrm{nm}$, the hole appears where the function "should have peaked", giving a lower amplitude than for both $L_e = 5\,\mathrm{nm}$ and $L_e = 12\,\mathrm{nm}$. The time-evolution of $\mathrm{Re}\{\gamma_{12}(t)\}$ is plotted in Fig. 7.3b for different L_e, and the case $L_e = 7\,\mathrm{nm}$ clearly gives the lowest contribution from the short-time effect to the indistinguishability.

The long-time effect described by $\mathrm{Re}\{\gamma_{12}(\infty)\}$ in Fig. 7.3b follows the shape of the effective phonon spectrum as for the lifetime asymmetry, where the holes appear because the electronic confinement allows no transition to the cavity.

The full ellipsoidal model

Going back to the full ellipsoidal wavefuntion, assuming that $l_{e,xy} > l_{e,z}$ and $l_{g,xy} > l_{g,z}$, we show that Eq. (7.11) may be written as

$$\mathrm{Re}\{D^{>}(\omega)\} = \frac{\hbar}{4\pi d c_l^5}\frac{\omega^3}{1-\mathrm{e}^{-\beta\hbar\omega}}\Big[D_e^2\mathrm{e}^{-\omega^2 l_{e,xy}^2/(2c_l^2)}g_1(\omega) + D_g^2\mathrm{e}^{-\omega^2 l_{g,xy}^2/(2c_l^2)}g_2(\omega) - 2D_eD_g\mathrm{e}^{-\omega^2(l_{e,xy}^2+l_{g,xy}^2)/(4c_l^2)}g_3(\omega)\Big], \tag{7.16}$$

with

$$g_i(\omega) = \int_0^1 \mathrm{d}x\,\mathrm{e}^{\frac{\omega^2 b_i^2}{4c_l^2}x^2}, \tag{7.17}$$

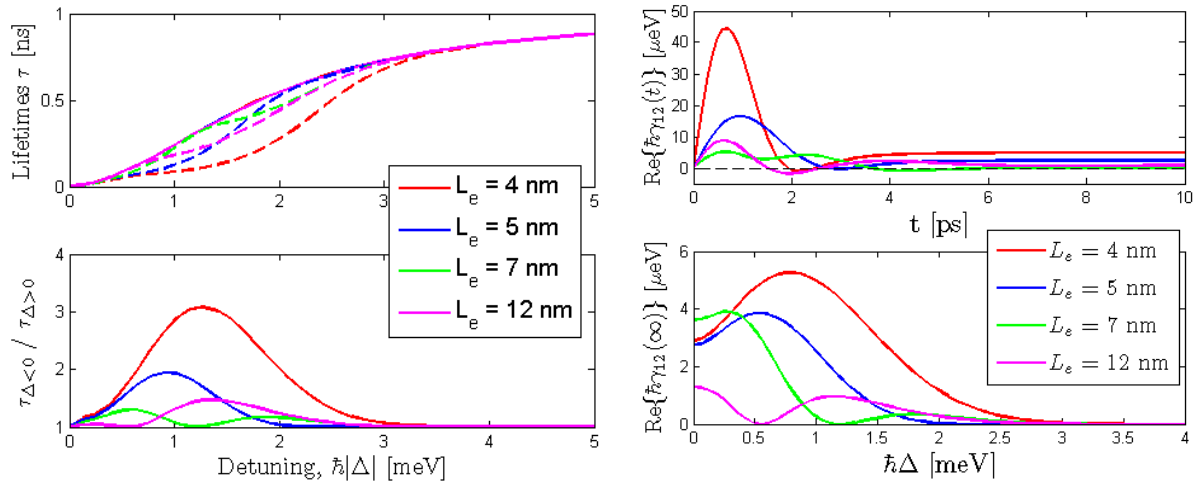

Figure 7.3: **(a)** (Top) Lifetimes of the excited QD state plotted versus the detuning for different values of L_e with $L_g = 4\,\text{nm}$, where solid (dashed) curves is for negative (positive) detunings. The solid lines are all coinciding, since the simulation is carried out at $T = 0\,\text{K}$, where the effective phonon spectrum is zero for negative frequencies. (Bottom) The degree of asymmetry defined as the ratio of the lifetime for opposite signs of the detuning. **(b)** (Top) The pure dephasing rate plotted vs. time for different L_e at $\Delta = 1\,\text{meV}$ with $L_g = 4\,\text{nm}$. (Bottom) The long-time pure dephasing rate plotted for varying detunings.

where

$$b_1 = \sqrt{2}\sqrt{l_{e,xy}^2 - l_{e,z}^2}, \quad b_2 = \sqrt{2}\sqrt{l_{g,xy}^2 - l_{g,z}^2}, \tag{7.18}$$

$$b_3 = \sqrt{l_{e,xy}^2 - l_{e,z}^2 + l_{g,xy}^2 - l_{g,z}^2} = \frac{\sqrt{b_1^2 + b_2^2}}{\sqrt{2}}. \tag{7.19}$$

Comparing Eq. (7.16) and Eq. (7.14) for the spherical wavefunction, we see that the form of the expression is the same as Eq. (7.14), where the only difference is the term in the square brackets. In the spherical dot limit, $l_{e,xy} \to l_{e,z}$ and $l_{g,xy} \to l_{g,z}$, then $g_i(\omega) \to 1$ and we obtain Eq. (7.14).

We now have four wavefunction widths to vary, so to get realistic values for these, we extract them from FEM-calculations of the QD wavefunction. This is done in the following section, where the effective phonon spectrum are also be plotted. As we shall see, the ellipsoidal wavefunction does not always lead to zeros as we saw in Fig. 7.2b, but a dip in the spectrum will still appear due to the minus-sign in square brackets in Eq. (7.16).

7.2 Wavefunction calculation using FEM

In this section we describe how the new effects discussed above appears in realistic QD structures where the wavefunction geometry is determined by the material parameters and by the QD shape. We consider a QD and a wetting layer of InAs and a surrounding barrier material of GaAs, see Appendix F for parameter values. We simulate the QD structure similar to the one in Fig. 7.1a by a truncated conical dot model as sketched in Fig. 7.4. The theory for determining the wavefunctions is treated in details in [100, 101, 102, 103].

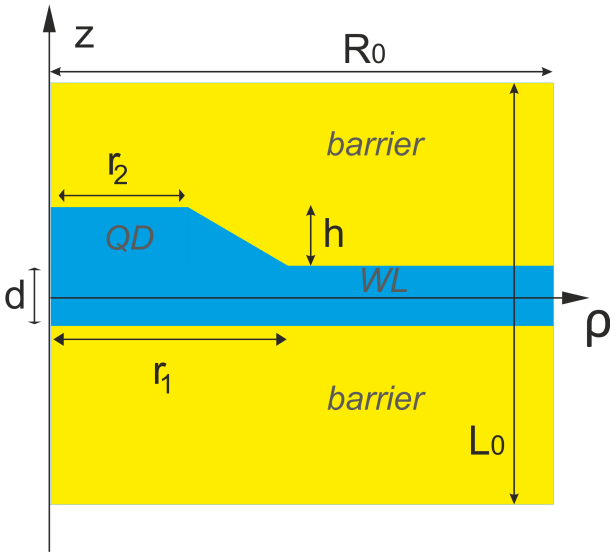

Figure 7.4: The model for the truncated conical QD on a wetting layer analyzed using COMSOL. When nothing else is mentioned, we use the size parameters $d = 0.2$ nm, $r_1 = 10$ nm, and $r_2 = 5$ nm which describes an experimentally realizable QD [37], where the wetting layer only consists of a few atom layers. The material parameters used in the simulation are given in Section A, and the calculation domain has the width R_0 and height L_0.

We describe the QD by a simple two-band model where only one conduction and valence band is considered, neglecting the spin of the electron as usually done in the literature. Furthermore we neglect effects of band mixing and strain in the material, except the fact that the QD was form by strain induced by different lattice constants of InAs and GaAs. In the envelope function approximation the full wavefunction is given by

$$\Phi(\mathbf{r}) = u(\mathbf{r})\Psi(\mathbf{r}) \tag{7.20}$$

where $u(\mathbf{r})$ is a Bloch function describing the periodic ion lattice (which we do not need to know in details), and $\Psi(\mathbf{r})$ is the envelope function. In this approximation the envelope function obeys the one-band Schrödinger equation,

$$-\boldsymbol{\nabla}\cdot\left(\frac{\hbar^2}{2m^*(\mathbf{r})}\boldsymbol{\nabla}\Psi(\mathbf{r})\right) + V(\mathbf{r})\Psi(\mathbf{r}) = E\Psi(\mathbf{r}) \tag{7.21}$$

where $m^*(\mathbf{r})$ is the position dependent effective mass of an electron moving in the confinement potential $V(\mathbf{r})$, which is created by band-bending effects due to the presence of a low-bandgap material surrounded by a barrier of a high-bandgap material. A detailed description of this is provided in Appendix F.

The wavefunction, $\Psi(\mathbf{r})$, has to be continuous and everywhere differentiable. At a discontinuity in $m^*(\mathbf{r})$, i.e. at the interface between the WL/QD and the barrier material, this gives two boundary conditions

- $\Psi(\mathbf{r})$ is continuous.
- $\frac{1}{m^*(\mathbf{r})}\mathbf{n}\cdot\boldsymbol{\nabla}\Psi(\mathbf{r})$ is continuous,

where $\mathbf{n}$ is a outer normal vector in the considered domain. Furthermore $\Psi(\mathbf{r})$ must be finite at all $\mathbf{r}$ to have a physical solution.

The QD has rotational symmetry around the z-direction, allowing us to use a cylindrical coordinate system and separate the wavefunction as

$$\Psi(\mathbf{r}) = \chi(\rho, z)\Phi(\phi) \tag{7.22}$$

By inserting this expression for $\Psi(\mathbf{r})$ into Eq. (7.21), the equation separates one part concerning $\chi(\rho, z)$ and one concerning $\Phi(\phi)$. By requiring that $\Phi(\phi)$ is single-valued, i.e. $\Phi(\phi) = \Phi(\phi + 2\pi)$, we get

$$\Psi(\mathbf{r}) = \chi(\rho, z)\mathrm{e}^{in\phi}, \tag{7.23}$$

where n is an integer. Using this, the equation for $\chi(\rho, z)$ becomes

$$\left[-\frac{\hbar}{2\rho}\frac{\partial}{\partial\rho}\left(\frac{\rho}{m^*}\frac{\partial}{\partial\rho}\right) - \frac{\hbar^2}{2}\frac{\partial}{\partial z}\left(\frac{1}{m^*}\frac{\partial}{\partial z}\right) + \frac{n^2\hbar^2}{2m^*\rho^2} + V(\rho, z)\right]\chi_n(\rho, z) = E\chi_n(\rho, z), \tag{7.24}$$

where $m^* = m^*(\rho, z)$. Different modes appear which we describe by an index on *chi*, indicating the mode number, n. We also see from Eq. (7.24) that the eigenvalue E is degenerate in n due to the rotational symmetry.

The boundary conditions for $\chi_n(\rho, z)$ may be obtained from Eq. (7.23): If $n = 0$ then Ψ does not vary with ϕ, giving the requirement that the gradient of $\chi_0(\rho, z)$ has to be the zero-vector for $\chi_0(\rho, z)$ to be differentiable, otherwise $\chi_0(\rho, z)$ has a ,,sharp corner" at $\rho = 0$. If $n \neq 0$ the requirement of continuity of Ψ at $\rho = 0$ implies $\chi_n(\rho = 0, z) = 0$ due to the oscillating variations in the radial direction.

The above mentioned boundary conditions arise from pure physical considerations. While doing FEM-calculations, we are limited to a finite domain with boundaries $z = \pm L_0/2$ and $\rho = R_0$ as sketched in Fig. 7.4. These artificial boundaries are defined to be able to solve the problem numerically, and we have to state boundary conditions for these too.

From basic quantum mechanics we know that a finite quantum well has sinusoidal solutions inside the well and exponentially decaying solutions outside [104, sec. 4.6]. Thus it is reasonable to assume that $\chi_n(\rho, \pm L_0/2) = 0$ if L_0 is large enough. By applying a boundary condition in the radial direction at R_0, this implies that the continuum of modes in the wetting layer is quantized. As $R_0 \to \infty$, the energy spacing of these discrete wetting layer modes become infinitely small, converging towards the mode continuum. For bound modes, i.e. modes that are confined to the dot, it is thus reasonable to used the boundary condition $\chi_n(\rho = R_0, z) = 0$ if we make sure to check that the solution has converged when increasing R_0.

Summarizing the boundary conditions, we have

- $\chi_n(\rho = 0, z) = 0$ for $n \neq 0$.
- $\partial_\rho\chi_n(\rho, z)|_{\rho=0} = 0$ for $n = 0$.
- $\chi_n(\rho, \pm L_0/2) = \chi_n(R_0, z) = 0$.

In our model we only consider a single conduction and valence band, corresponding to the fundamental state in each band described by $n = 0$, defined as the state with the lowest eigenenergy. If the structure only contained the WL and the barrier, this corresponds to the finite quantum well, which has an analytical solution. More complicated structures as the one including the QD

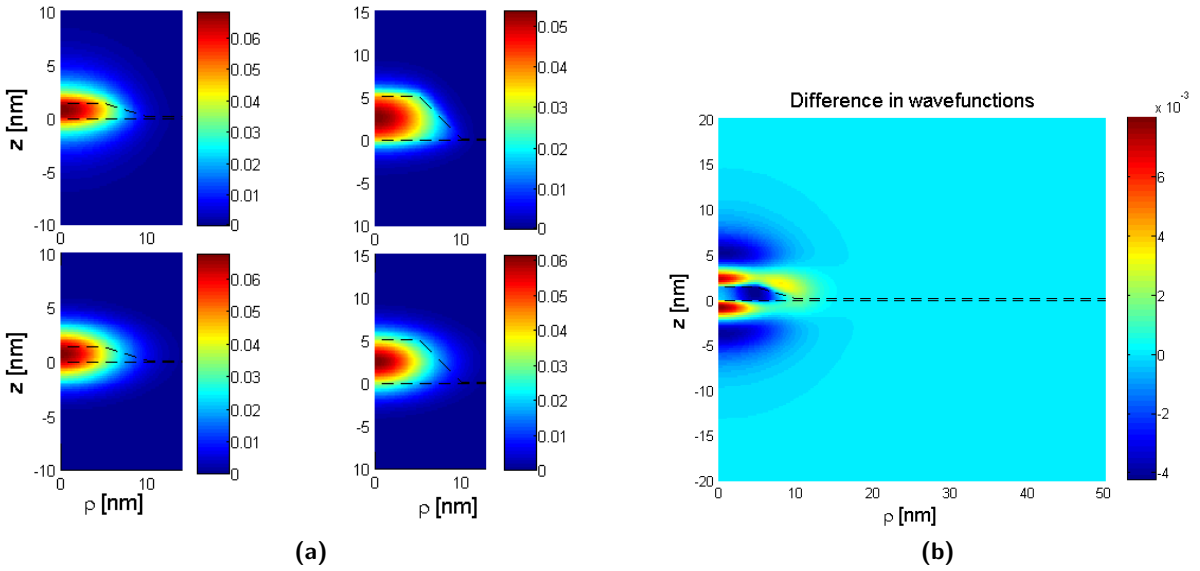

Figure 7.5: **(a)** Normalized wavefunctions in the QD described in Fig. 7.4 for $h = 1.25$ nm (left) and $h = 5.0$ nm (right). The upper pictures are the FEM wavefunction for an electron in the conduction band and the lower pictures are the fit to Eq. (7.25). **(b)** The absolute difference between the fit and the FEM wavefunction, $\phi_{\text{fit}} - \phi_{\text{FEM}}$, illustrated for the QD with $h = 1.25$ nm in Fig. 7.5a.

must be solved numerically. We implement the model in the finite element package COMSOL[1]. Eq. (7.24) has to be implemented in a normalized version, and a detailed description of the normalization is provided in Appendix F. In Appendix F we furthermore compare a numerical calculation of the energies of a finite quantum well with the analytical results to confirm, that the implementation is correct. As the last thing we verify solutions of the QD-problem have converged with respect to the used number of mesh points and R_0.

7.3 Truncated conical dot wavefunction

To calculate the wavefunctions by FEM, we use the parameters in Appendix F for the effective masses and bandgap energies. All plots are made for $T = 0\,\text{K}$ because we in Section 7.1 realized that the temperature only scales the spectrum, though a little asymmetrically. The wavefunctions are fitted using a two-dimensional fitting procedure to the ellipsoidal wavefunction,

$$\phi_\nu(\mathbf{r}) = a_4 \mathrm{e}^{-a_1\rho^2 - a_2(z-a_3)^2}, \tag{7.25}$$

where a_{1-4} are fitting parameters[2]. From a_1 and a_2 we may extract the effective lengths, and the center of the Gaussian we denote $(\rho, z) = (0, z_0)$, from which we see that $z_0 = a_3$.

An example of a wavefunction calculated with FEM is plotted in Fig. 7.5a where the wavefunction clearly is confined to the dot although part of the wavefunction lies outside the dot.

[1] For further details see `www.comsol.com`

[2] Requiring a normalized wavefunction fit, the parameter a_4 is determined by a_1 and a_2 in a three-parameter fit. We did however not have time to implement this succesfully in the fitting procedure, and instead we normalized the wavefunction after doing the four-parameter fitting. But as we will see, our approach gives good fits anyway.

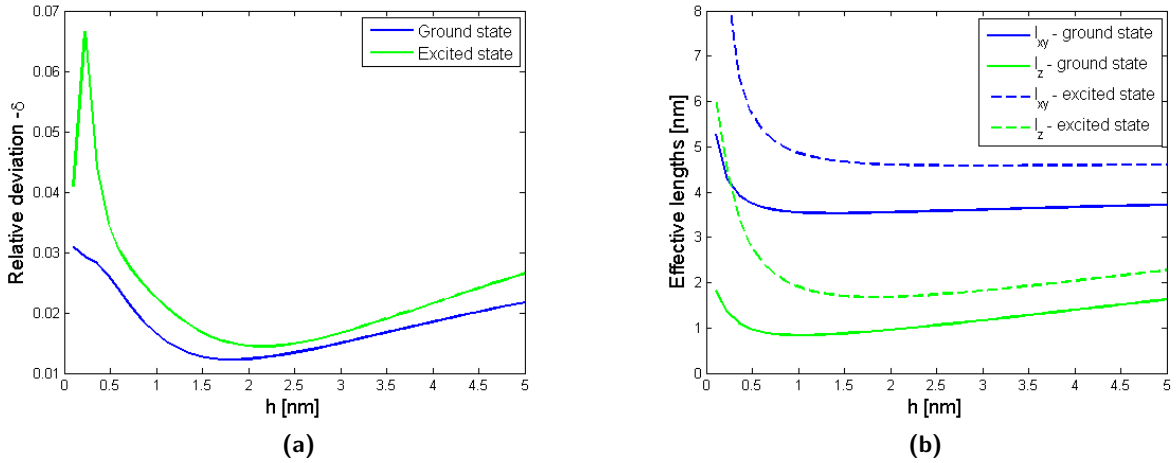

Figure 7.6: **(a)** The relative deviation δ between the COMSOL wavefunction and the ellipsoidal fit versus the QD height, h. **(b)** Effective widths of the ground and excited states in the radial direction (xy-direction) and in the z-direction versus h. The widths are extracted by an ellipsoidal fit to the FEM-wavefunction. We use the parameters $d = 0.2$ nm, $r_1 = 10$ nm, and $r_2 = 5$ nm.

The wavefunction fit is given in the lower part of the figure and the absolute difference between the fit and the COMSOL wavefunction is given in Fig. 7.5b.

As a measure of the deviation between the wavefunctions, we define the quantity

$$\delta = \frac{\int \mathrm{d}\mathbf{r}\, |\phi_{\mathrm{fit}}(\mathbf{r}) - \phi_{\mathrm{FEM}}(\mathbf{r})|^2}{\int \mathrm{d}\mathbf{r}\, |\phi_{\mathrm{FEM}}(\mathbf{r})|^2}. \tag{7.26}$$

We see that δ lies in the range $0 \leq \delta \leq 1$, where $\delta = 1$ corresponds to a perfectly matching fit. Both the FEM- and the fitted wavefunction are normalized making the denominator equal to 1.

Depending on how the dots is grown, the proportions of the QD may vary and thus change the wave functions. We calculate δ for QDs with different heights, see Fig. 7.6a. For our parameters there exists an optimal height at around $1.5 - 2$ nm. When the height is too small, the QD-wetting layer structure looks more like a finite quantum well. From general quantum mechanics it is known that the wavefunction in a finite quantum well has a sinusoidal shape inside the well and an exponential decay outside [104]. The large deviation between the calculated wavefunction and the fit for small values of h is simply a statement of the mismatch between this sinusoidal-exponential function and the Gaussian fit. In the large h-limit, the shape of the FEM wavefunction follow the shape of the dot, as seen in Fig. 7.5a, an thus deviates more from the symmetric, ellipsoidal model. But in general the fit is quite good and only deviates with 1-5 %.

From the fitting we may also extract the effective widths, see Fig. 7.6b. As expected, the wave function of the ground state has smaller width than the excited state, consisten with the higher confinement in the valence band due to the higher effective mass. As $h \to 0$, the setup becomes equal to the finite quantum well, where the electron is confined in the z-direction, but totally free to move in the x and y-direction giving infinite confinement lengths[3]. In the large h limit, the effective lengths scale with the shape parameters, i.e. l_z scales with $d + h$ (of course depending on the relationship between r_1 and r_2 also) and l_{xy} scales with a combination of r_1 and r_2, depending on their relative size. A rough estimate is to say that the effective length l_{xy} or l_z is half the size of the QD in that given direction, with the length of the excited state being a little larger than for the ground state. From Fig. 7.6b we have for a QD with $h = 4$ that $l_z \approx 1.5 - 2$ nm $\approx h/2$ and $l_{xy} \approx 4 - 5$ nm $\approx r_1$.

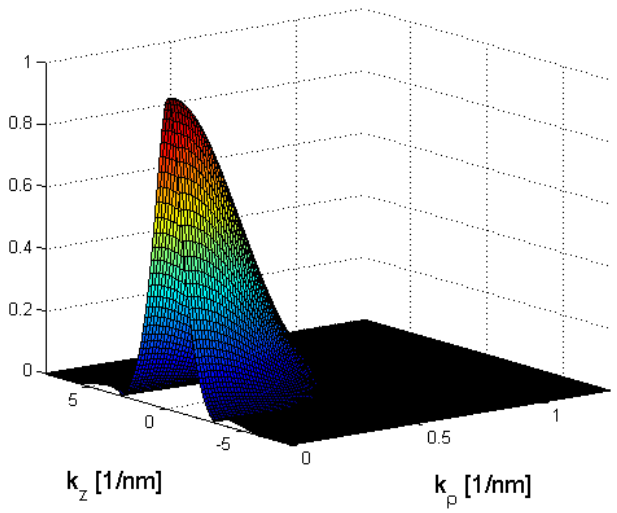

Figure 7.7: The form factor of the conduction band FEM wavefunction in k-space for $h = 3$ nm, defined as the Fourier transform of $|\phi(\mathbf{r})|^2$, see Eq. (7.2). It is described in cylindrical coordinates by an in-plane wavevector of length k_ρ and an axial wavevector k_z. The value at $k_\rho = k_z = 0$ is 1, showing that the FEM wavefunction is normalized, and furthermore we confirm that our calculation domain in k-space is reasonably large.

The effective phonon spectrum

The calculated FEM wavefunctions are calculated in the two-dimensional (ρ, z)-plane, and with these the interaction matrix elements may be calculated from Eq. (7.2). These contain the Fourier transform of the wavefunction, see Fig. 7.7. When calculating interaction matrix element from Eq. (7.2), we must integrate over the three-dimensional $\mathbf{k}$-space where the angular dependence is included. By carrying out the angular integration, we arrive at

$$\int \mathrm{d}\mathbf{r}\, |\phi_\nu(\mathbf{r})|^2 \mathrm{e}^{\mathrm{i}\mathbf{k}\cdot\mathbf{r}} = 2\pi \int_{-\infty}^{\infty} \mathrm{d}z \int_0^{\infty} \mathrm{d}\rho\, \rho |\phi_\nu(\rho, z)|^2 J_0(k_\rho \rho) \mathrm{e}^{\mathrm{i}k_z z}. \tag{7.27}$$

[3]When the heights of the dot becomes comparable with the thickness of the wetting layer and the modes becomes unconfined, an error occurs due to the boundary condition at $\rho = R_0$, requiring the wavefunction to be zero. We operate with heights $h \gg d$, so this is not an issue

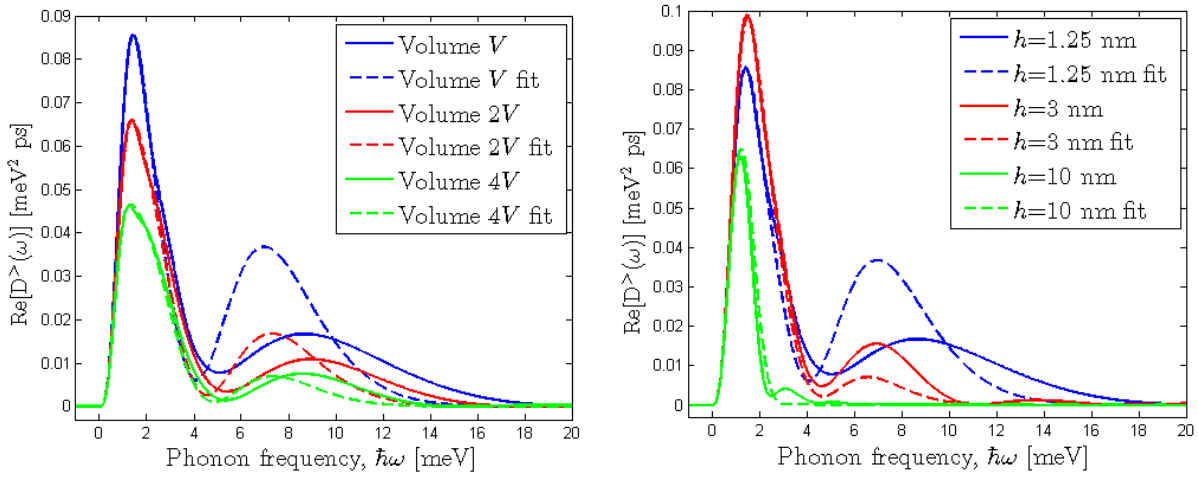

Figure 7.8: **(a)** The effective phonon spectrum plotted for different QD volumes for the FEM-wavefunction and the ellipsoidal fit. The volume V corresponds to a QD of height h, and all sizes in the QD are scaled equally. All size parameters are scaled with the same amount, having $h = 1.25$ nm at the volume V. **(b)** Same as in (a), but where h is varied, keeping all other parameters constant.

From the Fourier transform of the phonon bath correlation function we obtain the effective phonon spectrum. This we evaluate for varying volumes, corresponding to scaling all sides of the QD equally, and we vary only the QD height, changing the shape of the QD, see Figs. 7.8a and 7.8b. At first we notice that the well accounts for dynamics at small detunings $0-4$ meV, but gives deviations for larger detunings due to the deviations of the fit from the FEM wavefunction as shown in Figs. 7.5b and 7.6a.

For $h = 3$ nm we observe several oscillations in the spectrum which is not apparent in the ellipsoidal model. A possible explanation for the oscillations may be achieved by mathematical considerations: If we assume a rectangular (in 3d a disk-shape), constant wavefunction on the form $\phi(\rho, z) = K\theta(\rho_0 - |\rho|)\theta(z_0 - |z|)$ with θ being the Heaviside step function and ρ_0 and z_0 dot parameters, the resulting effective phonon spectrum may be shown to contain Bessel-functions in ρ and z, giving decaying oscillations for large frequencies in the spectrum like the ones we see in Fig. 7.8b. Even though the rectangular wavefunction is clearly unphysical, it may explain that oscillations occur in the effective phonon spectrum when FEM wavefunction has sharp edges and deviates from the ellipsoidal shape.

In Fig. 7.8a an increased volume increases the spatial extend of the wavefunction and decreases the electron-phonon interaction, as previously discussed. When varying h in Fig. 7.8b, we also observe that for the large dot, the amplitude of the spectrum is lowest. But the QD with $h = 3$ nm gives a higher spectrum amplitude than for $h = 1.25$ nm. The wavefunction for $h = 1.25$ nm extends quite much into the barrier material as shown in Fig. 7.5a. We understand the higher amplitude for $h = 3$ nm as the fact the when increasing the height a little from $h = 1.25$ nm, the wavefunction actually becomes better confined because less of the wavefunction is in the barrier material. Thus the phonon dynamics is only changed slight, even though the QD height is varied significantly, from $h = 1.25 - 3$ nm.

In general we observe that a dip (but no zero as for the spherical wavefunction) appears

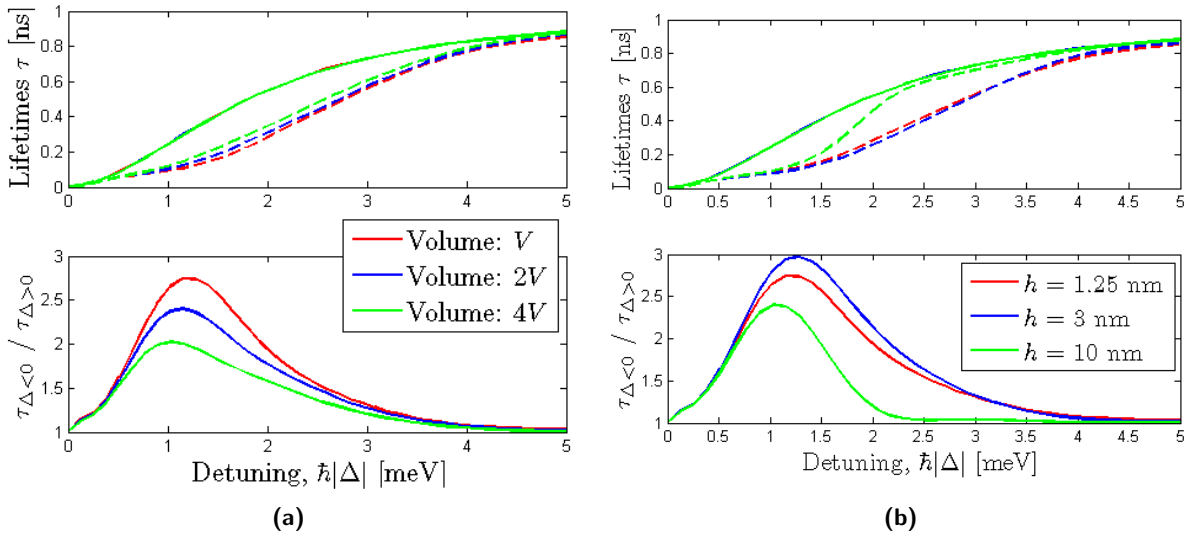

Figure 7.9: **(a)** (Top) Lifetimes of the excited QD state plotted versus the detuning for different QD volumes, where solid (dashed) curves is for negative (positive) detunings. The solid lines are all coinciding, since the simulation is carried out at $T = 0\,\mathrm{K}$, where the effective phonon spectrum is zero for negative frequencies. (Bottom) The degree of asymmetry defined as the ratio of the lifetime for opposite signs of the detuning. **(b)** Same as in (a), but for different QD heights.

in the spectrum, as predicted by the theory from Section 7.1. The position of the hole is though not changed much when varying the QD shape, due to the mutual dependence of the wavefunction widths. The energy range of the effective phonon spectrum is larger than for the preciously considered analytical cases. Here, the wavefunction widths were around $4-6\,\mathrm{nm}$, but the widths extracted from the FEM-calculations are much smaller, see Fig. 7.6b. As discussed below Eq. (5.20), the width of effective phonon spectrum is approximately proportional to L^{-1} for the crude wavefunction. The low widths due to the confinement in the QD growth direction $\sim 1-2\,\mathrm{nm}$ results in a wide energy span, containing a dip around $5\,\mathrm{meV}$.

Lifetime asymmetry and indistinguishability

To determine the effect of realistic wavefunctions on the lifetime, we consider the lifetime asymmetry for varying volume and h, see Figs. 7.9a and 7.9b. As expected, increasing the QD size gives lower effect of the electron-phonon interaction. The dips in the effective phonon spectrum, however, appears at around $5\,\mathrm{meV}$ at too high energies to affect the asymmetry. Only at $h = 10\,\mathrm{nm}$ where l_z is larger, the dip introduces a lower asymmetry. Due to the nearly similar wavefunctions for $h = 1.25\,\mathrm{nm}$ and $h = 3\,\mathrm{nm}$, the asymmetry is almost similar.

Compared to the crude wavefunction approach in Fig. 5.8b, the effect on the lifetime asymmetry is the same; a larger dot gives lower asymmetry. A little effect of the dips are though seen for $h = 10\,\mathrm{nm}$ in Fig. 7.9b, where the detuning range is decreased. It is difficult compare these cases quantitatively, since the width of the crude wavefunction, L, is an unphysical quantity and thus is difficult to ascribe a reasonable value to.

For the indistinguishability we neither see any qualitatively different behaviour of the pure dephasing rate in Figs. 7.10a and 7.10b compared to the crude wavefunction approach Figs. 6.1a

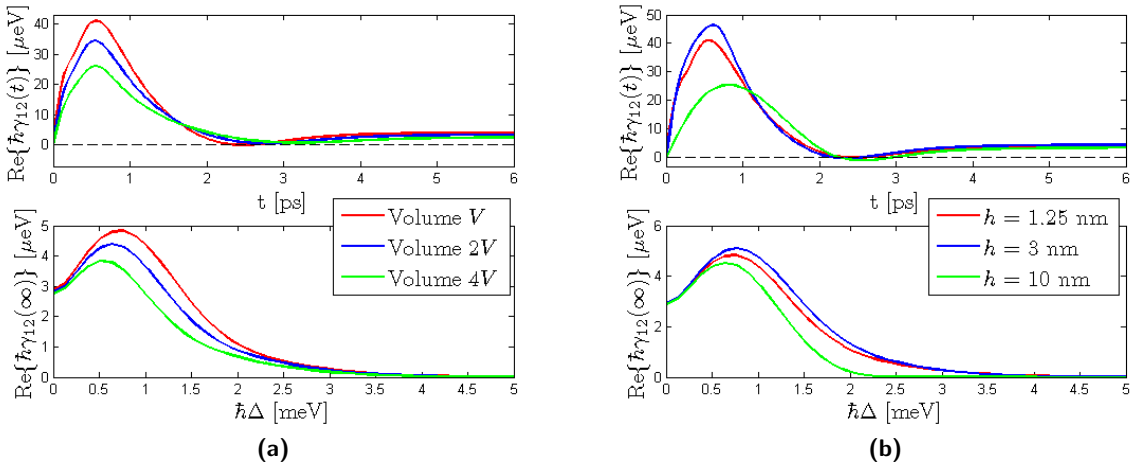

Figure 7.10: **(a)** (Top) The pure dephasing rate plotted vs. time for different QD volume at $T = 0\,\mathrm{K}$. (Bottom) The long-time pure dephasing rate plotted for varying QD volumes. **(b)** Same as in (a), but for different QD heights.

and 6.2b, because the dip appears at too high phonon energies. The pure dephasing rate almost is the same in the case of $h = 1.25\,\mathrm{nm}$ and $h = 3\,\mathrm{nm}$ due to the almost similar wavefunctions.

7.4 Summary and discussion

In this chapter we have demonstrated how the electronic confinement in the QD may alter the electron-phonon coupling properties. We expanded the crude wavefunction approach to an ellipsoidal model, which takes into account the possibility of different wavefunction widths in the growth and in-plane directions and includes different effective masses of the valence and conduction band.

In the spherical limit of the ellipsoidal approach, we demonstrate that for materials with the same sign of the deformation potential constants, D_e and D_g, zeros appears in the effective phonon spectrum at non-zero phonon frequencies. These appear when D_e and D_g are balancing the asymmetry of the wavefunctions caused by the difference in effective masses in the valence and conduction band. This has, to our knowledge, not have been observed before. We demonstrated how these zeros could be used to minimize both the lifetime asymmetry and the pure dephasing from the phonons. For the full ellipsoidal model, zeros are only achieved in the spherical limit, but dips still appear in the effective phonon spectrum.

To test how well the ellipsoidal fit matches the wavefunction in a realistic QD structure, we determine the wavefunction of a truncated conical quantum dot by FEM calculations and compare this to an ellipsoidal wavefunction fit. The fit is best for shallow but not too shallow quantum dots, and we are able to extract wavefunction widths. The resulting phonon spectra are wider than for the crude wavefunction since the extracted wavefunction widths are smaller.

A quantitative comparison of the results from the crude and from the FEM wavefunction will be misleading, since we do not have any physical reasonable value for L, because it describes an unphysical wavefunction. Although we will try to qualitatively point out the similarities

and differences between the crude wavefunction with $L = 4\,\text{nm}$ and the truncated conical dot structure which is considered. Both of these resolve the large peak around a phonon energy of $0 - 5\,\text{meV}$ in the effective phonon spectrum, but the FEM-spectrum differ by having a non-zero value up to $\sim 18\,\text{meV}$, where the spectrum for the crude model is zero.

Recalling from the expression for the total decay rate of the excited QD state derived in Eq. (5.17) in the limit $\Delta \gg g$, the phonon contribution depends on the value of the effective phonon spectrum evaluated in $\omega = \Delta$. The same applies for the long-time phonon-induced pure dephasing rate in Eq. (6.20), which depend on the values at $\pm\sqrt{\Delta^2 + 4g^2}$. The reason why no qualitatively different behaviour in the lifetime asymmetry and in the long-time pure dephasing rate is seen, is because the dip in the FEM-spectrum appears at so high detuning, compared to the losses in the system, that no acoustic phonons with these energies exist to assist the coupling to the cavity.

For the short-time pure dephasing rate, which depends on the magnitude of the whole effective phonon spectrum and not just specific values, we expect that the non-zero part of the FEM-effective phonon spectrum at $5 - 20\,\text{meV}$ introduce a higher rate than expected from the crude wavefunction. This is though difficult to verify due to the inaccuracy in making a quantitative comparison.

Both the crude and ellipsoidal wavefunction do not resolve the high-energy values of the effective phonon spectrum properly, so when considering pure dephasing effects due to phonos, these wavefunction approximations are not sufficient. If the losses in some way could be minimized, the lifetime would decrease slower when Δ is increased, and the cavity-coupling would have more influence on the decay rate. In that case the dips in the effective phonon spectrum would begin to have influence on both the lifetime asymmetry and the long-time dephasing at those high detunings.

We experimented with a FEM-calculation of the wavefunction in the half-ellipsoidal QD shown in Fig. 7.1b also, but we did not gain any new physical insight, so we did not include it here, see Appendix G for details. Using other semiconductor materials for the QD would result in different deformation potentials and effective masses (and thus different wavefunction widths). By examining this in details, one might be able to find a combination, where the dip appears at lower phonon energies, such that the dephasing effects from the phonons could be minimized where the decay rate of the QD is still large, giving an optimal configuration for high indistingusihability in a single-photon source. The configurations in this thesis do however not propose any good solutions other than pumping at zero detuning, where the long-time detuning is zero and the QD decay rate is large due to the large Purcell-factor, even though it is not assisted by phonon-cavity feeding.

Chapter 8

Engineering the Phononic Confinement - Phonons in an Infinite Slab

The confinement of phonons in a quantum system is always finite due to the finite extend of the experimental sample, and the approximations about bulk phonons may not be valid. For a QD inside a photonic crystal cavity slab as in Fig. 1.2c, taken as an example, the phonons are are confined in one direction by the slab and in the other two by the holey structure. The finite confinement discretize the phonon modes and introduces new kind of phonons that behave differently than the bulk phonons.

Designs of materials with a so-called phononic band gap, in which mechanical excitations are forbidden in a range of frequencies, have been proposed and tested for different geometries [105]. By introducing a defect in these structures, a mechanical cavity appears where only vibrational modes with specific frequencies may exist. Demonstrations of materials with simultaneous photonic and phononic bandgaps have been shown recently [106, 107], and by designing these structures properly, an optomechanical cavity appears, in which the coupling between the vibrational mode and the light is enhanced [108, 109].

We consider the possibility of exploiting the structural confinement to minimize the effects of phonons instead of trying to exploit the phonon modes. To understand the complicated phonon mode structure in e.g. a photonic crystal cavity slab, it is important first to examine the case where the phonons are confined in one direction, namely the infinite slab. To our knowledge, this has not yet been dealt with in the literature in relation to coupling to an optical cavity. Several articles consider two coupled QDs in a slab instead of a coupled QD-cavity system [110, 111, 112, 113]. In these articles, the equivalence to the QD-cavity coupling parameter g is the transition rate between excited states in the two QDs, which depends on the mutual positions in the slab, but the Hamiltonians have similar structures. Physically the two systems differ in a couple of ways: Due to the spatial separation of the electron wavefunctions in the double-QD-system, the piezo-electric coupling may no longer be neglected. Furthermore the Purcell effect appears in the QD-cavity system, and not directly in the double QD-system[1]. At last, the coupling to acoustic phonons in the two systems is significantly different when coupling to two dots compared to a single dot.

[1]The Purcell-effect may be imitated in the double QD structure by assigning the loss rate κ as an extra non-radiative decay rate to one of the dots. The effect is though more easily addressed in a coupled QD-cavity system.

In Section 8.1 we describe the phonon modes that appear in a slab, based on discussions on the fundamental properties of phonon modes in a slab is found in many textbooks and articles, see e.g. [114, 115]. The deformation potential interaction between electrons in a bare QD (without any optical cavity) and acoustical phonons in a slab is described in [116, 117, 118]. In Section 8.2 we examine how the confinement of the phonons in a slab influence the dynamics of a coupled QD-cavity system in the slab.

8.1 Phonon modes in a slab

We will briefly discuss the different phonons modes that exist in a slab of thickness d with plane surfaces at $z = \pm d/2$. In an isotropic elastic continuum the ion displacement at a position $\mathbf{r}$ at a time t is described by $\mathbf{u}(\mathbf{r}, t)$ which obeys the wave equation [117],

$$\frac{\partial^2 \mathbf{u}}{\partial t^2} = c_t^2 \nabla^2 \mathbf{u} + (c_l^2 - c_t^2)\boldsymbol{\nabla}(\boldsymbol{\nabla} \cdot \mathbf{u}), \tag{8.1}$$

where c_t and c_l are the velocity of the transverse and longitudinal sound waves in bulk semiconductors, respectively. These are determined from the so-called Lamé constants and obey $c_l > c_t$.

The boundary conditions to Eq. (8.1) stem from the assumption of a *free-standing* slab, requiring that the normal components of the stress tensor vanish. The direction perpendicular to the slab is the z-direction, meaning that the boundary conditions may be expressed as $\sigma_{x,z} = \sigma_{y,z} = \sigma_{z,z} = 0$ at $z = \pm d/2$, using the definition of the stress tensor as given in Eq. (2.54). This gives three partial differential equations for the three spatial components of $\mathbf{u}$, and these equations constitute the boundary conditions.

A guess for a solution to Eq. (8.1) with the described boundary conditions is

$$\mathbf{u}(\mathbf{r}, t) = \sum_n \int \mathbf{u}_n(\mathbf{k}_\parallel, z) \mathrm{e}^{\mathrm{i}\mathbf{k}_\parallel \cdot \mathbf{r}_\parallel - \mathrm{i}\omega_n t} \frac{\mathrm{d}\mathbf{k}_\parallel}{(2\pi)^2}, \tag{8.2}$$

where the phonons are described by a continuum of plane waves in the in-plane directions and by discrete set of eigenmodes $\mathbf{u}_n(\mathbf{k}_\parallel, z)$ in the z-direction depending on the in-plane wavevector, $\mathbf{k}_\parallel$.

By inserting Eq. (8.2) in Eq. (8.1) and applying the boundary conditions, the eigenmodes $\mathbf{u}_n$ and phonon dispersion relation ω_n may be calculated for all modes and a solution is determined. In [117] it is shown that the guess Eq. (8.2) describes a complete set of modes, which may be divided into three confined acoustic modes, characterized by their symmetry properties: Shear waves, dilatational waves, and flexural waves [116]. In the following we describe the calculations of [116], and without loss of generalisation, we align the x-axis parallel to $\mathbf{k}_\parallel$, $\mathbf{k}_\parallel = (k_x, 0)$.

Shear waves

Shear waves have only one non-zero component perpendicular to the propagation direction of the wave, where the eigenmodes are given by $\mathbf{u}(\mathbf{k}_\parallel, z) = (0, u_y, 0)$ with

$$u_y = \begin{cases} \cos(k_{z,n}) & \text{if } n = 0, 2, 4, ... \\ \sin(k_{z,n}) & \text{if } n = 1, 3, 5, ... \end{cases}, \tag{8.3}$$

with $k_{z,n} = (\pi n/d)$. The dispersion relation of the shear waves is

$$\omega_n = c_t \sqrt{k_{z,n}^2 + k_x^2}. \tag{8.4}$$

The shear modes are behaving similarly to transverse modes in semiconductors and are quantified such that an integer number of half-wavelengths fit into the slab.

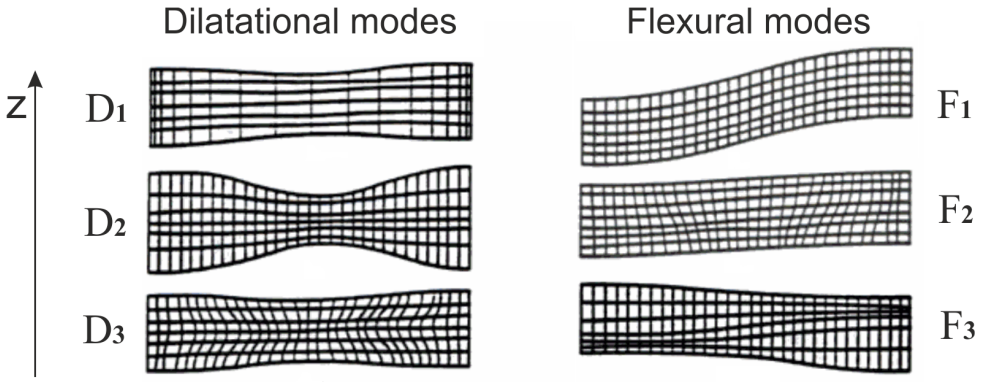

Figure 8.1: Grid diagrams for the three lowest-order dilatational (symmetric) and flexural (anti-symmetric) modes. After [119].

Dilatational waves

Dilatational waves are symmetric with respect to the center plane of the slab at $z = 0$, see Fig. 8.1, and are characterized by two non-zero components, $\mathbf{u}_n(\mathbf{k}_\parallel, z) = (u_x, 0, u_z)$ with

$$u_x = \mathrm{i}k_x \left[(k_x^2 - k_t^2)\sin(k_t d/2)\cos(k_l z) + 2k_l k_t \sin(k_l d/2)\cos(k_t z)\right], \tag{8.5}$$

$$u_z = k_l \left[-(k_x^2 - k_t^2)\sin(k_t d/2)\sin(k_l z) + 2k_x^2 \sin(k_l d/2)\sin(k_t z)\right]. \tag{8.6}$$

The parameters k_t and k_l has to be determined from the two coupled equations,

$$\frac{\tan(k_t d/2)}{\tan(k_l d/2)} = -\frac{4k_x^2 k_l k_t}{(k_x^2 - k_t^2)^2} \quad \text{and} \quad c_l^2(k_x^2 + k_l^2) = c_t^2(k_x^2 + k_t^2). \tag{8.7}$$

To solve Eq. (8.7) a numerical approach has to be done[2]. For a certain value of k_x, Eq. (8.7) has multiple solutions, and we label k_t and k_l by an additional index, $k_{t,n}$ and $k_{l,n}$. These parameters describes different types of solutions depending on if they are real or purely imaginary. Three possible combinations exists for Eq. (8.7) to have solutions: k_l and k_t are both real, k_l and k_t are both purely imaginary, and k_l is purely imaginary and k_t is real. Thus Eqs. (8.5) and (8.6) describes modes containing $\cos(|k_{l/t}|z)$ and $\sin(|k_{l/t}|z)$ that are extended through the width of the slab and phonon modes containing $\cos(\mathrm{i}|k_{l/t}|z) = \cosh(|k_{l/t}|z)$ and $\sinh(|k_{l/t}|z)$ that are confined to the surface and decay exponentially into the slab.

From k_l and k_t the dispersion relation may be found as

$$\omega_n = c_t \sqrt{k_x^2 + k_{t,n}^2} = c_l \sqrt{k_x^2 + k_{l,n}^2}. \tag{8.8}$$

[2]Numerically it may be an advantage first to determine the solutions of Eq. (8.7) for $k_x = 0$, and then use this result to determine the total solution. These may be determined straightforward by an analytical approach.

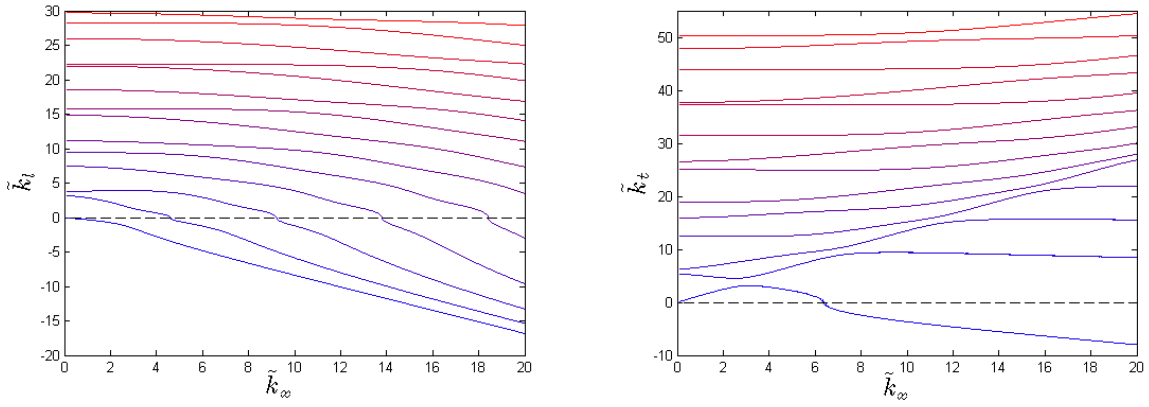

Figure 8.2: **(a)** The solution parameter k_l normalized to the slab thickness, $\tilde{k}_l = k_l d$, plotted as a function of the in-plane wave vector for the first 14 modes. Values above the abscissa correspond to real values of $\tilde{k}_l$, values below to imaginary values of $\tilde{k}_l$. **(b)** The normalized solution parameter $\tilde{k}_t$ plotted as a function of the in-plane wave vector similar to (a).

As in [116], the index n defines the branch number, where a branch is defined as a continuous single-connected curve of the solution functions $k_{t,n}(k_x)$ and $k_{l,n}(k_x)$. The „lowest" branch is denoted by $n = 1$ and indicates the branch in the dispersion relation with the lowest energy.

Eq. (8.7) may advantageously be solved by introducing the normalized, unit-less parameters $\tilde{k}_x = k_x d$, $\tilde{k}_l = k_l d$, $\tilde{k}_t = k_t d$ and $\tilde{\omega}_n = \omega_n d/c_l$. A plot of the solutions to Eq. (8.7) is given in Figs. 8.2a and 8.2b[3] with $c_l = 5.11\,\mathrm{km/s}$ and $c_t = 3.02\,\mathrm{km/s}$. Note that the solutions only depend on the material parameters as the ratio c_l/c_t, whereas the dispersion relation Eq. (8.8) depends on c_t or c_l specifically.

By comparing Eq. (8.8) to the bulk phonon dispersion relation $\omega = c_{\mathrm{eff}}|k|$, we see that because k_t and k_l may be purely imaginary, there exist effective phonon velocities, c_{eff}, that may be lower than both c_l and c_t. Considered the other way around, we may charaterize modes with $c_{\mathrm{eff}} < c_t$ as modes, that have purely imaginary k_l and k_t and thus are confined to the surface, whereas phonon modes with $c_{\mathrm{eff}} > c_l$ are modes extended through the slab. Modes with $c_t < c_{\mathrm{eff}} < c_l$ are a mix of the two.

The dispersion relation in Eq. (8.8) is plotted in Fig. 8.3a. For small k_x the lowest dilatational mode has a linear dispersion relation. From the dispersion relation, the phonon density of states (DOS) may be calculated as

$$\rho(\omega) = \sum_{k_x,n} \delta(\omega - \omega_n(k_x)) \tag{8.9}$$

$$\propto \sum_n \int_0^\infty \mathrm{d}k_x\, k_x \delta(\omega - \omega_n(k_x)) \tag{8.10}$$

$$= \sum_n k_x \left(\frac{\mathrm{d}\omega_n(k_x)}{\mathrm{d}k_x}\right)^{-1}\Bigg|_{\omega=\omega_n(k_x)} \theta\Big(\omega - \omega_n(k_x = 0)\Big), \tag{8.11}$$

[3]These plots agree with the plots provided in [116] where slightly different values of c_l and c_t are used.

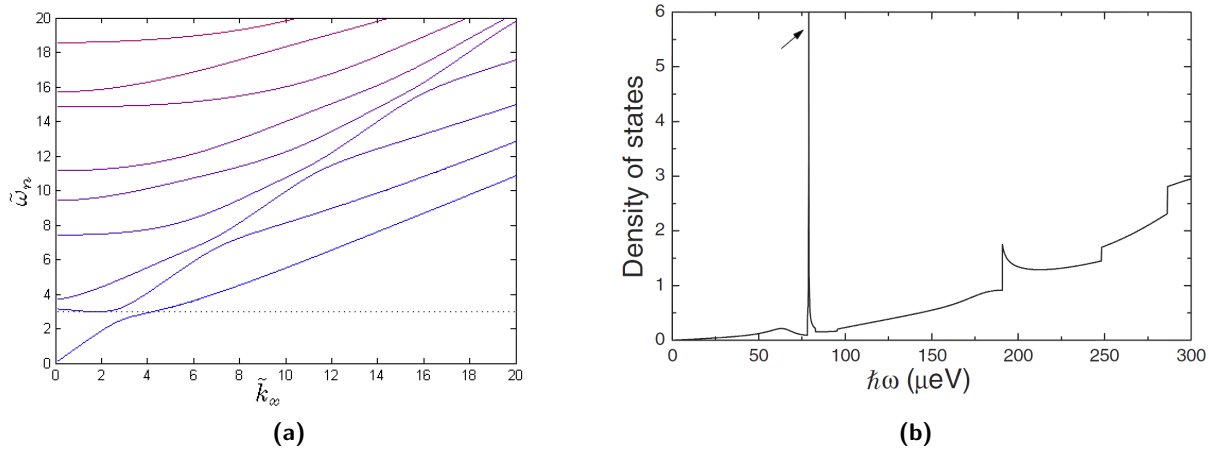

(a) (b)

Figure 8.3: **(a)** Phonon dispersion relation for dilatational waves: Normalized frequency $\tilde{\omega}_n$ plotted versus the normalized in-plane wavevector $\tilde{k}_x = k_x d$. The black dotted line indicates the value of $\tilde{\omega}_n = \omega d/c_l = 2.98$, where the second band has a minimum. **(b)** Phonon DOS plotted from Eq. (8.11) for a slab with $d = 130\,\text{nm}$. The arrow indicates the van-Hove singularity corresponding to frequency value of the minimum value of the second band in the dispersion relation in (a). Plot is taken from [120].

where $\theta(\omega)$ is the Heaviside step function. The phonon DOS is plotted in Fig. 8.3b[4], where higher order branches of the dispersion relation contributes as the frequency increases. The second branch of the dispersion relation has a very noticeable behaviour because it is the only branch with a minimum, marked with a black dotted line in Fig. 8.3a. Due to this minimum, the DOS in Eq. (8.11) is infinite at $\tilde{\omega}_n = \omega d/c_l = 2.98$ (extracted from Fig. 8.3a), where a resonance in the slab appears for the dilatational modes. Note that the value of $\tilde{\omega}$ where the minimum appears, only depend on the relation c_l/c_t, not on the thickness of the slab.

Flexural waves

Flexural waves are antisymmetric with respect to the center plane of the slab, see Fig. 8.1, and are also characterized by two non-zero components, $\mathbf{u}_n(\mathbf{k}_\parallel, z) = (u_x, 0, u_z)$ with

$$u_x = \mathrm{i}k_x \left[(k_x^2 - k_t^2)\cos(k_t d/2)\sin(k_l z) + 2k_l k_t \cos(k_l d/2)\sin(k_t z)\right], \tag{8.12}$$

$$u_z = k_l \left[(k_x^2 - k_t^2)\cos(k_t d/2)\cos(k_l z) - 2k_x^2 \cos(k_l d/2)\cos(k_t z)\right]. \tag{8.13}$$

where k_t and k_l are determined from

$$\frac{\tan(k_l d/2)}{\tan(k_t d/2)} = -\frac{4k_x^2 k_l k_t}{(k_x^2 - k_t^2)^2} \quad \text{and} \quad c_l^2(k_x^2 + k_l^2) = c_t^2(k_x^2 + k_t^2). \tag{8.14}$$

The flexural waves obey the same dispersion relation as the dilatational waves, Eq. (8.8), remembering that the values of $k_{t,n}$ and $k_{l,n}$ are different. We will not describe the flexural modes in details, see e.g. [116] for more information.

[4]We borrowed a plot from [120], since uncertainties from solving Eq. (8.7) numerically carried on and gave difficulties in determining $\mathrm{d}\omega_n/\mathrm{d}k_x$, which we did not have time to solve and thus to make the plot ourselves. We point out that this does not introduce errors in our calculation of the effective phonon spectrum, since it does not depend on the evaluation of $\mathrm{d}\omega_n/\mathrm{d}k_x$.

8.2 Electron-phonon interaction in the slab

As described in [118], the electron-phonon interaction matrix element for the deformation potential interaction from Section 2.2.1 may in general be written as

$$M_{n,\nu\nu} = D_\nu \mathcal{G}_n \mathcal{F}_{n,\nu}, \tag{8.15}$$

where D_ν is the deformation potential of the electron/hole, and $\mathcal{G}_n$ contains the dispersion relation of the phonon mode n, ω_n. The last factor $\mathcal{F}_{n,\nu}$ is equivalent to the form factor in Eq. (2.60) and contains the electronic wavefunction and thus represents the confinement of the electrons. For the bulk-phonon case, the expression for $\mathcal{F}_{n,\nu}$ and $\mathcal{G}_n$ has a simple form as in Eq. (2.61). In the slab case they becomes more complicated, as we will see, where the dynamics is determined from the calculated functions $\tilde{k}_{l,n}(\tilde{k}_x)$, $\tilde{k}_{t,n}(\tilde{k}_x)$, and $\tilde{\omega}_n(\tilde{k}_x)$.

As described in Section 2.2.1, the interaction between electrons and acoustical phonons through the deformation potential is governed by a Hamiltonian containing $\boldsymbol{\nabla}\cdot\mathbf{u}$ where $\mathbf{u}$ is the ion displacement given by Eq. (8.2). For the shear waves, $\boldsymbol{\nabla}\cdot\mathbf{u} = 0$, meaning that shear acoustic modes do not interact with the electrons. This is due to the fact that shear phonons remind of transverse phonons in bulk isotropic solids where they do not contribute to the deformation potential interaction [120].

Both the dilatational and the flexural modes contribute to the interaction Hamiltonian. The form factors of the two modes are

$$\mathcal{F}_{n,\nu,\mathrm{dil}} = \int_{\mathrm{slab}} \mathrm{d}\mathbf{r}\, |\phi_\nu(\mathbf{r})|^2 \mathrm{e}^{\mathrm{i}\mathbf{k}_\parallel\cdot\mathbf{r}_\parallel} \cos(k_{l,n} z), \tag{8.16}$$

$$\mathcal{F}_{n,\nu,\mathrm{flex}} = \int_{\mathrm{slab}} \mathrm{d}\mathbf{r}\, |\phi_\nu(\mathbf{r})|^2 \mathrm{e}^{\mathrm{i}\mathbf{k}_\parallel\cdot\mathbf{r}_\parallel} \sin(k_{l,n} z). \tag{8.17}$$

For simplicity we consider the carrier wavefunctions to be symmetric functions (like Gaussians as we used earlier) having their centers at $z = 0$ in the middle of the slab. In this case, the integral in $\mathcal{F}_{n,\nu,\mathrm{flex}}$ over the z-direction contains a symmetric electron wave function times an anti-symmetric phonon wavefunction integrated over a symmetric interval $[-d/2; d/2]$, which due to symmetry reasons must equal zero.

The assumption of having a perfect symmetric wavefunction centered exactly in the center of the slab is not realizable in a real structure. But the assumptions seems fair when trying to give a qualitative explanation of the influence of the slab setup on the phonon properties. Thus we will only consider the deformation potential interaction between electrons and dilatational phonon modes in the following calculations[5].

The other part of the interaction matrix element, $\mathcal{G}_n$, is for the dilatational modes given by [118][6],

$$\mathcal{G}_n = \frac{1}{2\pi}\sqrt{\frac{\hbar}{2\rho\omega_n}} F_{\mathrm{dil}} (k_t^2 - k_x^2)(k_l^2 + k_x^2) \sin\left(\frac{dk_t}{2}\right), \tag{8.18}$$

[5]The electron-acoustical phonon interaction was also possible through the piezoelectric interaction. According to [116] the piezoelectric interaction in a slab only gives a small contribution compared to the deformation potential interaction, and it is reasonable still to neglect the piezoelectric interaction.

[6]The assumption about infinitely closely modes in the $\mathbf{k}_\parallel$-space such that the sum over $\mathbf{k}_\parallel$ may be evaluated as an integral, similar to Eq. (5.13), has already been applied, which is why $\mathcal{G}_n$ does not contain any phonon confinement area.

remembering that both k_l, k_t, and ω_n are functions of the continuous variable k_x and depending on the mode number n. Here $F_{\rm dil}$ is the normalization constant, which is in the case of k_l and k_t being both real or both purely imaginary is given by [118],

$$\begin{aligned}
F_{\rm dil}^{-2} &= \frac{1}{8k_lk_t}\Big[2dk_l^3k_t^5+4dk_l^3k_t^3k_x^2+2dk_lk_t^5k_x^2+10dk_l^3k_tk_x^4-4dk_lk_t^3k_x^4+2dk_lk_tk_x^6 \\
&\quad -8dk_l^3k_tk_x^2(k_t^2+k_x^2)\cos(dk_l)-2dk_lk_t(k_t^2-k_x^2)^2(k_l^2+k_x^2)\cos(dk_t) \\
&\quad +2k_t(-k_t^2+k_x^2)(k_l^2k_t^2+7k_l^2k_x^2-k_t^2k_x^2+k_x^4)\sin(dk_l)+8k_l^3k_x^2(k_t^2-k_x^2)\sin(dk_t) \\
&\quad +(k_l^2k_t^5+4k_l^3k_t^2k_x^2+6k_l^2k_t^3k_x^2-k_t^5k_x^2-4k_l^3k_x^4-7k_l^2k_tk_x^4+2k_t^3k_x^4 \\
&\quad -k_tk_x^6)\sin(d(k_l-k_t))+(k_l^2k_t^5-4k_l^3k_t^2k_x^2+6k_l^2k_t^3k_x^2-k_t^5k_x^2+4k_l^3k_x^4-7k_l^2k_tk_x^4 \\
&\quad +2k_t^3k_x^4-k_tk_x^6)\sin(d(k_l+k_t))\Big], \qquad (8.19)
\end{aligned}$$

and when $k_l = \mathrm{i}\kappa$ is purely imaginary and k_t is real becomes

$$\begin{aligned}
F_{\rm dil}^{-2} &= \frac{1}{4\kappa_lk_t}\Big[-d\kappa_l^3k_t^5-2d\kappa_l^3k_t^3k_x^2+d\kappa_lk_t^5k_x^2-5d\kappa_l^3k_tk_x^4-2d\kappa_lk_t^3k_x^4+d\kappa_lk_tk_x^6+ \\
&\quad 4d\kappa_l^3k_tk_x^2(k_t^2+k_x^2)\cosh(d\kappa_l)+d\kappa_lk_t(\kappa_l^2-k_x^2)(k_t^2-k_x^2)^2\cos(dk_t) \\
&\quad +(\kappa_l^2k_t^5+6\kappa_l^2k_t^3k_x^2+k_t^5k_x^2-7\kappa_l^2k_tk_x^4-2k_t^3k_x^4+k_tk_x^6)\sinh(d\kappa_l) \\
&\quad +4\kappa_l^3k_x^2(-k_t^2+k_x^2)\sin(dk_t)-4\kappa_l^3k_x^2(k_x^2-k_t^2)\cosh(d\kappa_l)\sin(dk_t)+(-\kappa_l^2k_t^5 \\
&\quad -6\kappa_l^2k_t^3k_x^2-k_t^5k_x^2+7\kappa_l^2k_tk_x^4+2k_t^3k_x^4-k_tk_x^6)\sinh(d\kappa_l)\cos(dk_t)\Big]. \qquad (8.20)
\end{aligned}$$

The matrix element $M_{n,\nu\nu} = D_\nu \mathcal{G}_n \mathcal{F}_{n,\nu}$ may now be calculated and describes the interaction of the electrons with the nth phonon band of the dilatational modes. The numerical calculations are most easily done in the frame of the normalized values. To implement the electronic confinement in the simplest way, we use the crude wavefunction approximation in Eq. (5.6), where $\phi_e(\mathbf{r}) = \phi_g(\mathbf{r}) = 1/(\pi^{3/4}L^{3/2})\cdot\exp[-r^2/(2L^2)]$, and we arrive at

$$\mathcal{F}_n \approx \mathrm{e}^{-(\tilde{k}_l^2+\tilde{k}_x^2)\tilde{L}^2/4}, \qquad (8.21)$$

$$\mathcal{G}_n = \frac{1}{d}\frac{1}{2\pi}\sqrt{\frac{\hbar}{2\rho c_l\tilde{\omega}_n}}\tilde{F}_{\rm dil}(\tilde{k}_t^2-\tilde{k}_x^2)(\tilde{k}_l^2+\tilde{k}_x^2)\sin(\tilde{k}_t/2), \qquad (8.22)$$

where $\tilde{L} = L/d$. When evaluating the spatial integral in $\mathcal{F}_n$, Eq. (8.16), for a QD in the center of the slab, we may when d/L is reasonably large, approximate the form factor by the bulk, as done in Eq. (8.21). From calculations we show that this approximation only introduces an insignificant error. The major influence of the phonon confinement is determined by $\mathcal{G}_n$, which contains the phonon dispersion relation.

From these normalized expression we also attain some physical insight. The form factor describes the interaction of the confined electron with the surrounding material and not the phonons specifically. Thus it only depends on $\tilde{L}$, which makes sense since Eq. (8.1) is scaling invariant. The confinement of the phonons is contained in $\mathcal{G}_n$, and it scales as d^{-1}. As the thickness of the slab is increased, more phonon modes have influence, and in the bulk limit $d \to \infty$, $\mathcal{G}_n \to 0$. But since infinite slab thickness also means infinitely many discrete phonon modes, a finite value of the total electron-phonon matrix element is still obtained when summarizing all modes, equivalent to the bulk case.

In principle Eq. (8.7) has infinitely many solutions for $\tilde{k}_t$ and $\tilde{k}_l$, meaning that n goes to ∞. For computational purposes, a cut-off of the n-sum has to be introduced. We determine a reasonable cut-off for $\tilde{k}_l$ at the value where the $\mathcal{F}_n$ has decreased to $\mathrm{e}^{-4} = 2\%$. We consider the point $\tilde{k}_x = 0$ in Fig. 8.2a from we get the requirement[7]

$$\mathrm{e}^{-[\tilde{k}_l(\tilde{k}_x=0)]^2\tilde{L}^2/4} \geq \mathrm{e}^{-4} \quad \Rightarrow \quad \tilde{k}_{l,n}(k_x=0) \leq 4/\tilde{L}. \tag{8.23}$$

From Fig. 8.2a we note that the number of modes that contribute to the interaction matrix element goes approximately as $\tilde{L}^{-1} = d/L$. Physically this agrees with the bulk case, $d \to \infty$, where infinitely many modes has to be included.

With $M_n(k_x) = M_{n,ee}(k_x) - M_{n,gg}(k_x)$, we arrive at an expression for the phonon bath correlation function similar to the bulk expression in Eq. (4.52), by summing over all the n phonon bands and integrating over the in-plane wave vector,

$$D^{\gtrless}(t) = \sum_n 2\pi \int_0^\infty \mathrm{d}k_x\, k_x\, |M_n(k_x)|^2 \left[n_{\omega_n(k_x)} \mathrm{e}^{\pm \mathrm{i}t\omega_n(k_x)} + (n_{\omega_n(k_x)}+1)\mathrm{e}^{\mp \mathrm{i}t\omega_n(k_x)} \right], \tag{8.24}$$

using $\int \mathrm{d}\mathbf{k}_\parallel = 2\pi \int_0^\infty \mathrm{d}k_x\, k_x$, and where $n_{\omega_n(k_x)}$ is the thermal occupation factor from Eq. (4.51).

8.2.1 Simulation results

A plot of the real part of $D^{>}(t)$ is given in Figs. 8.4a and 8.4b, where a significant difference from the bulk case appears, since $D^{>}(t)$ oscillates and dies out much slower than for the bulk case ($\sim 5\,\mathrm{ps}$). We verify from Fig. 8.4b that $D^{\gtrless}(t)$ looks similar for $d = 70\,\mathrm{nm}$ as for the value obtained using bulk phonons. From our analysis we found that $d = 50\,\mathrm{nm}$ was a reasonable case to describe the slab-system by bulk phonons, and already at 30 nm the deviation is small.

In the beginning the oscillations fluctuate, but for long times an oscillation at a single frequency remains, although dying out slowly. Physically this is explained by the phonons which are reflected and bounce between the surfaces. When a longitudinal phonon is reflected, it creates both a longitudinal and a transverse phonon. The transverse phonon may be reflected at the other surface, creating a new longitudinal and transverse phonon. In time the phonons will carry the energy away from the QD in the infinite radial direction, and phonon bath correlation function decays to zero.

The period of the oscillation for $d = 10\,\mathrm{nm}$ is 4.1 ps. Assuming that this is the time a phonon use to travel to the surface, be reflected, and travel back, the phonon velocity is $2.4\,\mathrm{km/s}$. This is lower than both c_l and c_t, which as previously discussed, is the property of a phonon mode localized at the surface. This also explains why the amplitude of the oscillation decreases, when the surface is moved further away from the QD by increasing d. The frequency of the oscillation exactly matches $\omega = 2.98 c_l/d$, which is the frequency where the DOS is infinite, and which corresponds to a phonon energy of 1.0 meV. The same considerations applies to the oscillation at $d = 30\,\mathrm{nm}$.

In reality, many other effects, such as anharmonic effects described in Section 2.1.1, determine the lifetime of the phonons, which at $T = 10\,\mathrm{K}$ is around 600 ps [121, 122, 123]. To include these effects in the calculation, we multiply $D^{\gtrless}(t)$ with a factor $\exp(-\gamma_{\mathrm{phon}}t)$, where $\gamma_{\mathrm{phon}} = 1/(600\,\mathrm{ps})$.

[7] In each simulation we also verify by considering $\mathcal{F}_n(k_x)$ and $\mathcal{G}_n(k_x)$ that enough modes are included, and also the enough points in the $\tilde{k}_x$-array are used.

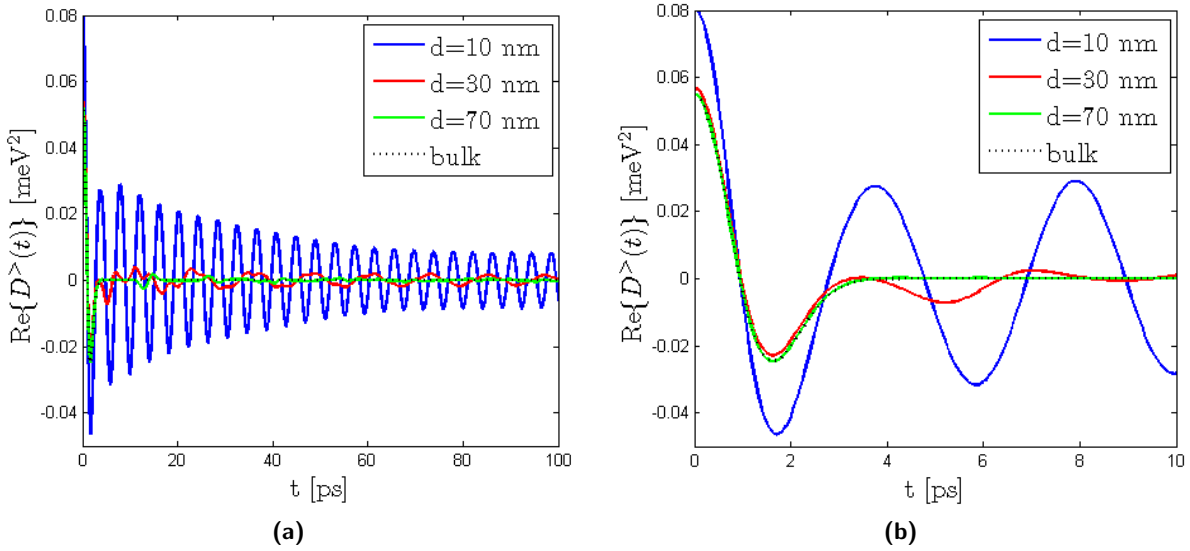

Figure 8.4: **(a)** The real part of the phonon bath correlation function plotted vs time, $L = 5\,\mathrm{nm}$ and $T = 10\,\mathrm{K}$. **(b)** The curve in (a) shown for low times.

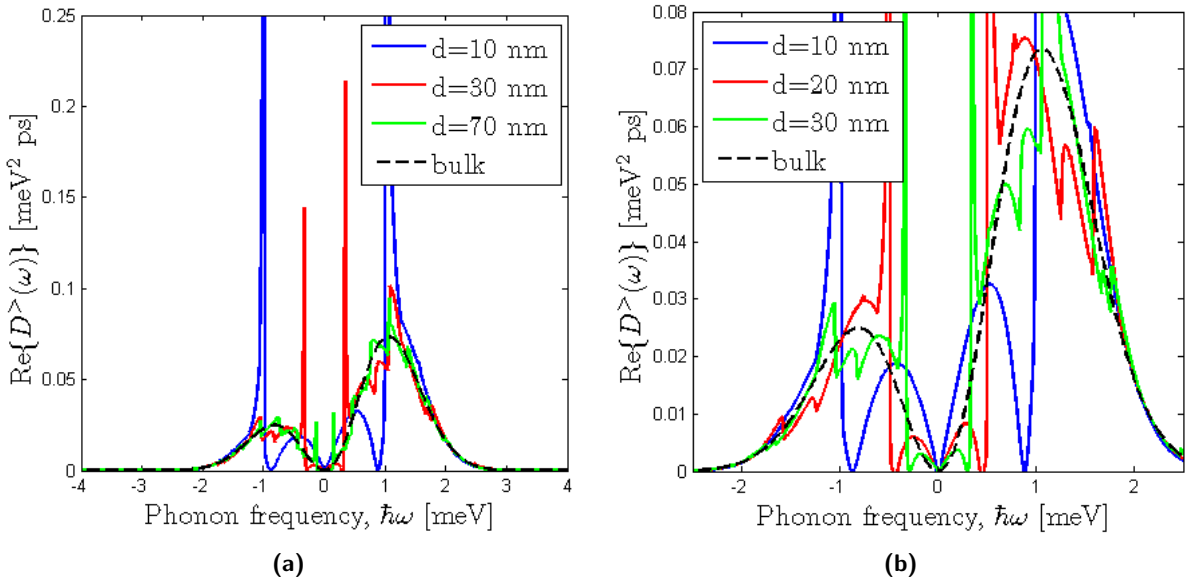

Figure 8.5: **(a)** Effective phonon spectrum versus phonon frequency plotted for different slab thickness at $T = 10\,\mathrm{K}$, calculated as the Fourier transform of Eq. (8.24) **(b)** Effective phonon spectrum versus phonon frequency plotted for different slab thickness, zoom on the low-energy part. Note that the values of d is different from (a)

As for the bulk case, we use the theory from Section 4.3 to calculate the effective phonon spectrum seen in Fig. 8.5a, where the peaks corresponding to the resonant phonon mode are present at a phonon energy of $\omega = 2.98 c_l/d$. The amplitude of the peaks decreases because as d increases, a larger percentage of the phonons are emitted into the infinite slab directions and carries energy away that will not be reflected. A very interesting fact is though that at energies slightly lower than the peaks, a small frequency range appears where the spectrum is very low, corresponding to phonon modes that are suppressed due to the slab environment. If higher values of γ_{phon} is used, we expect the resonance peaks to be wider with a smaller amplitude.

These behaviour of the effective phonon spectrum is also carried on to the lifetime plot in Fig. 8.6, as we have seen earlier. Due to long computational times, the plot is made with a large discretization in the Δ-array. Due to the rough sampling, we only observe the peak and hole for $d = 10\,\text{nm}$, but the peaks and dips should also appear for the other values of d, if the sampling density of the Δ-array is increased. Thus for a QD-cavity system with a detuning, $\Delta = 2.98 \cdot c_l/d$, the QD may decay through a resonant phonon mode in the slab, increasing the decay rate significantly. By decreasing the detuning slightly from this peak, the phonon-assisted transmission rates are essentially zero.

The pure dephasing rate may no longer be divided into a short-time and long-time effect due to the long oscillation time of $D^{\gtrless}(t)$. It may though still be divided into cavity-dependent and a cavity-independent part as seen in Eqs. (6.16) and (6.17), but the calculations get complicated, and due to the limited period of time for this project, we did not have time to continue this analysis and describe the effect on the indistinguishability more thoroughly.

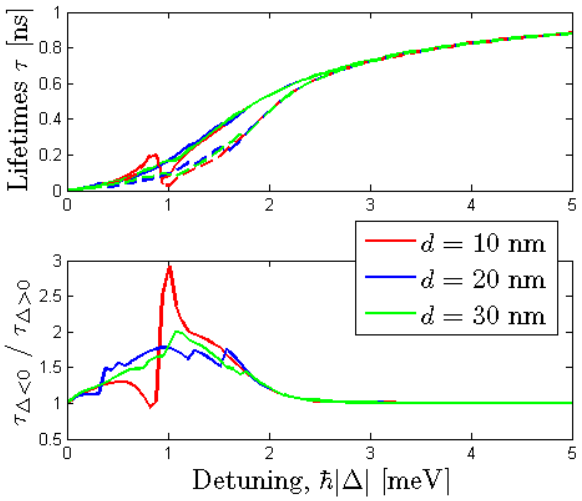

Figure 8.6: (Top) Lifetimes of the excited QD state plotted versus the detuning for different slab thickness at $T = 10\,\text{K}$, where solid (dashed) curves is for negative (positive) detunings. The plot is a little messy, so more focus should be given to the bottom plot. (Bottom) The degree of asymmetry defined as the ratio of the lifetime for opposite signs of the detuning.

8.3 Summary and discussion

We have in this chapter presented a sketch of the types of vibrational modes which in exist an infinite slab. We assumed a symmetrical electron wavefunction, placed in the center of the slab, and this will only interact with the dilatational (symmetric) slab modes. A resonant vibrational mode appeared in the slab due to a local minimum in the phonon dispersion relation at $\omega = 2.98 c_l/d$. The effect of the slab compared to the bulk case for the QD-cavity dynamics is largest for smallest d, where the system interacts significantly with only few vibrational modes. The slab may though not be so small that it changes the electronic confinement. For slabs thicker than $\approx 50\,\text{nm}$, behaviour similar to that of bulk appears.

By designing a QD-cavity system with a positive detuning matching this resonance frequency, the phonon-enhanced cavity feeding is increased greatly, and we observe a large lifetime asymmetry. By using a cavity with a slightly lower detuning, the phonon modes with a frequency matching the detuning are suppressed, giving almost no lifetime asymmetry. This behaviour of the phonon density with zeros and resonance peaks have to our knowledge not been considered for QD-cavity in a slab, but only in coupling between two coupled QDs in a slab for different spatial configurations [112, 113].

In general impurities at the surface may affect and give shorter lifetime to the resonant phonons and thus decrease the amplutide of the peaks in the effective phonon spectrum. If we take into account that the QD may be placed at an arbitrary position in the slab, the oscillations in the phonon correlation function would be more complex since phonons reflected at different surfaces will return to the dot at different times. This, or the fact that the QD wavefunction in general not is symmetric, implies the necessity to also consider the flexural (anti-symmetrical) vibrational modes in the slab. The flexural dispersion relation has a minimum in the third band, which gives another resonant phonon mode at a larger frequency than for the dilatational modes [116]. In general both resonance peaks will appear in the effective phonon spectrum, and the amplitude of these will depend on how well the electronic wavefunction overlaps with the dilational and flexural mode, respectively.

If phonon modes are suppressed for the dilatational mode, a contribution though comes from the flexural modes, vice versa, but we still expect to see dips in the total effective phonon density. Using detunings in the frequency range of the dips should give a lower phonon-induced pure dephasing rate. But due to the long temporal extend of the phonon bath correlation function, an analytical consideration of the pure dephasing rate becomes complicated, and we did not have time to go into details with this.

Summarizing, this chapter clearly shows that the effects of the phonons is altered for the dynamics of a QD-cavity system in a slab compared to the bulk case. Even when considering this simple geometry, the expression for the interaction matrix element becomes a lot more complicated compared to the bulk system.

Chapter 9

Conclusion and Outlook

In this project we have examined the dynamics of a two-level quantum dot coupled to a single optical mode interacting with a large non-Markovian phonon reservoir. Our main emphasis has been to determine how the structural confinement of both the electrons and the phonons affects the lifetime of the emitter and the indistinguishability of the emitted photons due to pure dephasing.

The physical realization of quantum dots and optical cavities are demonstrated in Chapter 1, and these show promising application for designing an efficient single-photon source. Due to the small structure of these systems, it is of highly importance to include interaction with the surroundings, which becomes a complicated problem demanding a many-body description. In Chapter 2 the different kinds of interaction Hamiltonians are sketched, where loss mechanisms are included according to the Lindblad-formalism. For this model, the only significant electron–phonon interaction mechanism is coupling to LA-phonons through the deformation potential interaction. We assume that the phonon dispersion relation does not depend on the properties of the optical cavity.

Using a quantum master equation approach, the equations of motion are derived in Chapter 3 for the reduced density operator where the phonon degrees of freedom are traced out. In Chapter 4 we formulate the problem by a linear differential equation system with time-dependent coefficients, which we solve numerically.

In Chapter 5 the model dynamics are investigated in details, assuming a simple electronic confinement by a crude, non-physical spherical wavefunction with same effective mass in the valence and conduction band, and we consider bulk phonons. For a Markovian (memoryless) phonon reservoir, the effect of the phonons is described solely by an additional pure dephasing rate. For a non-Markovian reservoir, that does have memory, a lifetime asymmetry is observed for low temperatures when the sign of the detuning between the QD and the cavity is changed. Physically this demonstrates the possibility for the QD to couple to the cavity through emission of an acoustical phonon if the QD bandgap has a higher energy than the cavity mode, but the inability if to couple if the QD bandgap is lower. This effect has been demonstrated in [1, 43], where the electronic and phononic confinement though not is examined in details, as done in this thesis.

By determining an analytical expression for the time-evolution operator of the QD-cavity system in Chapter 6, we are able to divide the phonon-induced pure dephasing rate into two parts: 1) A short-time contribution which depends strongly on the behaviour of the phonon bath correlation function and is independent of the cavity. 2) A long-time part which is cavity-

dependent and only dominates for large times. We demonstrate how the short-time rate depends on the amplitude of the whole effective phonon spectrum, whereas the long-time rate depends only on specific values of the effective phonon spectrum determined by the cavity detuning and QD-cavity coupling strength.

We discuss indistinguishability from a phenomenological expression stating that a higher indistinguishability is achieved by decreasing the emitter lifetime or increasing the decoherence time. According to this, the short- and long-time phonon-induced pure dephasing rate both has to be minimized to achieve a high indistinguishability.

In Chapter 7 the electronic confinement is examined in details analytically, assuming a spherical electron wavefunction with different confinement lengths for the ground state and excited state of an electron in the QD due to different effective masses in the energy bands. In materials as GaAs where the sign of the deformation potential constant is the same for the valence and the conduction band, the energy bands are shifted the same direction when the crystal is compressed. We demonstrate that for these materials, zeros appear in the effective phonon spectrum at certain phonon energies, which to our knowledge not have been demonstrated before. When matching the QD-cavity detuning with the zeros, the long-time phonon-induced pure dephasing rate becomes zero. By optimizing the QD geometry, the amplitude of the effective phonon spectrum may be minimized, decreasing the short-time dephasing rate. This surely demonstrate the possibility of achieving a high indistingusihability, even when having a non-zero detuning.

In general the QD wavefunction is not spherical. From a FEM-calculation of the wavefunction in a truncated conical dot structure, we see that valleys appear in the effective phonon spectrum, although not zeros, which we expect still may be used to decrease the induced pure dephasing. By fitting the FEM-wavefunction to an ellipsoidal wavefunction, we observe that the ellipsoidal model resolves the shape of the FEM-calculated effective phonon spectrum for low phonon energies, but does not catch the shape for higher energies. This should be taken into account in the literature, where a spherical/an ellipsoidal wavefunction is used without taking further notice.

In Chapter 8 we consider a coupled QD-cavity system in an infinite slab, and we demonstrate that the confinement of phonons introduce resonant vibrational modes. By matching the resonance energies with the cavity detnuning, a huge lifetime asymmetry is achieved where the QD decays through the resonant mode of the slab. Suppressed phonon modes also appear in the effective phonon spectrum, which could be exploited to reduce the pure dephasing rate. The effects are though sensible to impurities at the surfaces, etc.. In slabs thicker than 50 nm, we estimate the dynamics to be described approximately by the bulk case for a reasonably-sized self-assembled quantum dot. A standard photonic crystal cavity slab my easily be thicker, and our calculations indicate that the phonon modes in such structures may be considered as bulk phonon modes, at any rate in the slab confinement direction.

Outlook

The model we use to describe the dynamics of a QD in an optical cavity may be expanded in many ways to describe more realistic physical situations. We only discuss indistinguishability in relation to the phonon-induced pure dephasing rate. But for the non-Markovian phonon reservoir, the phonons influence more than just the pure dephasing rate. If a model describing the total dephasing effect of the phonons could be provided, this would be a large achievement.

The reservoir-description of the phonons may be expanded into a description of the occupation of each single phonon mode, characterized by the phonon frequencies, which is currently examined by Per Kær Nielsen, DTU Fotonik.

Regarding the electronic confinement, an interesting feature would be to examine how different material combinations in the QD structure would change the position of the dip in the effective phonon spectrum, due to different deformation potential values and effective masses.

Concerning the phononic confinement, other more complicated structures could be considered where change in the phononic confinement due to the optical cavity is included. Experimental results of the (former) Quantum Photonics group at DTU Fotonik demonstrate spectral broadening effects in measurements on a QD in a photonic crystal cavity, where electron-phonon interaction is indicated as a possible cause. No theoretical model has, however, been developed for describing such systems, so this is surely an interesting feature for further work on this model. Another example on a structure for confining phonons is considered by Anna Grodecka at the Niels Bohr Institute. Here, small, circular free-standing membrane structures are considered with the purpose of altering the electron-phonon interaction for a QD in the membrane.

Another totally different feature would be to consider two coupled QDs, which are promising candidates for quantum gates for quantum computation [124]. Beneficial effects might be achieved by expanding the model in this way, although it will get a lot more complicated.

This thesis demonstrates many interesting aspects that surely should be considered if a better way of examining the indistinguishability is developed in the future. This work proposes that the properties of a single-photon emitter or other quantum devices could be improved by engineering the phonon interaction by using clever electronic and phononic confinements.

Chapter 10

Appendix

A Parameter overview

In this appendix we state the parameters used in the simulations and discuss some in details.

Table A.1: Simulation Parameters

Parameter	Description	Value	Reference
d	Density of GaAs	$5.37\,\mathrm{g/m^3}$	[66]
c_l	Velocity of longitudinal acoustic waves in GaAs	$5.11\,\mathrm{km/s}$	[a)]
c_t	Velocity of transverse acoustic wave in GaAs	$3.02\,\mathrm{km/s}$	[b)]
D_e	Deformation potential for a electron in GaAs	$-14.6\,\mathrm{eV}$	[c)]
D_h	Deformation potential for a hole in GaAs	$-4.8\,\mathrm{eV}$	[c)]
$\hbar g$	Electron-photon coupling strength	$150\,\mu\mathrm{eV}$	[d)]
Γ	Relaxation rate of excited state in QD	$1\,\mathrm{ns^{-1}}$	[26]
$\hbar\kappa$	Cavity population relaxation rate	$100\,\mu\mathrm{eV}$	[33]
$\hbar\gamma$	Pure dephasing rate of QD	$0\,\mu\mathrm{eV}$	

[a)] c_l: The longitudinal sound velocity in GaAs may vary from $4.784 - 5.447\,\mathrm{km/s}$ depending on the direction of propagation compared to the various crystal planes in the GaAs crystal, $T = 77\,\mathrm{K}$ [125]. We use the value $c_l = 5.11\,\mathrm{km/s}$ used in articles dealing with electron-phonon interaction [43, 66], agreeing with the velocity obtained when averaging over all crystal directions in [125]. Other similar articles use a velocity of $5.15\,\mathrm{km/s}$ [126, 127].

[b)] c_t: The transverse sound velocity in GaAs varies from $2.479 - 3.35\,\mathrm{km/s}$ depending on the direction of propagation compared to the various crystal planes in the GaAs crystal, $T = 77\,\mathrm{K}$ [125]. We use the value $c_l = 3.02\,\mathrm{km/s}$ calculated as an average value of all the propagation directions of the value in [125], it and corresponds to values used in [128]. Other articles dealing with transverse sound waves use values from $2.80\,\mathrm{km/s}$ [126] to $3.35\,\mathrm{km/s}$ [116].

[c)] D_e, D_h: We adapt the values of the deformation potential from articles considering electron-acoustic phonon interaction, [66, 43], although it seems there a big uncertainty in determining agreeing values when measuring the deformation potentials in different experiments. This is discussed in details in [97].

[d)] $\hbar g$: For QD in cavities coupling strengths for good cavities have been shown to be on the order $100 - 200\,\mu\mathrm{eV}$ [34, 41]. Thus we pick $g = 150\,\mu\mathrm{eV}$ as a reasonable value.

B Hamiltonian in a rotating frame

In quantum mechanics, it may sometimes be advantageous to transform the Hamiltonian H of a considered (sub-)space to a rotating frame, as used in Section 4.2.

We assume that the time evolution of the state of the system, $|\psi\rangle$, is described by the Schrödinger equation, where H time-independent and given in the Schrödinger picture,

$$\mathrm{i}\hbar\frac{\partial|\psi\rangle}{\partial t} = H|\psi\rangle. \tag{B.1}$$

Let $T(t)$ be a unitary operator on the form

$$T(t) = \mathrm{e}^{-\mathrm{i}\hbar^{-1}At}, \tag{B.2}$$

where A is an arbitrary Hermitian operator. The Hermittivity is required for $T(t)$ to be unitary. The state vector is in the transformed frame using $T(t)$ given by

$$|\tilde{\psi}\rangle = T^{\dagger}(t)|\psi\rangle. \tag{B.3}$$

To determine how the H transforms, we write the Schrödinger equation for $|\tilde{\psi}\rangle$,

$$\begin{aligned}
\mathrm{i}\hbar\frac{\partial|\tilde{\psi}\rangle}{\partial t} &= \mathrm{i}\hbar T^{\dagger}(t)\frac{\partial|\psi\rangle}{\partial t} + \mathrm{i}\hbar\frac{\partial T^{\dagger}(t)}{\partial t}|\psi\rangle && \text{(B.4)}\\
&= T^{\dagger}(t)H|\psi\rangle - AT^{\dagger}(t)|\psi\rangle && \text{(B.5)}\\
&= \left[T^{\dagger}(t)HT(t) - A\right]T^{\dagger}(t)|\psi\rangle && \text{(B.6)}\\
&= \left[T^{\dagger}(t)HT(t) - A\right]|\tilde{\psi}\rangle. && \text{(B.7)}
\end{aligned}$$

Comparing to Eq. (B.1), the transformed Hamiltonian has must have the form

$$\tilde{H} = T^{\dagger}(t)HT(t) - A. \tag{B.8}$$

C Jaynes-Cummings model

The dynamics of a coupled QD-cavity system may be described by the Jaynes–Cummings model when no losses or phonon scattering are included, see e.g. [39, sec. 4.5]. The Hamiltonian describing the system is given by Eq. (4.17),

$$H_s = \hbar\Delta\sigma_{11} + \hbar g(\sigma_{12} + \sigma_{21}). \tag{C.1}$$

We write the state vector as

$$|\psi(t)\rangle = C_1(t)|1\rangle + C_2(t)|2\rangle, \tag{C.2}$$

where $|C_1(t)|^2$ and $|C_2(t)|^2$ is the excited quantum dot state and cavity populations, respectively. We use the initial conditions for an excited QD state, $C_1(0) = 1$ and $C_2(0) = 0$. By inserting $|\psi(t)\rangle$ into the Schrödinger equation,

$$\mathrm{i}\hbar\frac{\partial|\psi(t)\rangle}{\partial t} = H_s|\psi(t)\rangle, \tag{C.3}$$

we get

$$\mathrm{i}\hbar\partial_t C_1(t)|1\rangle + \mathrm{i}\hbar\partial_t C_2(t)|2\rangle = \hbar\Delta C_1(t)|1\rangle + \hbar g\left(C_1(t)|2\rangle + C_2(t)|1\rangle\right). \tag{C.4}$$

Projecting onto the state $|1\rangle$ and $|2\rangle$ respectively, gives

$$\mathrm{i}\partial_t C_1(t) = \Delta C_1(t) + gC_2(t), \tag{C.5}$$

$$\mathrm{i}\partial_t C_2(t) = gC_1(t). \tag{C.6}$$

By solving this linear differential system, we determine $C_1(t)$ and $C_2(t)$ and may calculate the population of the excited QD state as

$$|C_1(t)|^2 = 1 - \frac{g^2}{g^2 + (\Delta/2)^2}\sin^2\left(\sqrt{g^2 + (\Delta/2)^2}t\right). \tag{C.7}$$

The cavity population $|C_2(t)|^2$ may be determined through population conservation, $|C_1(t)|^2 + |C_2(t)|^2 = 1$.

D Lifetime in the adiabatic limit

In this appendix we derive in Section D.1 in details the effective decay rate in the adiabatic approximation of the lossy Jaynes-Cummings model in the bad cavity regime, described in Section 5.1.2. In Section D.2 the same principles are carried on to derive an expression for the decay rate when also phonon scattering is included given in Eq. (5.17), which is shown to be

$$\Gamma_{\text{tot}} = \Gamma + 2g^2 \frac{\gamma_{\text{tot}}}{\gamma_{\text{tot}}^2 + \Delta^2} \left[1 + \frac{1}{\hbar^2 \gamma_{\text{tot}}} \text{Re}\{D^{>}(\omega = \Delta)\} \right]. \tag{D.1}$$

This expression has been stated in [69], but since the derivation is not included, we present a detailed derivation here.

D.1 No phonon interaction

When no phonon reservoir is included in the model, only the coherent terms in Eq. (4.33) and the Lindblad dissipative terms, Eq. (4.36), are included, giving the equations of motion

$$\begin{aligned}
\partial_t \langle \sigma_{11} \rangle &= -\Gamma \langle \sigma_{11} \rangle - \text{i}g \langle \sigma_{12} \rangle + \text{i}g \langle \sigma_{21} \rangle, && \text{(D.2)} \\
\partial_t \langle \sigma_{11} \rangle &= -\kappa \langle \sigma_{22} \rangle + \text{i}g \langle \sigma_{12} \rangle - \text{i}g \langle \sigma_{21} \rangle, && \text{(D.3)} \\
\partial_t \langle \sigma_{12} \rangle &= (-\gamma_{\text{tot}} + \text{i}\Delta) \langle \sigma_{12} \rangle - \text{i}g (\langle \sigma_{11} \rangle - \langle \sigma_{22} \rangle) = [\partial_t \langle \sigma_{21} \rangle]^*, && \text{(D.4)}
\end{aligned}$$

where we omit writing the time-dependence on the σs, and where $\gamma_{\text{tot}} = (\Gamma + \kappa)/2 + \gamma$. We only consider the off-resonant case in the adiabatic limit, $\Delta \gg g$, where $\partial_t \langle \sigma_{12} \rangle \approx 0$ due to the fast oscillation of the polarisation, giving

$$\langle \sigma_{12} \rangle = \frac{\text{i}g}{-\gamma_{\text{tot}} + \text{i}\Delta} (\langle \sigma_{11} \rangle - \langle \sigma_{22} \rangle). \tag{D.5}$$

By inserting this into Eq. (D.2) we get

$$\begin{aligned}
\partial_t \langle \sigma_{11} \rangle &= -\Gamma \langle \sigma_{11} \rangle + \text{i}g \left(\frac{-\text{i}g}{-\gamma_{\text{tot}} - \text{i}\Delta} - \frac{\text{i}g}{-\gamma_{\text{tot}} + \text{i}\Delta} \right) (\langle \sigma_{11} \rangle - \langle \sigma_{12} \rangle) && \text{(D.6)} \\
&= -(\Gamma + R) \langle \sigma_{11} \rangle + R \langle \sigma_{22} \rangle, && \text{(D.7)}
\end{aligned}$$

where

$$R = 2g^2 \frac{\gamma_{\text{tot}}}{\gamma_{\text{tot}}^2 + \Delta^2}. \tag{D.8}$$

Similarly we find

$$\partial_t \langle \sigma_{22} \rangle = -(\kappa + R) \langle \sigma_{22} \rangle + R \langle \sigma_{11} \rangle. \tag{D.9}$$

We are able to determine a simple solution to the coupled equations Eqs. (D.7) and (D.9) in the Purcell regime described by $\kappa \gg R$. The two coupled first-order differential equations with the initial conditions $\langle \sigma_{11}(0) \rangle = 1$ and $\langle \sigma_{22}(0) \rangle = 0$ may be re-written into one ordinary second-order differential equation by differentiating Eq. (D.7) with respect to t and inserting $\partial_t \langle \sigma_{22} \rangle$ from Eq. (D.9), giving

$$\partial_t^2 \langle \sigma_{11} \rangle = -(\Gamma + R + \kappa + R) \partial_t \langle \sigma_{11} \rangle - (\kappa\Gamma + \kappa R + R\Gamma) \langle \sigma_{11} \rangle, \tag{D.10}$$

with the initial conditions $\langle\sigma_{11}(0)\rangle = 1$ and $\partial_t\langle\sigma_{11}(t)\rangle|_{t=0} = -(\Gamma+R)$ where the latter is obtained directly from Eq. (D.7).

The eigenvalues of the characteristic polynomium are

$$\lambda = \frac{-\Gamma-\kappa-2R \pm \sqrt{(\Gamma+\kappa+2R)^2 - 4(\kappa\Gamma+\kappa R+R\Gamma)}}{2} \tag{D.11}$$

$$= \frac{-\Gamma-\kappa-2R \pm (\Gamma-\kappa)\sqrt{1+\frac{4R^2}{(\Gamma-\kappa)^2}}}{2}. \tag{D.12}$$

In the limit $\kappa \gg R$,

$$\frac{4R^2}{(\Gamma-\kappa)^2} \ll 1 \quad \Rightarrow \quad \lambda = -(\Gamma+R) \ \vee \ \lambda = -\kappa. \tag{D.13}$$

The solution to Eq. (D.10) in this limit is

$$\langle\sigma_{11}(t)\rangle = A_1 \mathrm{e}^{-(\Gamma+R)t} + A_2 \mathrm{e}^{-\kappa t}. \tag{D.14}$$

The constants A_1 and A_2 are determined from the initial conditions to be $A_1 = 1$ and $A_2 = 0$, giving the final solution

$$\langle\sigma_{11}(t)\rangle = \mathrm{e}^{-(\Gamma+R)t}. \tag{D.15}$$

In this Purcell regime where $\kappa \gg R$, the decay of the QD thus is enhanced by an additional rate given by R.

D.2 Including Phonon Interaction

The description of the dynamics of the full model where the phonon reservoir is included, is determined by Eq. (4.33), (4.36) and (4.46). Omitting writing the time dependence of the σs, $\mathcal{G}^{\gtrless}(t)$, and $\tilde{\gamma}_{12}(t) = \gamma_{12}(t) - \mathrm{i}\Delta_{\mathrm{pol}}$, the dynamics are described by the set of coupled equations

$$\partial_t\langle\sigma_{11}\rangle = -\mathrm{i}g\langle\sigma_{12}\rangle + \mathrm{i}g\langle\sigma_{21}\rangle - \Gamma\langle\sigma_{11}\rangle, \tag{D.16}$$

$$\partial_t\langle\sigma_{22}\rangle = \mathrm{i}g\langle\sigma_{12}\rangle - \mathrm{i}g\langle\sigma_{21}\rangle - \kappa\langle\sigma_{22}\rangle, \tag{D.17}$$

$$\partial_t\langle\sigma_{12}\rangle = -\mathrm{i}\left(g+\mathcal{G}^{>}\right)\langle\sigma_{11}\rangle + \mathrm{i}\left(g+\mathcal{G}^{<}\right)\langle\sigma_{22}\rangle + (\mathrm{i}\Delta - \gamma_{\mathrm{tot}} - \tilde{\gamma}_{12})\langle\sigma_{12}\rangle, \tag{D.18}$$

$$\partial_t\langle\sigma_{21}\rangle = \partial_t\langle\sigma_{12}\rangle^*. \tag{D.19}$$

In the adiabatic approximation, $\partial_t\langle\sigma_{12}\rangle \approx 0$ as discussed in the previous section, giving

$$\partial_t\langle\sigma_{11}\rangle = \left(-\mathrm{i}g\frac{\mathrm{i}(g+\mathcal{G}^{>})}{\mathrm{i}\Delta - \gamma_{\mathrm{tot}} - \tilde{\gamma}_{12}} + \mathrm{i}g\frac{-\mathrm{i}(g+[\mathcal{G}^{>}]^*)}{-\mathrm{i}\Delta - \gamma_{\mathrm{tot}} - \tilde{\gamma}_{12}^*}\right)\langle\sigma_{11}\rangle - \Gamma\langle\sigma_{11}\rangle \tag{D.20}$$

$$= \left(g\frac{(g+\mathcal{G}^{>})(-\mathrm{i}\Delta - \gamma_{\mathrm{tot}} - \tilde{\gamma}_{12}) + (g+[\mathcal{G}^{>}]^*)(\mathrm{i}\Delta - \gamma_{\mathrm{tot}} - \tilde{\gamma}_{12}^*)}{|\mathrm{i}\Delta - \gamma_{\mathrm{tot}} - \tilde{\gamma}_{12}|^2} - \Gamma\right)\langle\sigma_{11}\rangle \tag{D.21}$$

$$= \left(g\frac{-2g\gamma_{\mathrm{tot}} - 2g\mathrm{Re}\{\tilde{\gamma}_{12}\} + 2\Delta\mathrm{Im}\{\mathcal{G}^{>}\} - 2\gamma_{\mathrm{tot}}\mathrm{Re}\{\mathcal{G}^{>}\} - 2\mathrm{Re}\{\mathcal{G}^{>}\tilde{\gamma}_{12}^*\}}{|\mathrm{i}\Delta - \gamma_{\mathrm{tot}} - \tilde{\gamma}_{12}|^2} - \Gamma\right)\langle\sigma_{11}\rangle, \tag{D.22}$$

using the well-known relations for complex numbers z, $2\mathrm{Re}\{z\} = z + z^*$ and $2\mathrm{i}\,\mathrm{Im}\{z\} = z - z^*$.

The next step is to express the terms in Eq. (D.22) containing $\mathcal{G}^{>}$ and $\tilde{\gamma}_{12}$ in terms of the effective phonon spectrum. The time evolution operator $U(t)$ is given by

$$U(t) \;=\; \mathrm{e}^{-\mathrm{i}H_s t/\hbar} = I + (-\mathrm{i}t)H_S + (-\mathrm{i}t)^2 H_S^2 + (-\mathrm{i}t)^3 H_S^3 + \ldots, \tag{D.23}$$

where I is the identity operator and

$$H_S = \begin{bmatrix} \Delta & g & 0 \\ g & 0 & 0 \\ 0 & 0 & 0 \end{bmatrix}. \tag{D.24}$$

In the limit $g \ll \Delta$, the expression of $U(t)$ reduces to

$$\begin{aligned}
U(t) &= \begin{bmatrix} 1 & 0 & 0 \\ 0 & 1 & 0 \\ 0 & 0 & 1 \end{bmatrix} + (-\mathrm{i}t) \begin{bmatrix} \Delta & g & 0 \\ g & 0 & 0 \\ 0 & 0 & 0 \end{bmatrix} + (-\mathrm{i}t)^2 \begin{bmatrix} \Delta^2 & \Delta g & 0 \\ \Delta g & g^2 & 0 \\ 0 & 0 & 0 \end{bmatrix} + \ldots && \text{(D.25)} \\
&= \begin{bmatrix} 1 + (-\mathrm{i}t)\Delta + (-\mathrm{i}t)^2\Delta^2 + \ldots & \frac{g}{\Delta}\left[(-\mathrm{i}t)\Delta + (-\mathrm{i}t)^2\Delta^2 + \ldots\right] & 0 \\ \frac{g}{\Delta}\left[(-\mathrm{i}t)\Delta + (-\mathrm{i}t)^2\Delta^2 + \ldots\right] & 1 + \frac{g^2}{\Delta^2}\left[(-\mathrm{i}t)^2\Delta^2 + \ldots\right] & 0 \\ 0 & 0 & 1 \end{bmatrix} && \text{(D.26)} \\
&= \begin{bmatrix} \mathrm{e}^{-\mathrm{i}t\Delta} & \frac{g}{\Delta}\left[\mathrm{e}^{-\mathrm{i}t\Delta} - 1\right] & 0 \\ \frac{g}{\Delta}\left[\mathrm{e}^{-\mathrm{i}t\Delta} - 1\right] & 1 + \frac{g^2}{\Delta^2}\left[\mathrm{e}^{-\mathrm{i}t\Delta} - 1 - (-\mathrm{i}t)\Delta\right] & 0 \\ 0 & 0 & 1 \end{bmatrix} && \text{(D.27)} \\
&\approx \begin{bmatrix} \mathrm{e}^{-\mathrm{i}t\Delta} & \frac{g}{\Delta}\left[\mathrm{e}^{-\mathrm{i}t\Delta} - 1\right] & 0 \\ \frac{g}{\Delta}\left[\mathrm{e}^{-\mathrm{i}t\Delta} - 1\right] & 1 & 0 \\ 0 & 0 & 1 \end{bmatrix}. && \text{(D.28)}
\end{aligned}$$

For notational simplicity we introduce the two functions

$$A^{\gtrless}(t) = \int_0^t \mathrm{d}t'\, D^{\gtrless}(t') \;\text{ and }\; B^{\gtrless}(t) = \int_0^t \mathrm{d}t'\, D^{\gtrless}(t')\mathrm{e}^{\mathrm{i}t'\Delta}. \tag{D.29}$$

With these and the approximate expression for $U(t)$ in Eq. (D.28), we may re-write the expressions for $\mathcal{G}^{\gtrless}(t)$ and $\gamma_{12}(t)$,

$$\begin{aligned}
\mathcal{G}^{\gtrless}(t) &= \mathrm{i}\hbar^{-2} \int_0^t \mathrm{d}t'\, U_{11}^*(t') U_{21}(t') D^{\gtrless}(t') && \text{(D.30)} \\
&= \mathrm{i}\hbar^{-2} \int_0^t \mathrm{d}t'\, \mathrm{e}^{\mathrm{i}t'\Delta} \frac{g}{\Delta} (\mathrm{e}^{-\mathrm{i}t'\Delta} - 1) D^{\gtrless}(t') && \text{(D.31)} \\
&= \mathrm{i}\hbar^{-2} \frac{g}{\Delta} \int_0^t \mathrm{d}t'\, (1 - \mathrm{e}^{\mathrm{i}t'\Delta}) D^{\gtrless}(t') && \text{(D.32)} \\
&= \mathrm{i}\hbar^{-2} \frac{g}{\Delta} \left(A^{\gtrless}(t) - B^{\gtrless}(t)\right), && \text{(D.33)}
\end{aligned}$$

and

$$\begin{aligned}
\gamma_{12}(t) &= \hbar^{-2}\int_0^t \mathrm{d}t' \, \left[|U_{11}(t')|^2 D^<(t') - |U_{21}(t')|^2 D^>(t')\right] && \text{(D.34)}\\
&= \hbar^{-2}\int_0^t \mathrm{d}t' \, \left[D^<(t') - \frac{g^2}{\Delta^2}(\mathrm{e}^{-\mathrm{i}t'\Delta}-1)(\mathrm{e}^{\mathrm{i}t'\Delta}-1)D^>(t')\right] && \text{(D.35)}\\
&\approx \hbar^{-2}\int_0^t \mathrm{d}t' \, D^<(t') && \text{(D.36)}\\
&= \hbar^{-2}A^<(t) && \text{(D.37)}
\end{aligned}$$

where it is used that $\gamma^2/\Delta^2 \ll 1$. Using these expressions we may simplify some of the terms in Eq. (D.22):

$$-2g\mathrm{Re}\{\tilde{\gamma}_{12}\} + 2\Delta\mathrm{Im}\{\mathcal{G}^>\} = -2g\hbar^{-2}\Big[\mathrm{Re}\{A^<(t)\} - \mathrm{Re}\{A^>(t)\} + \mathrm{Re}\{B^>(t)\}\Big] \quad \text{(D.38)}$$

Using that $[D^{\gtrless}(t)]^* = D^{\lessgtr}(t)$, we have

$$\begin{aligned}
\mathrm{Re}\{A^<(t)\} - \mathrm{Re}\{A^>(t)\} &= \mathrm{Re}\left\{\int_0^t \mathrm{d}t' \, \left[D^<(t') - [D^<(t')]^*\right]\right\} && \text{(D.39)}\\
&= \mathrm{Re}\left\{2\mathrm{i}\int_0^t \mathrm{d}t' \, \mathrm{Im}\{D^<(t')\}\right\} && \text{(D.40)}\\
&= 0, && \text{(D.41)}
\end{aligned}$$

arriving at

$$-2g\mathrm{Re}\{\tilde{\gamma}_{12}\} + 2\Delta\mathrm{Im}\{\mathcal{G}^>\} = -2g\hbar^{-2}\mathrm{Re}\{B^>(t)\}. \quad \text{(D.42)}$$

Two of the other terms in Eq. (D.22) become

$$-2\gamma_{\mathrm{tot}}\mathrm{Re}\{\mathcal{G}^>\} = 2\hbar^{-2}\gamma_{\mathrm{tot}}\frac{g}{\Delta}\mathrm{Im}\{A^>(t) - B^>(t)\}, \quad \text{(D.43)}$$

and

$$\begin{aligned}
-2\mathrm{Re}\{\mathcal{G}^>\tilde{\gamma}_{12}\} &= -2\mathrm{Re}\left\{\mathrm{i}\hbar^{-2}\frac{g}{\Delta}[A^>(t) - B^>(t)]\cdot\hbar^{-2}[A^<(t) - \mathrm{iIm}\{A^<(\infty)\}]^*\right\} && \text{(D.44)}\\
&= 2\hbar^{-4}\frac{g}{\Delta}\mathrm{Im}\left\{[A^>(t) - B^>(t)]\cdot[A^<(t) - \mathrm{iIm}\{A^<(\infty)\}]^*\right\}. && \text{(D.45)}
\end{aligned}$$

Both Eqs. (D.43) and (D.45) scales with g/Δ and are in the limit $g \ll \Delta$ small compared to Eq. (D.42). Thus we may approximate Eq. (D.22) by

$$\partial_t\langle\sigma_{11}(t)\rangle = -\left[\Gamma + \frac{2g^2\gamma_{\mathrm{tot}}}{|\mathrm{i}\Delta - \gamma_{\mathrm{tot}} - \tilde{\gamma}_{12}(t)|^2}\left(1 + \frac{\hbar^{-2}}{\gamma_{\mathrm{tot}}}\mathrm{Re}\{B^>(t)\}\right)\right]\langle\sigma_{11}\rangle. \quad \text{(D.46)}$$

By only including terms to first-order in $D^{\gtrless}(t)$, we arrive at Eq. (D.1).

E Displacement of the electron and hole wavefunction

In general we may not be sure, that the wavefunctions of an electron and a hole in a quantum dot are concentric, due to their different effective masses. In this appendix we demonstrate, that for bulk phonons in the model, reasonable displacements only have insignificant effect on the system dynamics. We do calculations similar to those in Section 7.1.

We assume that the carrier wavefunctions are spherical with different widths,

$$\phi_\nu(\mathbf{r}) = \phi_\nu(\rho, z) = \frac{1}{\pi^{3/4} L_\nu^{3/2}} \mathrm{e}^{-[\rho^2 + (z - z_{0,\nu})^2]/(2L_\nu^2)}, \tag{E.1}$$

where the centres of the wavefunctions are in $(\rho, z) = (0, z_{0,\nu})$. The Fourier transform of the wavefunctions is

$$\int \mathrm{d}\mathbf{r}\, |\phi_\nu(\mathbf{r})|^2 \mathrm{e}^{-\mathrm{i}\mathbf{k}\cdot\mathbf{r}} = \mathrm{e}^{-(k_\rho^2 + k_z^2)L_\nu^2/4} \mathrm{e}^{-\mathrm{i}k_z z_{0,\nu}}, \tag{E.2}$$

with $k_\rho^2 + k_z^2 = k^2$. We assume that the carrier waevfunctions are separated by a distance z_0 along the z-axis,

$$z_{0,\nu} = \begin{cases} 0 & \text{if } \nu = \mathrm{e}, \\ z_0 & \text{if } \nu = \mathrm{g}. \end{cases} \tag{E.3}$$

With this the difference in interaction matrix elements, $M^{\mathbf{k}} = M^{\mathbf{k}}_{\mathrm{ee}} - M^{\mathbf{k}}_{\mathrm{gg}}$, becomes

$$M^{\mathbf{k}} = \sqrt{\frac{\hbar k}{2\rho c_l V}} \left(D_e \mathrm{e}^{-(k_\rho^2 + k_z^2)L_e^2/4} - D_g \mathrm{e}^{-(k_\rho^2 + k_z^2)L_g^2/4 - \mathrm{i}k_z z_0} \right). \tag{E.4}$$

By evaluating the effective phonon spectrum as in Section 7.1, we arrive at

$$\begin{aligned} \mathrm{Re}\{D^>(\omega)\} \;=\; & \frac{\hbar}{4\pi\rho c_l^5} \frac{\omega^3}{1 - \exp(-\beta\hbar\omega)} \Big[D_e^2 \mathrm{e}^{-\omega^2 L_e^2/(2c_l^2)} + D_g^2 \mathrm{e}^{-\omega^2 L_g^2/(2c_l^2)} \\ & - 2D_e D_g \,\mathrm{sinc}\left(\frac{\omega z_0}{c_l}\right) \mathrm{e}^{-\omega^2 (L_e^2 + L_g^2)/(4c_l^2)} \Big]. \end{aligned} \tag{E.5}$$

In the limit $z_0 \to 0$, $\mathrm{sinc}\left(\frac{\omega z_0}{c_l}\right) \to 1$, and the effective phonon spectrum is identical to the one derived in Eq. (7.14).

In a quantum dot of the type that we consider, the maximum heights are around 10 nm. In these it would be reasonable to expect values of z_0 of maximum 1 nm, which we from a plot of Eq. (E.5) in Fig. A.1 see only gives a small change in the effective phonon spectrum.

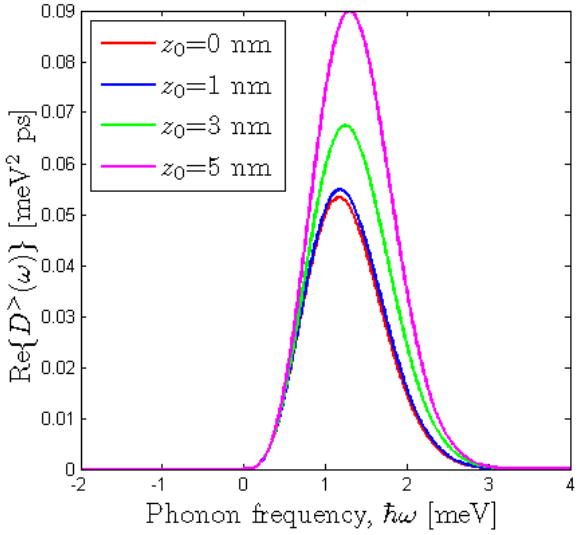

Figure A.1: Effective phonon spectrum plotted for different displacements between the centres of the excited and ground state wavefunction.

F Numerical verification of FEM-calculations

In this appendix we discuss the FEM-implementation of the Schrödinger equation in Eq. (7.24) in details, and the appendix is divided into three parts. In the first part we describe in details how the differential equation for $\chi(\rho, z)$,

$$\left[-\frac{\hbar}{2\rho}\frac{\partial}{\partial\rho}\left(\frac{\rho}{m^*}\frac{\partial}{\partial\rho}\right) - \frac{\hbar^2}{2}\frac{\partial}{\partial z}\left(\frac{1}{m^*}\frac{\partial}{\partial z}\right) + \frac{n^2\hbar^2}{2m^*\rho^2} + V(\rho, z)\right]\chi_n(\rho, z) = E\chi_n(\rho, z), \tag{F.1}$$

with the boundary conditions

- $\chi_n(\rho = 0, z) = 0$ for $n \neq 0$,
- $\partial_\rho\chi_n(\rho, z)|_{\rho=0} = 0$ for $n = 0$,
- $\chi_n(\rho, \pm L_0/2) = \chi_n(R_0, z) = 0$.

from Section 7.2 is implemented in the FEM-solver COMSOL. This requires a normalization of Eq. (F.1).

In the second the implementation is verified by comparing a calculation of the eigenenergies in a finite quantum well with analytical results. The third part deal with a QD structure and we verify that enough mesh points are used in our calculations.

The energy diagram of the QD is sketched in Fig. A.2, where I refers to the QD/wetting layer region, and II refers to the surrounding barrier material. Thus

$$m^* = \begin{cases} m_{\mathrm{I}} & \text{if } (\rho, z) \in \mathrm{I} \\ m_{\mathrm{II}} & \text{if } (\rho, z) \in \mathrm{II} \end{cases} \tag{F.2}$$

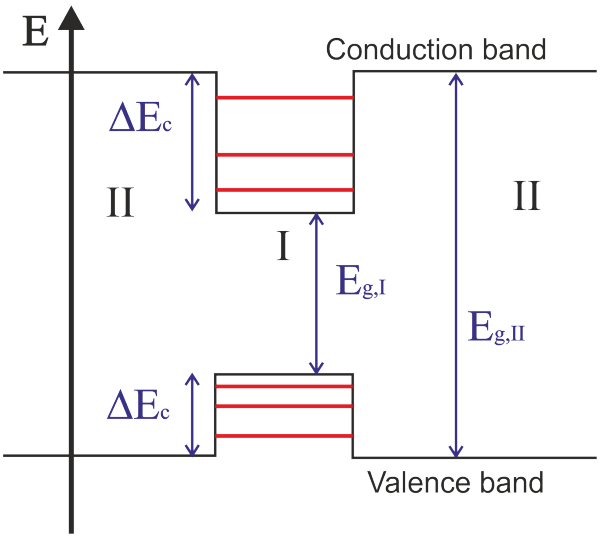

Figure A.2: A finite quantum well structure where modes with discretized energy spectrum exist in the well. The parameters are explained in the main text.

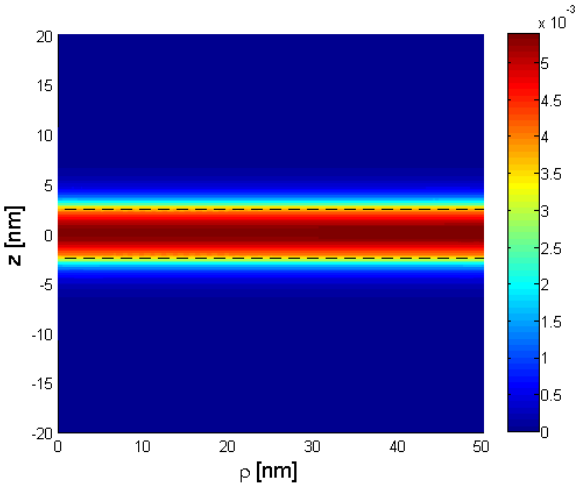

Figure A.3: The wavefunction of the fundamental mode in a the finite quantum well as described in Fig. A.2, plotted with arb. units. The dashed lines indicate the slab surfaces.

and by placing the zero point of the energy of the conduction (valence) band at the bottom (top) of the potential well, see figreffiniteQW,

$$V(r,z) = \begin{cases} 0 & \text{if } (\rho,z) \in \text{I} \\ \delta E_{c/v} & \text{if } (\rho,z) \in \text{II} \end{cases} \tag{F.3}$$

depending on the band. Note that the direction of the energy scale is downwards on the figure for the valence band.

F.1 Normalization

To simplify the normalization, we may express Eq. (F.1) in the two domains I and II,

$$-\left[\frac{1}{\rho}\frac{\partial}{\partial\rho}\left(\rho\frac{\partial}{\partial\rho}\right)+\frac{\partial^2}{\partial z^2}+\frac{n^2}{\rho^2}\right]\chi_n(\rho,z)=\frac{2m_{\text{I}}}{\hbar^2}E\chi_n(\rho,z), \tag{F.4}$$

and

$$-\left[\frac{1}{\rho}\frac{\partial}{\partial\rho}\left(\rho\frac{\partial}{\partial\rho}\right)+\frac{\partial^2}{\partial z^2}+\frac{n^2}{\rho^2}+\frac{2m_{\text{II}}}{\hbar^2}V\right]\chi_n(\rho,z)=\frac{2m_{\text{II}}}{\hbar^2}E\chi_n(\rho,z), \tag{F.5}$$

where $V = \Delta E_{v/c}$, where v/c refers to if the valence or conduction band is considered. By introducing a parameter describing the relative effective mass in the two domains, $\eta = m_{\text{I}}/m_{\text{II}}$, Eq. (F.5) may be written as

$$-\eta\left[\frac{1}{\rho}\frac{\partial}{\partial\rho}\left(\rho\frac{\partial}{\partial\rho}\right)+\frac{\partial^2}{\partial z^2}+\eta\frac{n^2}{\rho^2}+\frac{2m_{\text{I}}}{\hbar^2}V\right]\chi_n(\rho,z)=\frac{2m_{\text{I}}}{\hbar^2}E\chi_n(\rho,z), \tag{F.6}$$

We define the four unitless parameters $\tilde{\rho}$, $\tilde{z}$, $\tilde{E}$, and $\tilde{V}$ determined by

$$\rho = L\tilde{\rho},\quad z = L\tilde{z},\quad E=\frac{\hbar^2}{2m_{\text{I}}L^2}\tilde{E},\quad V=\frac{\hbar^2}{2m_{\text{I}}L^2}\tilde{V}, \tag{F.7}$$

where L is a length parameter in units of length. With these, Eqs. (F.4) and (F.6) may be written on a normalized form,

$$-\left[\frac{1}{\tilde{\rho}}\frac{\partial}{\partial\tilde{\rho}}\left(\tilde{\rho}\frac{\partial}{\partial\tilde{\rho}}\right)+\frac{\partial^2}{\partial z^2}+\frac{n^2}{\tilde{\rho}^2}\right]\chi(\tilde{\rho},z)=\tilde{E}\chi(\tilde{\rho},z), \tag{F.8}$$

and

$$-\eta\left[\frac{1}{\tilde{\rho}}\frac{\partial}{\partial\tilde{\rho}}\left(\tilde{\rho}\frac{\partial}{\partial\tilde{\rho}}\right)+\frac{\partial^2}{\partial z^2}+\eta\frac{n^2}{\tilde{\rho}^2}+\tilde{V}\right]\chi(\tilde{\rho},z)=\tilde{E}\chi(\tilde{\rho},z). \tag{F.9}$$

F.2 Finite quantum well

To verify that the implemention of the equation, the boundary conditions, and the parameter values are implemented correctly, we compare a FEM-calculation of the ground state energy of a finite quantum well with the value obtained from an analytic solution. We only calculate the two-dimensional wavefunction $\chi(r,z)$, due to the rotational symmetry.

In a finite quantum well the electrons are only confined in one direction which we denote the z-direction. In this case, the one-band Schrödinger equation simplifies to

$$-\frac{\mathrm{d}^2\psi}{\mathrm{d}z^2} = \frac{2m_\mathrm{I}}{\hbar^2}E\psi(z) \quad \text{for } z \in \mathrm{I}, \tag{F.10}$$

$$-\frac{\mathrm{d}^2\psi}{\mathrm{d}z^2} + \frac{2m_\mathrm{II}}{\hbar^2}V\psi(x) = \frac{2m_\mathrm{II}}{\hbar^2}E\psi(z) \quad \text{for } z \in \mathrm{II}. \tag{F.11}$$

By normalizing the parameters as before according to Eq. (F.7), these equations become

$$-\frac{\mathrm{d}^2\psi}{\mathrm{d}\tilde{z}^2} = \tilde{E}\psi(\tilde{z}) \quad \text{for } z \in \mathrm{I} \tag{F.12}$$

$$-\eta\frac{\mathrm{d}^2\psi}{\mathrm{d}\tilde{z}^2} = (\tilde{E} - \tilde{V})\psi(\tilde{z}) \quad \text{for } z \in \mathrm{II} \tag{F.13}$$

The potential landscape is symmetric with respect to $z = 0$, and thus we expect symmetric (with even-parity) and anti-symmetric (with odd-parity) wavefunctions. By applying a standard differential equation solution method [104], using the symmetry statement and the boundary conditions

$$\psi_\mathrm{I}(z = \pm d/2) = \psi_\mathrm{II}(z = \pm d/2), \quad \text{and} \quad \left.\frac{\mathrm{d}\psi_\mathrm{I}}{\mathrm{d}z}\right|_{z=\pm d/2} = \left.\frac{\mathrm{d}\psi_\mathrm{II}}{\mathrm{d}z}\right|_{z=\pm d/2}, \tag{F.14}$$

we may show that the even wavefunctions have eigenenergies described by the transcendental equation

$$\tan\left(\sqrt{\tilde{E}}\frac{\tilde{d}}{2}\right) = \sqrt{\eta}\sqrt{\frac{\tilde{V}}{\tilde{E}} - 1}, \tag{F.15}$$

with $\tilde{d} = d/L$. For the case of $\eta = 1$, this derivation is carried out in standard textbooks [104], and in the limit $\eta = 1$ of Eq. (F.15), the expression agrees with the textbook result.

The parameter values used in the calculation are taken from [75] and are given in Table A.2, where we consider a pure quantum dot/well of InAs surrounded by bulk GaAs. As in [36], the conduction and valence band offsets are given by

$$\Delta E_\mathrm{c} = 0.654 \times (E_\mathrm{g,GaAs} - E_\mathrm{g,InAs}), \tag{F.16}$$

$$\Delta E_\mathrm{v} = 0.346 \times (E_\mathrm{g,GaAs} - E_\mathrm{g,InAs}). \tag{F.17}$$

Furthermore we consider the effective mass in the [001]-direction, the z-direction, and for the effective masses in the valence band, we use the heavy hole values.

The fundamental mode is defined as the mode with the lowest energy, which is described by an even wavefunction, see Fig. A.3. To verify the implementation of the normalized Schrödinger equation in COMSOL we thus compare $\tilde{E}$ obtained from the simulation with the analytical result. Using the parameters described in Table A.2 and same mesh refinement as in the simulations, we obtain $\tilde{E}_\mathrm{analytic} = 0.11657$ and $\tilde{E}_\mathrm{numerical} = 0.11662$ giving a relative error of only 4×10^{-4}. This verifies our implementation of the cylindrical Schrödinger equation.

Table A.2: Band parameters used in the FEM simulations - the same as used in [36], all taken from [75].

Parameter	Description	Unit
$E_{\mathrm{g,I}}$	0.359	eV
$E_{\mathrm{g,II}}$	1.424	eV
ΔE_{c}	0.697	eV
ΔE_{v}	0.368	eV
$m^*_{\mathrm{c,I}}$	0.027	m_0
$m^*_{\mathrm{c,II}}$	0.0665	m_0
$m^*_{\mathrm{v,I}}$	0.34	m_0
$m^*_{\mathrm{v,II}}$	0.38	m_0

F.3 Testing the QD mesh

The last check we have to do is to ensure that the calculations with the QD structure give solutions that do not change when increasing the size of the calculation domain or increasing the number of mesh points. The mesh that we used in the calculations in Section 7.2 is shown in Fig. A.4a, where we refined the mesh in the area $[0; 2r_1] \times [-10d; h + 10d]$. The normalized eigenvalues are plotted for varying R_0 in Fig. A.4b. For large R_0, the eigenvalues vary only on the fourth significant figure for both the valence and conduction band, and it seems fair to used $R_0 = 50\,\mathrm{nm}$ as done in Section 7.2. The fluctuation may be explained by the fact, that when R_0 is changed, the mesh construction in COMSOL also changes, giving slight changes in the energy. We also tried varying lowering the number of mesh points, which we use in our calculation, but this did not change the eigenenergies or the wavefunction significantly.

In conclusion we have demonstrated that our FEM-model implemented in COMSOL gives correct results for the considered QD-sizes.

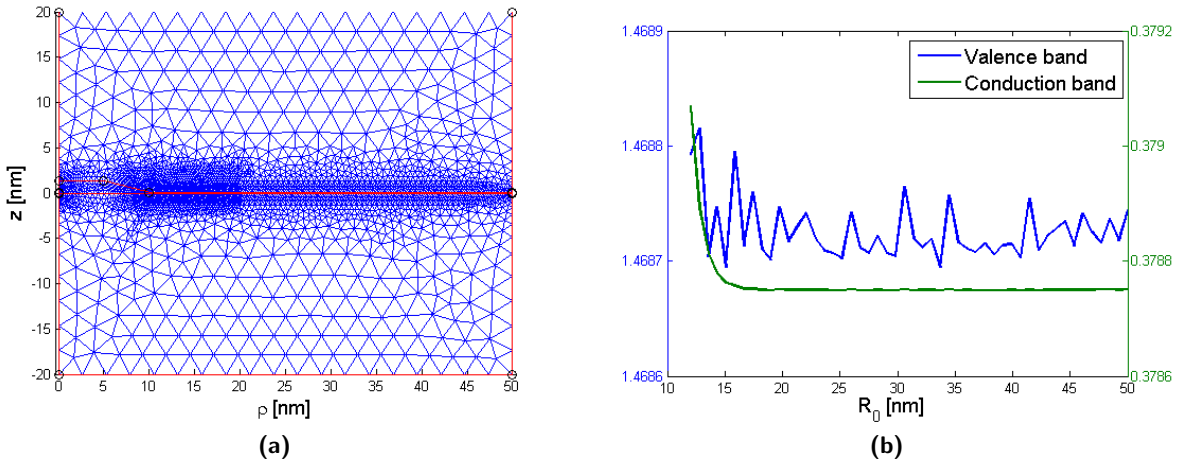

Figure A.4: **(a)** The mesh used in the FEM calculations. The initial mesh was refined in the area $[0; 2r_1] \times [-10d; h + 10d]$. **(b)** The normalized eigenvalues of the ground wavefunction of the valence and conduction band versus the width of the calculation domain.

G Elliptic dot wavefunction

This appendix should be seen as comment to Section 7.2, where a truncated conical dot structure is considered. Here we calculate the wavefunction of another QD shape with an ellipsoidal surface, see Fig. A.5. This shape is similar to the shape of the QD in Fig. 7.1b.

The resulting wavefunction is given in Figs. A.6a and A.6b where the FEM-wavefunction and the fit are compared. As in for the truncated conical dot in Section 7.2 we see that the wavefunction adapts the shape of the QD, giving deviations to the elliptical fit. The conclusions for the lifetime asymmetry and dephasing wave achieved with this structure was qualitatively the same as the one for the truncated conical dot, because the wavefunctions in both cases not are approximately ellipsoidal.

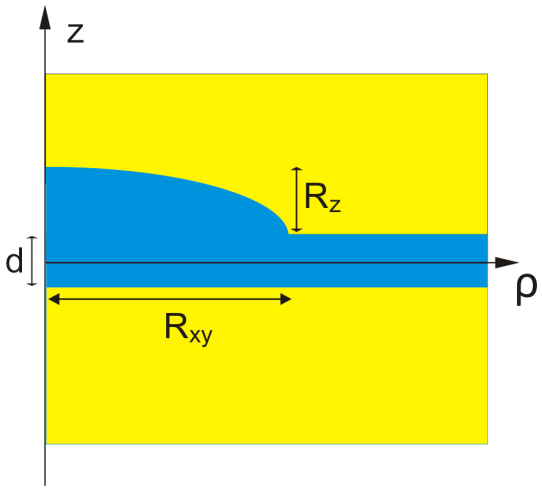

Figure A.5: Sketch of an elliptic dot as implemented in the FEM-calculations.

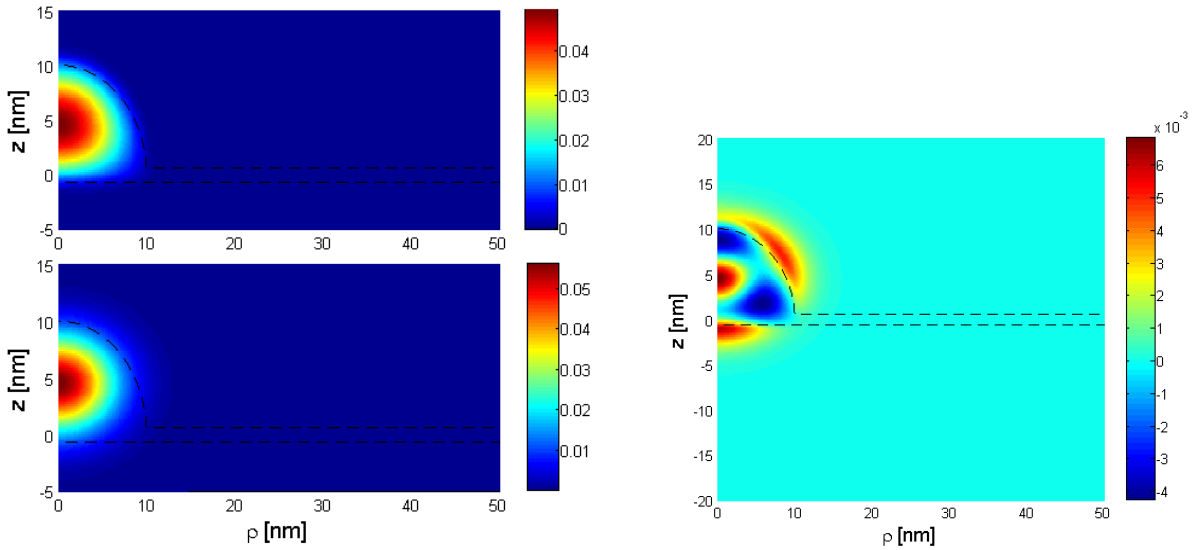

Figure A.6: **(a)** Wavefunction of an electron in the valence band (upper picture) and the corresponding ellipsoidal fit (lower picture). We use $d = 1.25$ nm, $R_z = R_{xy} = 10$ nm, and the material parameters given in Section A. **(b)** Absolute difference $\phi_{\text{fit}} - \phi_{\text{COMSOL}}$ between the wavefunction in Fig. A.6a. The maximum error is about $\sim 15\%$.

Bibliography

[1] P. Kaer et. al. Non-markovian model of photon-assisted dephasing by electron-phonon interactions in a coupled quantum-dot–cavity system. Physical Review Letters, 104(157401), 2010.

[2] Nicolas Gisin et. al. Quantum cryptography. Reviews of Modern Physics, 74:145–195, 2002.

[3] Florian Meier et. al. Quantum computing with spin cluster qubits. Physical Review Letters, 90(4), 2003.

[4] Peng Xue. Universal quantum computing with nanowire double quantum dots. Phys. Scr., 84(045002), 2011.

[5] K. R. Brown et. al. Quantum computing with quantum dots on quantum linear supports. Physical Review A, 65(012307), 2001.

[6] Pieter Kok et. al. Linear optical quantum computing with photonic qubits. Reviews of Modern Physics, 79(1), 2007.

[7] A. Ekert and R. Jozsa. Quantum computation and shor's factoring algorithm. Reviews of Modern Physics, 68(3), 1996.

[8] H. J. Kimble et. al. Photon antibunching in resonance fluorescence. Physical Review Letters, 39(11), 1977.

[9] Andrew J. Shields. Semiconductor quantum light sources. Nature Photonics, 1:215–223, 2007.

[10] Brahim Lounis and Michel Orrit. Single-photon sources. Rep. Prog. Phys., 68:1129–1179, 2005.

[11] David P. DiVincenzo. The physical implementation of quantum computation. Fortschr. Phys., 48(9-11):771–783, 2000.

[12] A. Kuhn and D. Ljunggren. Cavity-based single-photon sources. Contemporary Physics, 51(4), 2010.

[13] Stéphane Laurent et. al. Indistinguishable single photons from a single inas quantum dot in a photonic crystal cavity slab. Physica E, 32:480–483, 2006.

[14] Stefanie Weiler et. al. Highly indistinguishable photons from a quantum dot in a microcavity. Phys. Status Solidi B, 248(4):867–871, 2011.

[15] Peter Michler et. al. A quantum dot single photon source. Advances in Solid State Physics, 41:3–14, 2001.

[16] Charles Santori et. al. Triggered single photons from a quantum dot. Physical Review Letters, 86(8), 2001.

[17] R. M. Thompson et. al. Single-photon emission from exciton complexes in individual quantum dots. Physical Review B, 64(201302), 2001.

[18] Edo Waks et. al. Secure communication: Quantum cryptography with a photon turnstile. Nature, 420(762), 2002.

[19] E. Knill et. al. A scheme for efficient quantum computation with linear optics. Nature, 409:46–52, 2001.

[20] `http://www.princeton.edu/~pccm/outreach/REU2004/S.20LYON%20SHORT%20COURSE.PDF`, October 14, 2011.

[21] Richard Nötzel. Self-organized growth of quantum-dot structures. Semicond. Sci. Technol., 11:1365–1379, 1996.

[22] D. Leonard et. al. Direct formation of quantum-sized dots from uniform coherent islands of ingaas on gaas surfaces. Applied Physics Letters, 63(3203), 1993.

[23] Peter Michler. Single Quantum Dots - Fundamentals, Applications and New Concepts. Springer-Verlag Berlin Heidelberg, 2003.

[24] Peter Michler. Single Semiconductor Quantum Dots. Springer-Verlag Berlin Heidelberg, 2009.

[25] John R. Arthur. Molecular beam epitaxy. Surface Science, 500:189–217, 2002.

[26] S. Stobbe et. al. Frequency dependence of the radiative decay rate of excitons in self-assembled quantum dots: Experiment and theory. Physical Reviev B, 80(155307), 2009.

[27] J. H. Lee et. al. Size and density control of inas quantum dot ensemble of self-assembled nanostructured templates. Semicond. Sci. Technol., 21:1547–1551, 2006.

[28] J. M. Gérard and B. Gayral. Inas quantum dots: artificial atoms for solid-state cavity-quantum electrodynamics. Physica E, 9:131–139, 2001.

[29] Lucio C. Andreani et. al. Strong-coupling regime for quantum boxes in pillar microcavities: Theory. Physical Review B, 60(19), 1999.

[30] D. K. Armani et. al. Ultra-high-q toroid microcavity on a chip. Nature, 421:925–928, 2003.

[31] Kartik Srinivasan et. al. Photonic crystal microcavities for chip-based cavity qed. Phys. stat. sol. (b), 6:1187–1191, 2005.

[32] Kerry J. Vahala. Optical microcavities. Nature, 424:839–846, 2003.

[33] David Press et. al. Photon antibunching from a single quantum-dot-microcavity system in the strong coupling regime. Physical Review Letters, 98(117402), 2007.

[34] E. Peter et. al. Exciton-photon strong-coupling regime for a single quantum dot embedded in a microcavity. Physical Review Letters, 95(067401), 2005.

[35] `http://www.aph.caltech.edu/people/painter_o.html`, October 18, 2011.

[36] Per Kær Nielsen. Fundamental properties of single-photon sources. Master's thesis, Technical University of Denmark.

[37] Conversation with Kristian Høeg Madsen and Asger Kreiner-Møller.

[38] M. Paillard et. al. Time-resolved photoluminiescence in self-assembled inas/gaas quantum dots under strictly resonant excitation. Applied Physics Letters, 76(1), 2000.

[39] Christopher Gerry and Peter Knight. Introductory Quantum Optics. Cambridge University Press, 2005.

[40] P. J. Klar et. al. Photomodulated reflectance study of inxga1-xas/gaas/alas microcavity vertical-cavity surface emitting laser structures in the weak-coupling regime: The cavity/ground-state-exciton resonance. Physical Review B, 59(4), 1999.

[41] K. Hennessy et. al. Quantum nature of a strongly coupled single quantum dot-cavity system. Nature, 445:896–899, 2007.

[42] B. Krummheuer et. al. Pure dephasing and phonon dynamics in gaas- and gan-based quantum dot structures: Interplay between material parameters and geometry. Physical Review B, 71(235329), 2005.

[43] U. Hohenester. Cavity quantum electrodynamics with semiconductor quantum dots: Role of phonon-assisted cavity feeding. Physical Review B, 81(155303), 2010.

[44] S. Hughes et. al. Influence of electron-acoustic phonon scattering on off-resonant cavity feeding within a strongly coupled quantum-dot cavity system. Physical Review B, 83(165313), 2011.

[45] M. I. Vasilevskiy et. al. Electron-phonon interaction effects in semiconductor quantum dots: A nonperturbative approach. Physical Review B, 70(035318), 2004.

[46] H. Bruus and K. Flensberg. Many-Body Quantum Theory in Condensed Matter Physics. Oxford University Press, 2004.

[47] Gerald D. Mahan. Many-Particle Physics. Plenum Press, New York, second edition, 1990.

[48] C. Cohen-Tannoudji, J. Dupont-Roc, and G. Grynberg. Photons and Atoms - Introduction to Quantum Electrodynamics. John Wiley and Sons, Inc., 1989.

[49] M. Kira et. al. Quantum theory of spontaneous emission and coherent effects in semiconductor microstructures. Progress in Quantum Electronics, 23:189–279, 1999.

[50] Wilfried Schäfer and Martin Wegener. Semiconductor optics and transport phenomena. Springer-Verlag Berlin Heidelberg, 2002.

[51] Rodney Loudon. The Quantum Theory of Light. Oxford University Press, third edition.

[52] H. Arenhövel. Subnuclear degrees of freedom in electromagnetic interactions in nuclei. Chinese Journal of Physics, 30(1), 1992.

[53] Leslie E. Ballentine. Quantum Mechanics: A Modern Development. World Scientific Publishing, 1998.

[54] Charles Kittel. Introduction to Solid State Physics. John Wiley and Sons, eigth edition.

[55] Michael A. Stroscio and Mitra Dutta. Phonons in Nanostructures. Cambridge University Press, 2004.

[56] C. Patel et. al. Phonon frequencies in gaas. Phys. stat. sol, 122(461), 1984.

[57] J. Bardeen and W. Shockley. Deformation potentials and mobilities in non-polar crystals. Physical Review, 80(72), 1950.

[58] E. Kartheuser and S. Rodriguez. Deformation potentials and the electron-phonon interaction in metals. Physical Review B, 33(2):772–779, 1986.

[59] F. S. Khan and P. B. Allen. Deformation potentials and electron-phonon scattering: Two new theorems. Physical Review B, 29(6), 1984.

[60] G. Whitfield and P. B. Shaw. Interaction of electrons with acoustic phonons via the deformation potential in one dimension. Physical Review B, 14:3346–3355, 2002.

[61] Peter Y. Yu and Manuel Cardona. Fundamentals of Semiconductors. Springer, third edition, 2005.

[62] Jan Singh. Excitation Energy Transfer Processes in Condensed Matter. Plenum Press, New York, 1994.

[63] Anna Grodecka et. al. Phonon impact on the coherent control of quantum states in semiconductor quantum dots. http://arxiv.org/abs/cond-mat/0404364, 2004.

[64] Neil W. Ashcroft and N. David Mermin. Solid State Physics. Harcourt College Publishers, 1976.

[65] L. Jacak et. al. Coherent and incoherent phonon processes in artificial atoms. Eur. Phys. J. D, 22:319–331, 2003.

[66] B. Krummheuer et. al. Theory of pure dephasing and the resulting absorption line shape in semiconductor quantum dots. Physical Review B, 65(195313), 2002.

[67] M. Esposito and P. Gaspard. Quantum master equation for a system influencing its environment. Physical Review E, 68(066112), 2003.

[68] Heinz-Peter Breuer et. al. Stochastic wave-function method for non-markovian quantum master equations. Physical Review A, 59(2), 1998.

[69] P. K. Nielsen. Electron-phonon interactions in semiconductor quantum dot cavity qed systems. unpublished.

[70] Heinz-Peter Breuer and Francesco Petruccione. The Theory of Open Quantum Systems. Oxford University Press, 2002.

[71] T. Brandes, 2003. Chapter 7 (Quantum Dissipation) - Lectures on Background to Quantum Information.

[72] Howard Carmichael. An Open Systems Approach to Quantum Optics. Springer-Verlag Berlin Heidelberg, 1993.

[73] A. Smirne and B. Vacchini. Nakajima-zwanzig versus time-convolutionless master equation for the non-markovian dynamics of a two-level system. Physical Review A, 82(022110), 2010.

[74] S. Chaturvedi and F. Shibata. Time-convolutionless projection operator formalism for elimination of fast variables. applications to brownian motion. Zeitschrift für Physik B, 35:297–308, 1979.

[75] Larry A. Coldren and Scott W. Corzine. Diode Lasers and Photonic Integrated Circuits. John Wiley and Sons, Inc., 1995.

[76] Ahsan Nazir. Photon statistics from a resonantly driven quantum dot. Physical Review B, 78(153309), 2008.

[77] G. Lindblad. On the generators of quantum dynamical semigroups. Commun. math. Phys, 48:119–130, 1976.

[78] M. Howard et. al. Quantum process tomography and linblad estimation of a solid-state qubit. New Journal of Physics, 8(33), 2006.

[79] L. Jacak et. al. Anharmonicity-induced polaron relaxation in gaas/inas quantum dots. Physical Review B, 65(113305), 2002.

[80] Thomas Grange. Decoherence in quantum dots due to real and virtual transitions: A nonperturbative calculation. Physical Review B, 80(245310), 2009.

[81] E. A. Muljarov and R. Zimmermann. Dephasing in quantum dots: Quadratic coupling to acoustic phonons. Physical Review Letters, 93(237401), 2004.

[82] A. Grodecka *et al.* Interplay and optimization of decoherence mechanisms in the optical control of spin quantum bits implemented on a semiconductor quantum dot. Physical Review B, 76, 2007.

[83] Jean-Michel Gérard. Solid-State Cavity-Quantum Electrodynamics with Self-Assembled Quantum Dots. Nanophysics and Semiconductors Laboratory.

[84] Pierre Meystre and Murray Sargent. Elements of quantum optics. Springer, 2007.

[85] A. Auffèves et. al. Controlling the dynamics of a coupled atom-cavity system by pure dephasing. Phys. Rev. B, 81(245419), 2010.

[86] A. Auffèves et. al. Pure emitter dephasing: A resource for advanced solid-state single-photon sources. Phys. Rev. A, 79(053838), 2009.

[87] A. Grodecka and P. Machnikowski. Partly noiseless encoding of quantum information in quantum dot arrays against phonon-induced pure dephasing. Physical Review B, 73(125306), 2006.

[88] A. Naesby et. al. Influence of pure dephasing on emission spectra from single photon sources. Physical Review A, 78(045802), 2008.

[89] U. Hohenester. Quantum control of polaron states in semiconductor quantum dots. J. Phys. B: At. Mol. Opt. Phys., 40:315–330, 2007.

[90] V. M. Axt et. al. Reducing coherence of the confined exciton state in a quantum dot by pulse-sequence control. Phys. Rev. B, 71(155305), 2005.

[91] U. Hohenester et. al. Phonon-assisted transitions from quantum dot excitons to cavity photons. Physical Review B, 80(201311), 2009.

[92] Y. Ota et. al. Impact of electron-phonon interactions on quantum-dot cavity quantum electrodynamics. arXiv:0908.0788v1, 2009.

[93] I. Wilson-Rae and A. Imamoglu. Quantum dot cavity-qed in the presence of strong coupling electron-phonon interactions. Physical Review B, 65(235311), 2002.

[94] M. Calic et. al. Phonon-mediated coupling of ingaas/gaas quantum-dot excitons to photonic crystal cavities. Physical Review Letters, 106(227402), 2011.

[95] Jens Eising. Linear Algebra. Institut for Matematik, Danmarks Tekniske Universitet, 1999.

[96] Torben Roland Nielsen. Carrier-carrier and carrier-phonon scattering in self-assembled quantum dots. Ph.d. thesis, Universität Bremen.

[97] I. Vurgaftman et. al. Band parameters for iii-v compound semiconductors and their alloys. Journal of Applied Physics, 89(11), 2001.

[98] Su-Huai Wei and Alex Zunger. Predicted band-gap pressure coefficients of all diamond and zinc-blende semiconductors: Chemical trends. Physical Review B, 60(8), 1999.

[99] T. Takagahara. Theory of exciton dephasing in semiconductor quantum dots. Physical Review B, 60(4), 1999.

[100] Jean-Marc Lévy-Leblond. Position-dependent effective mass and galilean invariance. Phys. Rev. A, 52(3), 1995.

[101] T. Markussen et. al. Influence of wetting-layer wave functions on phonon-mediated carrier capture into self-assembled quantum dots. Phys. Rev. B, 74(195342), 2006.

[102] P. Kaer Nielsen et. al. Numerical investigation of electromagnetically induced transparency in a quantum dot structure. Optics Express, 15(10), 2007.

[103] R. V. N. Melnik and M. Willatzen. Bandstructures of conical quantum dots with wetting layers. Nanotechnology, 15:1–8, 2004.

[104] B. H. Bransden and C. J. Joachain. Quantum Mechanics. Pearson Education, second edition, 2000.

[105] T. P. M. Alegre et. al. Quasi-two-dimensional optomechanical crystals with a complete phononic bandgap. Optics Express, 19(6), 2011.

[106] V. Laude et. al. Simultaneous guidance of slow photons and slow acoustic phonons in silicon phoxonic crystal slabs. Optics Express, 19(10), 2011.

[107] M. Maldovan and E. L. Thomas. Simultaneous localization of photons and phonons in two-dimensional periodic structures. Applied Physics Letters, 88(251907), 2006.

[108] A. H. Safavi-Naeini and O. Painter. Design of optomechanical cavities and waveguides on a simultaneous bandgap phononic-photonic crystal slab. Optics Express, 18(14), 2010.

[109] V. Laude et. al. Optomechanical coupling in a two-dimensional photonic crystal defect cavity. Physical Review Letters, 106(203902), 2011.

[110] K. J. Xu and C. Piermarocchi. Dynamics of elastic and inelastic energy transfer between quantum dots in a microcavity. Physical Review B, 84(115316), 2011.

[111] Y. Y. Liao and Y. N. Chen. Pure dephasing of double-quantum-dot charge qubits in freestanding slabs. Physical Review B, 81(153301), 2010.

[112] W.-M. Ju et. al. The dynamics of a double-dot charge qubit embedded in a suspended phonon cavity. The European Physical Journal B, 72:417–422, 2009.

[113] Y. Y. Liao et. al. Decoherence of a charge qubit embedded inside a suspended phonon cavity. Physical Review B, 77(033303), 2008.

[114] Hiroshi Ezawa. Phonons in a half space. Annals of Physics, 67:438–460, 1971.

[115] M. C. Oliveros and D. R. Tilley. Quantization procedure for phonons in an isotropic elastic half-space. Phys. Stat. Sol. (b), 119(675), 1983.

[116] N. Bannov et. al. Electron relaxation times due to the deformation-potential interaction of electrons with confined acoustic phonons in a free-standing quantum well. Physical Review B, 51(15), 1995.

[117] N. Bannov et. al. Confined acoustic phonons in a free-standing quantum well and their interaction with electrons. Phys. Stat. Sol. (b), 183(131), 1994.

[118] B. Krummheuer et. al. Coupled polarization and acoustic-phonon dynamics after optical excitation of quantum dots near surfaces. Physical Review B, 72(245336), 2005.

[119] Neil W. Ashcroft and N. David Mermin. Acoustic Fields and Waves in Solids, Vol II. Krieger, Malabar, second edition, 1989.

[120] Y. Y. Liao et. al. Electric-field-controlled electron relaxation in lateral double quantum dots embedded in a suspended slab. Journal of Applied Physics, 104(104315), 2008.

[121] P. Borri et. al. Ultralong dephasing time in ingaas quantum dots. Physical Review Letters, 87(157401), 2001.

[122] R. Zimmermann et. al. Dephasing in quantum dots via electron-phonon interaction. Proceedings of the 26th International Conference on the (2002).

[123] Dieter Bimberg. Semiconductor Nanostructures. Springer, 2008.

[124] D. Loss and D. P. DiVincenzo. Quantum computation with quantum dots. Physical Review A, 57(1), 1998.

[125] John Sydney Blakemore. Gallium Arsenide. American Institute of Physics, 1993.

[126] Krzystof Gawarecki et. al. Phonon-assisted relaxation and tunneling in self-assembled quantum dot molecules. Phys. Rev. B, 81(245312), 2010.

[127] M. Bagheri Harouni et. al. Influence of phonons on exciton-photon interaction and photon statistics of a quantum dot. Phys. Rev. B, 79(165304), 2009.

[128] Henrik Bruus et. al. Magnetoconductivity of quantum wires with elastic and inelastic scattering. Physical Review B, 48(15), 1993.